

Dissertation

High-Rate Performance of Muon Drift Tube Detectors

von

Philipp Schwegler

eingereicht an der

Fakultät für Physik

der

Technischen Universität München

erstellt am

Max-Planck-Institut für Physik
(Werner-Heisenberg-Institut)

München

Juni 2014



MAX-PLANCK-GESELLSCHAFT

TECHNISCHE UNIVERSITÄT MÜNCHEN

Max-Planck-Institut für Physik
(Werner-Heisenberg-Institut)

High-Rate Performance of
Muon Drift Tube Detectors

Philipp Schwegler

Vollständiger Abdruck der von der Fakultät für Physik der Technischen Universität München zur
Erlangung des akademischen Grades eines

Doktors der Naturwissenschaften (Dr. rer. nat.)

genehmigten Dissertation.

Vorsitzender: Univ.-Prof. Dr. A. Ibarra

Prüfer der Dissertation:

1. Priv.-Doz. Dr. H. Kroha
2. Univ.-Prof. Dr. L. Oberauer

Die Dissertation wurde am 30.06.2014 bei der Technischen Universität München eingereicht und durch
die Fakultät für Physik am 10.07.2014 angenommen.

Abstract

The Large Hadron Collider (LHC) at the European Centre for Particle Physics, CERN, collides protons with an unprecedentedly high centre-of-mass energy and luminosity. The collision products are recorded and analysed by four big experiments, one of which is the ATLAS detector. In parallel with the first LHC run from 2009 to 2012, which culminated in the discovery of the last missing particle of the Standard Model of particle physics, the Higgs boson, planning of upgrades of the LHC for higher instantaneous luminosities (HL-LHC) is already progressing. The high instantaneous luminosity of the LHC puts high demands on the detectors with respect to radiation hardness and rate capability which are further increased with the luminosity upgrade.

In this thesis, the limitations of the Muon Drift Tube (MDT) chambers of the ATLAS Muon Spectrometer at the high background counting rates at the LHC and performance of new small diameter muon drift tube (sMDT) detectors at the even higher background rates at HL-LHC are studied. The resolution and efficiency of sMDT chambers at high γ -ray and proton irradiation rates well beyond the ones expected at HL-LHC have been measured and the irradiation effects understood using detailed simulations. The sMDT chambers offer an about an order of magnitude better rate capability and are an ideal replacement for the MDT chambers because of compatibility of services and read-out. The limitations of the sMDT chambers are now in the read-out electronics, taken from the MDT chambers, to which improvements for even higher rate capability are proposed.

Contents

Abstract	v
Contents	vii
Introduction	xi
1 The ATLAS Experiment at the Large Hadron Collider	1
1.1 Introduction	1
1.2 The Large Hadron Collider	2
1.3 The ATLAS Experiment	4
1.3.1 Detector Components	6
1.3.2 Trigger and Data Acquisition System	12
1.3.3 Data Taking and Analysis	13
1.4 Towards Higher Luminosity	14
1.4.1 LHC Upgrades	14
1.4.2 ATLAS Upgrade Projects	15
2 The ATLAS MDT and sMDT Chambers	17
2.1 Introduction	17
2.2 Monitored Drift Tube Chambers	18
2.2.1 Mechanical Design and Functionality	18
2.2.2 Front-End Electronics	21
2.2.3 Performance of the ATLAS MDT Chambers	27
2.2.4 Performance in the Presence of Radiation Background	30
2.3 Small-Diameter Muon Drift Tube Chambers	31
2.3.1 Technical Implementation	32
2.3.2 The sMDT Prototype Chamber	35
2.3.3 Application of sMDT Chambers in ATLAS	36

3	High-Rate Phenomena in MDT and sMDT Chambers	39
3.1	Introduction	39
3.2	Radiation Background Expectations	40
3.3	Space Charge Effects	40
3.3.1	Gain Drop	44
3.3.2	Space Charge Fluctuations	48
3.4	Read-Out Electronics Effects	48
3.4.1	Signal Characteristics	48
3.4.2	Dead Time Effects	51
3.4.3	Signal Pile-Up Effects	53
4	Calibration and Data Analysis Methods	55
4.1	Background Rate Measurement	55
4.2	Gas Amplification Measurement	56
4.3	Drift Tube Calibration Methods	57
4.3.1	Drift Time Measurement	57
4.3.2	Calibration of the Space-to-Drift Time Relationship	58
4.3.3	Time Slewing Correction	59
4.4	Spatial Resolution	59
4.5	Drift Tube Efficiency	63
5	MDT Chambers Under Photon Irradiation	65
5.1	Introduction	65
5.2	Experimental Setup	66
5.3	Measurements Under Photon Background Radiation	67
5.3.1	Dead Time Measurement	67
5.3.2	Afterpulsing	68
5.3.3	Counting Rate Measurement	70
5.3.4	Spatial Resolution	73
5.3.5	Efficiency	74
6	sMDT Chambers Under Photon Irradiation	77
6.1	Introduction	77
6.2	Experimental Setup	78
6.3	Data Acquisition and Ambient Condition Monitoring	80
6.3.1	Front-End Electronics	80
6.3.2	Irradiation Conditions	81

6.3.3	Monitoring of Ambient Conditions and Slow Control	82
6.4	Data Preparation	84
6.4.1	Time and Drift Distance Calibration	84
6.4.2	Time Slewing Correction	85
6.4.3	Spatial Resolution	87
6.5	Performance Under Irradiation	88
6.5.1	Gas Gain Drop	90
6.5.2	Spatial Resolution	91
6.5.3	Muon Efficiency	98
7	sMDT Chambers Under Proton Irradiation	101
7.1	Introduction	101
7.2	Experimental Setup	102
7.3	Irradiation Conditions	103
7.4	Drop of the Gas Amplification	106
7.5	Data Analysis	108
7.5.1	Proton Rate	108
7.5.2	Spatial Resolution and Efficiency	109
7.6	Results	110
8	Simulation of High-Rate Effects	115
8.1	Introduction	115
8.2	Simulation Chain	115
8.2.1	Recorded Signals	117
8.2.2	Electronics Response	121
8.3	Simulation of Resolution and Efficiency Under Irradiation	123
8.3.1	Comparison with Measurements Under Photon Irradiation	123
8.3.2	Comparison with Measurements Under Proton Irradiation	123
8.3.3	Simulation of Other Chamber Geometries Under Photon Irradiation	126
8.4	Improvements of Signal Processing for High Rates	127
9	Comparison of the MDT and sMDT Drift Tube Performance	133
9.1	Loss of Gas Amplification	133
9.2	Spatial Resolution	134
9.3	Drift Tube Efficiency	136
	Summary	141

A Additional Time Slewing and Pile-Up Corrections	143
List of Figures	147
List of Tables	155
Bibliography	157
Acknowledgements	165

Introduction

Since its start-up in 2009, the Large Hadron Collider (LHC) has delivered integrated luminosities of 5.5 fb^{-1} at a centre-of-mass energy of 7 TeV and of 22.8 fb^{-1} at 8 TeV to the ATLAS and CMS experiments. With the recorded data sets, the Standard Model of particle physics has been confirmed in the new energy regime, culminating in the discovery of the last missing Standard Model particle, the Higgs boson, with a mass of about 125.5 GeV.

Evidence for physics beyond the Standard Model has not yet been found despite a huge variety of searches. These will continue with the next LHC run starting in spring 2015 at an increased centre-of-mass energy of 13 TeV and an instantaneous luminosity reaching at least the design value of $1 \cdot 10^{34} \text{ cm}^{-2} \text{ s}^{-1}$. After a decade of operation, an upgrade of the LHC to the High-Luminosity LHC (HL-LHC) is planned, starting operation in 2025 at an instantaneous luminosity of $7 \cdot 10^{34} \text{ cm}^{-2} \text{ s}^{-1}$. The high instantaneous luminosity of the LHC results in harsh background radiation conditions and puts tight requirements to the detectors and read-out electronics with respect to radiation hardness and rate capability. At HL-LHC luminosity, the rate capability and lifetime of many detector and read-out electronics components of the LHC experiments will be exceeded, requiring replacement of the components.

In this thesis, the performance of the ATLAS Monitored Drift Tube (MDT) chambers with 30 mm tube diameter and of newly developed drift tube detectors with smaller diameter of 15 mm, called sMDT chambers, at high background rates is studied. The reduced tube diameter of the sMDT chambers yields a significant improvement of the rate capability, while compatibility with the detector services and with the read-out system of the MDT chambers is maintained, which makes the sMDT chambers ideal substitutes for the MDT chambers at HL-LHC.

After an introduction about the LHC and the ATLAS experiment and about the planned luminosity upgrades in chapter 1, the principles of the MDT and sMDT chambers and their technical implementation are described in chapter 2. In chapter 3, the expected background radiation rates in the ATLAS detector and the high-rate phenomena caused by it in the MDT and sMDT drift tubes, including their read-out electronics, are discussed. Chapter 4 describes the calibration and analysis methods used for the tests of the MDT and sMDT chambers under irradiation discussed in chapters 5 to 7. In chapter 8, the simulation of the high-rate effects in the sMDT chambers is discussed. Finally, measurements and simulation are compared and summarised in chapter 9.

1

The ATLAS Experiment at the Large Hadron Collider

1.1 Introduction

This chapter introduces the Large Hadron Collider (LHC) and its experiments, in particular the ATLAS detector. The LHC is a hadron accelerator and collider with a circumference of 27 km located at the European centre for particle physics, CERN. Four big experiments, ALICE, ATLAS, CMS and LHCb, study the products of proton and heavy ion collisions.

ATLAS is a multipurpose high-luminosity experiment which addresses a wide range of physics topics. One of its main goals was the search for the last missing particle of the Standard Model of particle physics, the Higgs boson. Now it is the measurement of the properties of the Higgs boson as well as the search for physics beyond the Standard Model like, for instance, for new particles predicted by supersymmetric extensions of the Standard Model.

This chapter describes the layout of the LHC and of the ATLAS detector mainly based on references [1, 2] and gives a brief outlook on planned high-luminosity upgrades.

1.2 The Large Hadron Collider

The Large Hadron Collider (LHC) at CERN [1] is the most powerful hadron accelerator and collider in terms of beam energy and luminosity to date. It is housed in the same 26.7 km long tunnel as the Large Electron–Positron Collider (LEP) before, which was shut down and decommissioned in 2000.

The tunnel is ring-shaped, consisting of eight straight sections and eight arcs, and is located 45 to 170 m below the surface on a slightly (1.4 %) inclined plane. Two 2.5 km long transfer tunnels connect it to the rest of the CERN accelerator complex (see Figure 1.1) which is used for beam injection.

As proton–proton collider, the LHC contains two separate vacuum pipes with oppositely oriented magnetic fields for the counter-rotating beams. A “twin bore design” was chosen for the superconducting dipole magnets that keep the beams on circular orbits. In this compact design, the two rings are integrated into the superconducting magnets in the same cryostat. The dipole magnets generate a field strength of up to 8.33 T allowing for a maximum proton beam energy of 7 TeV. The proton beams are not continuous but divided into 2808 bunches of $1.15 \cdot 10^{11}$ protons each with 25 ns spacing resulting in a collision rate of 40 MHz at design operation of the LHC.

The instantaneous design luminosity of the LHC is $\mathcal{L} = 1 \cdot 10^{34} \text{ cm}^{-2} \text{ s}^{-1}$. The event rate of a specific process is given by

$$\frac{dN}{dt} = \sigma(\sqrt{s}) \cdot \mathcal{L},$$

where $\sigma(\sqrt{s})$ is the cross-section of the process which depends on the centre-of-mass energy \sqrt{s} of the proton beams. The total number of expected events in a time period is given by

$$N = \sigma(\sqrt{s}) \int \mathcal{L} dt = \sigma(\sqrt{s}) \cdot L,$$

where L denotes the integrated luminosity.

Four of the eight straight sections of the LHC house the big experiments: ALICE, ATLAS, CMS and LHCb. ATLAS [2] and CMS [3] are multipurpose detectors designed to operate at the design centre-of-mass energy of $\sqrt{s} = 14 \text{ TeV}$ and luminosities of up to $\mathcal{L} = 1 \cdot 10^{34} \text{ cm}^{-2} \text{ s}^{-1}$. After the achievement of the main goal, the discovery of the Higgs boson [4, 5] as the last missing particle of the Standard Model, they search for any accessible physics beyond the Standard Model perform measurements of the properties of the Higgs boson like coupling strengths to fermions and bosons, CP quantum numbers and total decay width.

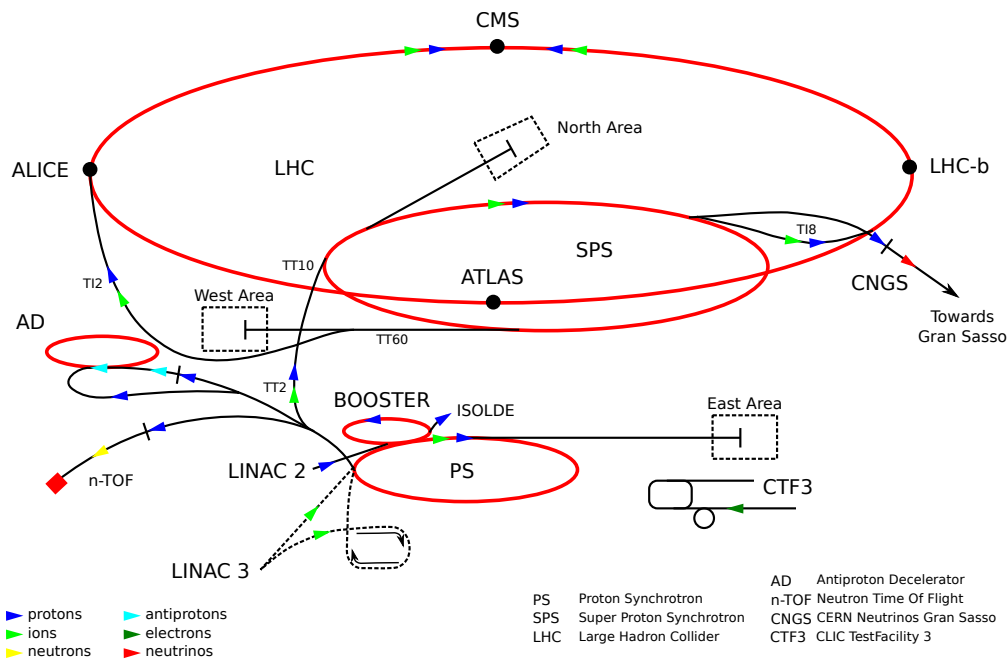


Figure 1.1: The CERN accelerator complex.

LHCb [6] is an experiment dedicated to b -hadron physics designed for a lower luminosity of $\mathcal{L} = 1 \cdot 10^{32} \text{ cm}^{-2} \text{ s}^{-1}$. It performs precision measurements of CP-violation that may help to explain the matter–antimatter asymmetry in the universe and searches for rare B meson decays.

In addition to protons, the LHC can collide lead ions ($^{208}\text{Pb}^{+82}$) in lead–lead and lead–proton operating modes at a centre-of-mass energy of $\sqrt{s} = 2.76 \text{ TeV}$ per nucleon. At the high energy densities reached in lead–lead collisions, quarks and gluons are expected to form a colour-deconfined state called quark–gluon plasma. The ALICE experiment [7] is devoted to the study of heavy ion collisions at a luminosity of $\mathcal{L} = 1 \cdot 10^{27} \text{ cm}^{-2} \text{ s}^{-1}$.

The four big LHC experiments share their interaction points with three additional smaller experiments: LHCf, TOTEM and MoEDAL. LHCf [8] consists of two detectors 140 m from the interaction point on either side of the ATLAS detector and aims for a better understanding of the origin of ultra-high-energy cosmic rays. TOTEM [9] shares the interaction point with CMS and consists of detectors 147 m and 220 m from the collision point. Its goal is the measurement of the total proton–proton interaction cross section and elastic and diffractive scattering processes. MoEDAL [10], approved in 2010, is the youngest of the LHC experiments. Its goal is the search for magnetic monopoles and other strongly ionising massive particles.

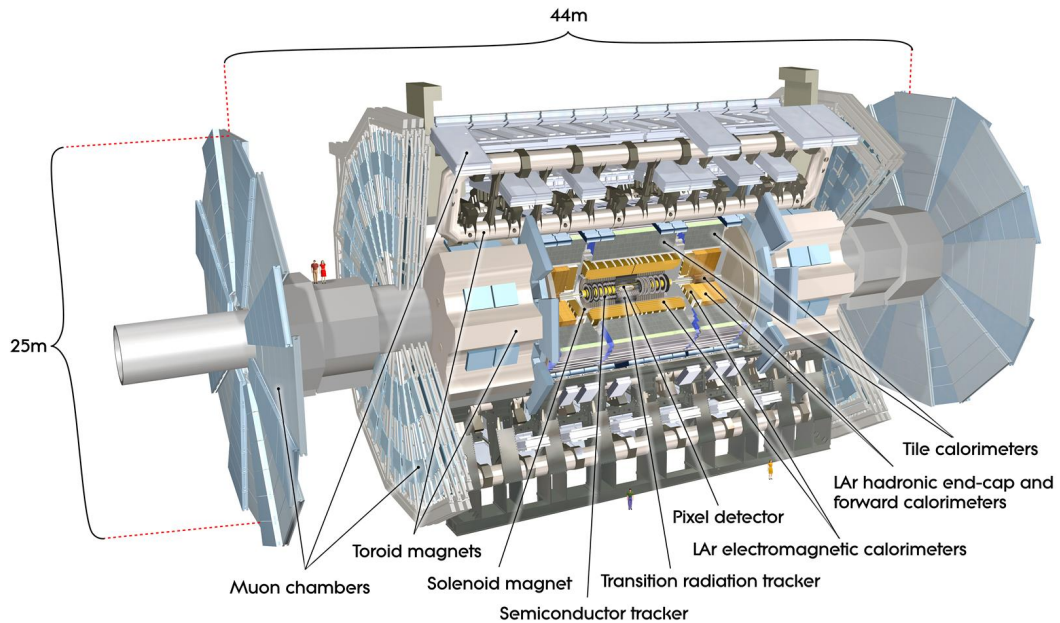


Figure 1.2: The ATLAS experiment at the Large Hadron Collider [2].

1.3 The ATLAS Experiment

The ATLAS detector is a multipurpose detector designed to explore a wide range of physics topics. The unprecedented energy and luminosity of the LHC allow for both precision measurements of the Standard Model on QCD, electroweak interactions and flavour physics and searches for any conceivable new physics processes beyond the Standard Model.

The high interaction rate puts, however, strong demands on the detectors and electronics in terms of radiation tolerance and spatial and time resolution. The production cross-sections of most interesting processes are many orders of magnitude smaller than the total inelastic proton–proton cross-section of about 80 mb which is dominated by dijet production. At design luminosity, with 40 MHz bunch crossing rate, each interesting event is accompanied by on average 23 inelastic events. Highly granular, radiation hard detectors and electronics are needed to cope with the high radiation levels and track density to control the effects of overlapping events. As the read-out and storage capacity is limited, a very selective and efficient trigger system is required to arrive at a manageable data volume without discarding interesting rare events.

High resolution electromagnetic calorimetry is important for efficient electron and photon identification and precise energy measurement. Hermetic hadronic calorimetry is essential for accurate jet and missing transverse energy measurements which are fundamental for many studies.

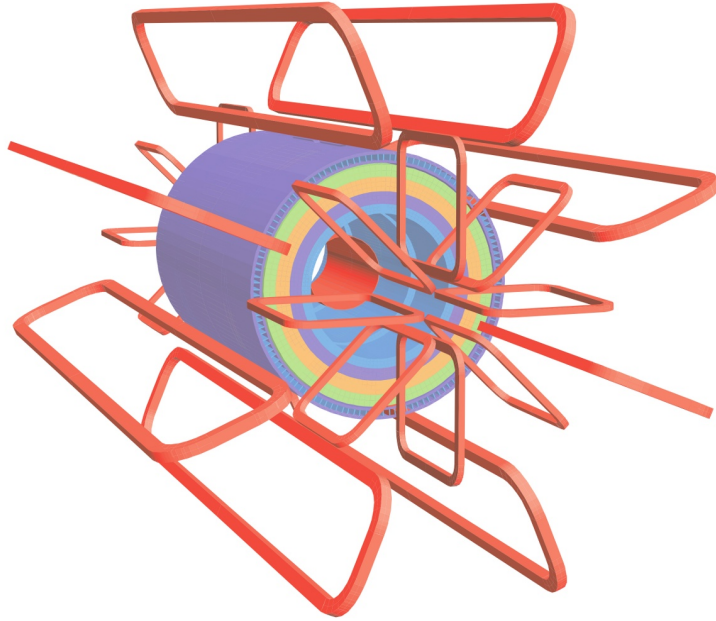


Figure 1.3: The superconducting solenoid (blue) and toroid (red) magnet coils [2].

The ATLAS detector, depicted in Figure 1.2, is forward–backward symmetric with respect to the interaction point. The individual sub-detectors are arranged cylindrically around the beam pipe in the central barrel region and in discs in the so-called end-caps, typical for many collider experiments.

The superconducting magnet system consisting of a thin solenoid coil surrounding the inner tracking detector with a length of 5.3 m and a diameter of 2.5 m and three large air-core toroids (one for the barrel and one for each end-cap) in the Muon Spectrometer determines the size and geometry of the detector. The layout of the magnet system is shown in Figure 1.3.

ATLAS uses a right-handed coordinate system with its origin at the nominal interaction point in the centre of the detector and the z -axis along the beam line. The x -axis points from the interaction point to the centre of the LHC ring and the y -axis is directed upwards. Cylindrical coordinates (r, θ, ϕ) are used in the transverse plane, where ϕ is the azimuthal angle around the beam line, θ the polar angle and r the radius measured from the beam line. Transverse observables (index “ T ”) are projections into the x – y plane perpendicular to the beam line. For many applications, the pseudorapidity is used as replacement of the polar angle θ given by $\eta = -\ln \tan \theta/2$.

Table 1.1: Energy (E) and transverse momentum (p_T) resolution and η coverage of the ATLAS sub-detectors, where E and p_T are in units of GeV. The η limits in parentheses correspond to the trigger coverage [2].

Detector component	Required resolution	$ \eta $ coverage (trigger)
Tracking	$\sigma_{p_T}/p_T = 0.05\% \oplus 1\%$	≤ 2.5
Electromagnetic calorimetry	$\sigma_E/E = 10\%/\sqrt{E} \oplus 0.7\%$	≤ 3.2 (≤ 2.5)
Hadronic calorimetry (jets)		
barrel and end-cap	$\sigma_E/E = 50\%/\sqrt{E} \oplus 3\%$	≤ 3.2
forward	$\sigma_E/E = 100\%/\sqrt{E} \oplus 10\%$	$3.1 < \eta < 4.9$
Muon spectrometer	$\sigma_{p_T}/p_T = 10\%$ at $p_T = 1$ TeV $= 3\%$ at $p_T = 100$ GeV	≤ 2.7 (≤ 2.4)

1.3.1 Detector Components

This section describes the sub-detectors of the ATLAS experiment. The performance specifications of the individual subsystems in terms of energy and momentum resolution and pseudorapidity coverage are summarised in Table 1.1.

The Inner Tracking Detector

About 1000 particles emerge from a proton collision at the LHC leading to a high density of tracks in the detector. ATLAS uses a combination of three technologies in the Inner Detector (ID) — silicon pixel and micro-strip (SCT) detectors and a Transition Radiation Tracker (TRT) — to achieve the required momentum and vertex resolutions. The ID is immersed in a 2 T magnetic field created by the central solenoid. The overall layout of the ID is illustrated in Figure 1.4.

The innermost component is the Pixel Detector arranged around the interaction point in three concentric cylinders in the barrel region and disks perpendicular to the beam line in the end-cap regions. The spatial resolution provided by the Pixel Detector is $10\ \mu\text{m}$ in the transverse plane and $115\ \mu\text{m}$ in the longitudinal direction with respect to the beam line. The innermost detector layer is at a distance of only 5 cm from the beam line and is especially important for the measurement of decay vertices needed for b -quark and τ -lepton identification as well as for searches for new long-lived particles. The Pixel Detector has approximately 80.4 million read-out channels.

In a similar layout but with four layers, the Semiconductor Tracker SCT (Semiconductor Tracker) surrounds the Pixel Detector. It uses silicon micro-strip sensors with an average strip pitch of $80\ \mu\text{m}$ assembled back-to-back with a stereo angle of 40 mrad in each layer to measure track coordinates with a resolution of $17\ \mu\text{m}$ in transverse and $580\ \mu\text{m}$ in longitudinal direction. Both the Pixel and the SCT detectors cover the pseudorapidity range $|\eta| < 2.5$.

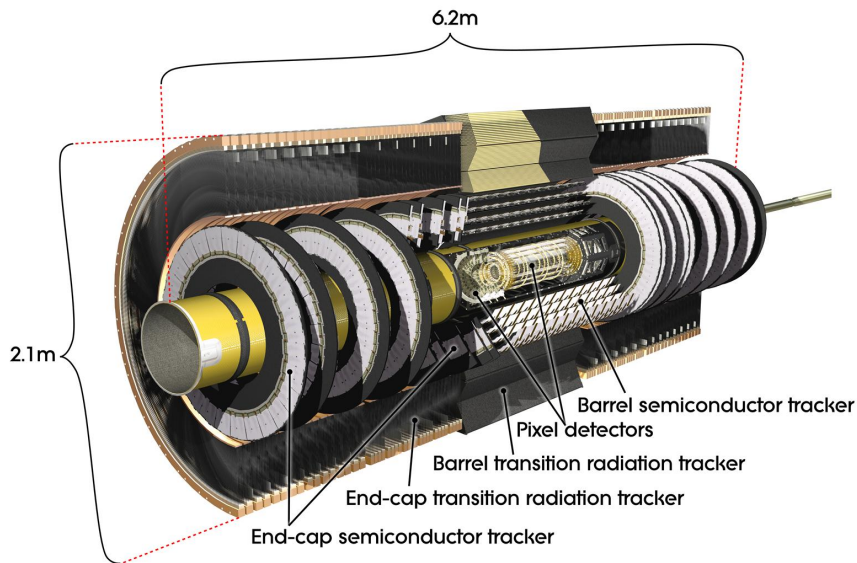


Figure 1.4: The ATLAS Inner Detector [2].

The outermost component of the ID is the TRT consisting of 4 mm diameter straw drift tubes made of 35 μm thick Kapton with 31 μm diameter gold-plated tungsten anode wires operated with $\text{Xe}/\text{CO}_2/\text{O}_2$ (70/27/3) gas at 5 to 10 mbar over-pressure. The TRT provides on average 36 coordinates per track with a resolution of 130 μm in transverse direction over a pseudorapidity range of $|\eta| < 2.0$. Transition radiation photons from electrons traversing the polypropylene fibres and foils with which the straws are interleaved ionise the Xenon gas yielding much larger signals than minimum-ionising particles and thus providing electron identification. The large number of hits per track allows for robust pattern recognition.

The Calorimeters

The ATLAS calorimeter system consists of electromagnetic and hadronic sampling calorimeters covering the pseudorapidity range $|\eta| < 4.9$. The total thickness of the electromagnetic calorimeters is more than 22 radiation lengths. Approximately 11 nuclear interaction length of the whole calorimeter system sufficiently reduce the punch-through into the Muon Spectrometer. The high containment of hadrons together with the large η -coverage enables high jet and missing transverse energy resolution which are crucial for a hadron collider experiment. An overview of the calorimeter system is given in Figure 1.5.

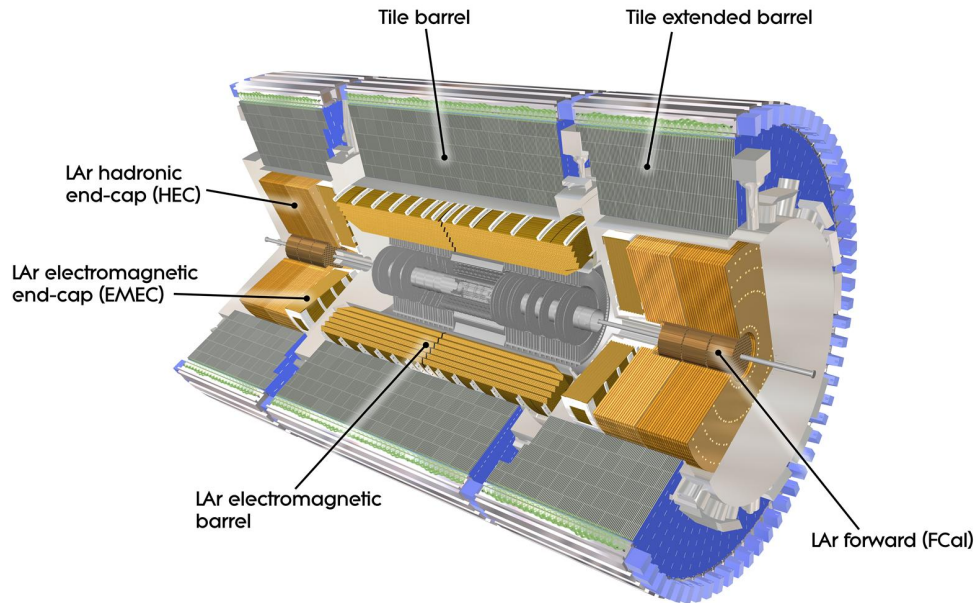


Figure 1.5: The ATLAS calorimeter system [2].

Electromagnetic Calorimeters The electromagnetic calorimeter uses liquid argon (LAr) as active medium and lead absorber material in a barrel part and two end-cap parts, each housed in their own cryostats. The barrel part shares the vacuum vessel with the superconducting solenoid magnet it surrounds minimising the amount of dead material which deteriorates the energy resolution. Each end-cap consists of two coaxial wheels. All parts consist of radially accordion-shaped lead absorber plates and Kapton electrodes. The accordion geometry provides homogeneous azimuthal response and electronics connections at the outer diameter. The absorber plate thickness is optimised for energy resolution as a function of η . For $|\eta| < 2.5$, the electromagnetic calorimeter is segmented into three sections in depth, while in the more forward regions there are only two sections in depth and also the lateral granularity is reduced. In the range $|\eta| < 1.8$, a highly segmented LAr presampler is used to correct for energy loss upstream of the calorimeter.

Hadronic Calorimeters The hadronic calorimeter consists of a barrel and two end-cap parts supplemented by a forward calorimeter. The barrel Tile Calorimeter with its extensions uses steel as absorber and scintillating tiles as active medium and covers the ranges $|\eta| < 1.0$ and $0.8 < |\eta| < 1.7$, respectively. Both the barrel and the extended barrels are segmented into 64 modules azimuthally and three sections in depth. The scintillating tiles are read out on two sides by photomultiplier tubes via wavelength shifting fibres. The hadronic end-cap LAr calorimeter

is located directly behind the electromagnetic end-cap calorimeter and shares the same cryostat. It consists of two wheels on each side, each consisting of 32 wedge-shaped modules. Copper plates, 25 mm thick in the inner and 50 mm thick in the outer wheel, are used as absorber material, separated by 8.5 mm wide LAr gaps.

The forward calorimeter shares the cryostats with the end-cap calorimeters and covers the range $3.1 < |\eta| < 4.9$. It is recessed by about 1.2 m with respect to the front of the electromagnetic calorimeter in order to reduce neutron albedo into the inner detector. It also uses LAr as the active medium and consists of three modules in longitudinal direction. The innermost module optimised for electromagnetic measurements uses copper absorbers, the other two optimised for measurements of hadronic interactions use tungsten absorbers. A matrix of longitudinal channels filled with LAr as active medium is embedded into the absorber materials.

The Muon Spectrometer

The main characteristic of the ATLAS detector is the Muon Spectrometer which defines the overall size of the detector with 44 m in length and 25 m in diameter. It measures the deflection of muon tracks in the magnetic field generated by large superconducting air-core toroid magnets and is designed to provide a highly efficient muon trigger and high-precision muon momentum measurement up to the TeV scale. The air-core magnet design minimises the degradation of the momentum resolution due to multiple scattering. An overview of the Muon Spectrometer is given in Figure 1.6.

The Muon Spectrometer is subdivided into the barrel part ($|\eta| < 1.4$), where the toroidal magnetic field is provided by the eight 20 m long superconducting coils and two end-caps ($1.6 < |\eta| < 2.7$), where the magnetic field is provided by two separate superconducting toroid magnets. In the transition region between the barrel and the end-caps ($1.4 < |\eta| < 1.6$), there is a superposition of the barrel and end-cap toroid fields. While the eight barrel toroid coils are housed in individual cryostats assembled symmetrically around the beam line, the end-cap toroid coils on either side of the detector share a common cryostat. The eight end-cap toroid coils are rotated by 22.5° with respect to the barrel toroid coils in order to provide radial overlap and improve the bending power in the transition region (see Figure 1.3). The magnetic field is mostly perpendicular to the muon trajectories and provides a bending power in the range from 1 to 7.5 T m.

Dedicated detectors for precision tracking and triggering are arranged in three cylindrical layers around the beam axis in the barrel and in three wheels in the end-cap regions. The majority of the precision tracking chambers are Monitored Drift Tube (MDT) chambers which are described in detail in the following chapter as they form the framework of this thesis. Only

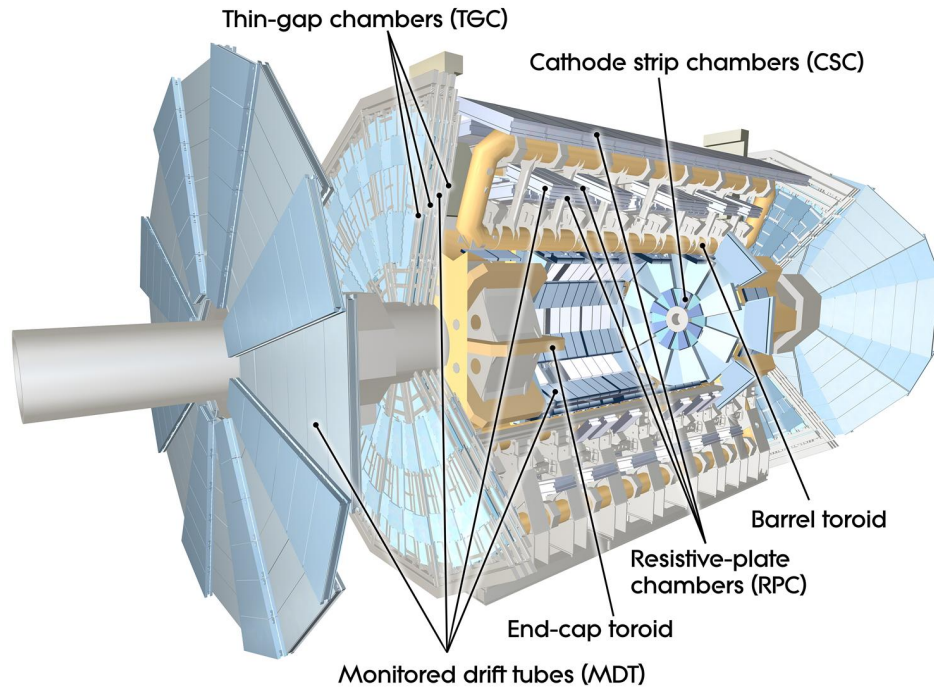


Figure 1.6: The ATLAS Muon Spectrometer [2].

in the inner end-cap layer at large pseudorapidity ($2.0 < |\eta| < 2.7$), where the particle flux is too high for the MDT chambers, Cathode Strip Chambers (CSC) with higher granularity and faster response are used. In total, 1150 MDT chambers with 350 000 drift tubes and 32 CSCs with 31 000 channels cover the pseudorapidity range $|\eta| < 2.7$.

Resistive Plate Chambers (RPC) are used as trigger detectors in the barrel region while Thin Gap Chambers (TGC) are used in the end-caps. Besides providing a fast trigger decision, the trigger chambers provide bunch crossing identification and measurement of the second coordinates of the muon tracks in the direction of the drift tubes of the MDT chambers. The spatial resolution is only on the order of 1 cm.

Figure 1.7 illustrates the principle of the muon trigger. The muon momentum measurement of the trigger chambers is based on the angular deviation between a straight line connecting a hit in the so-called pivot or reference plane with the nominal interaction point and a straight line connecting the hit in the pivot plane with a hit in one of the other two detector layers. In the barrel region, the pivot plane is the middle RPC layer (RPC2) while in the end-caps it is the outermost TGC layer (TGC3). Depending on whether the second hit is in the close or in the distant layer, one obtains a low- or a high- p_T trigger. An additional fourth TGC layer in front of the end-cap toroid magnet is used to reduce the number of fake triggers from tracks not originating from the

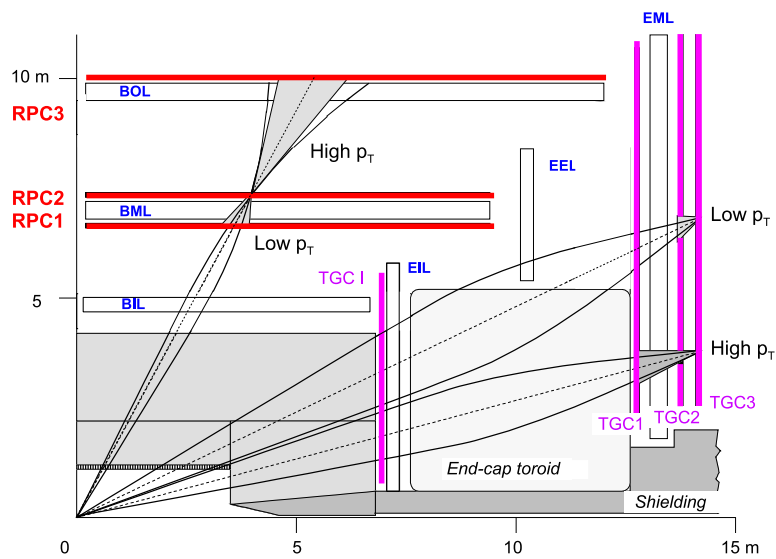


Figure 1.7: Illustration of the Level-1 muon momentum trigger in one quadrant of the detector cross section containing the beam line, three layers of RPCs in the barrel and 3 layers of TGCs in the middle end-cap wheel. The p_T -thresholds are defined by deviations of the track from a straight line connecting the track point in a reference or pivot plane and the interaction point. The pivot plane in the barrel is the middle RPC layer and in the end-caps the outermost TGC layer. The other two layers, RPC1 or RPC3 and TGC1 or TGC2, are used for low- p_T and high- p_T trigger thresholds, respectively [2].

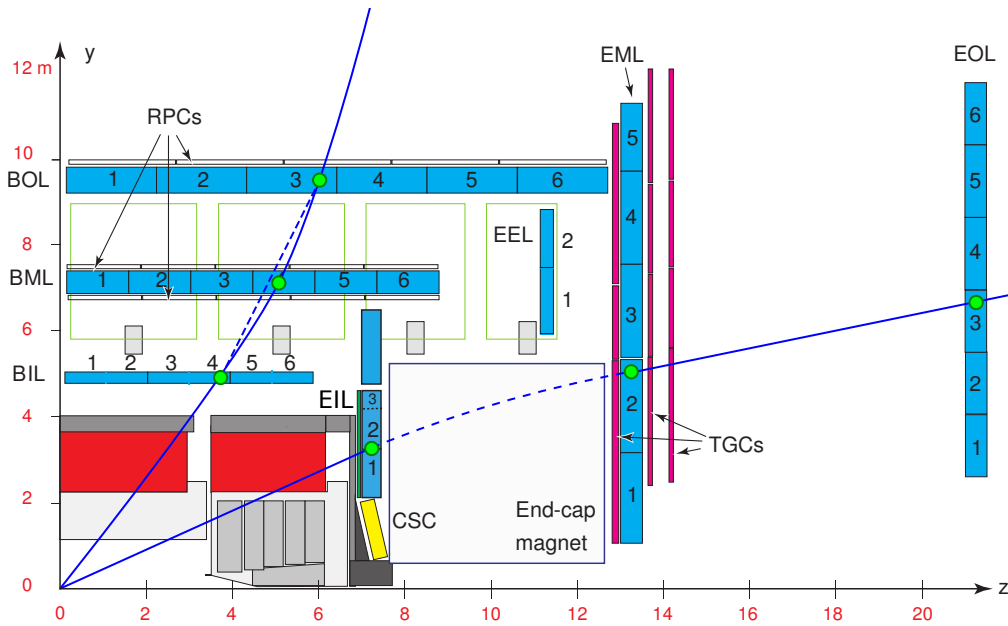


Figure 1.8: Illustration of the muon momentum measurement in the ATLAS Muon Spectrometer.

interaction point.

Figure 1.8 illustrates the precision muon momentum measurement. In the barrel region it is based on the measurement of the track sagitta from hits in three muon detector layers while in the end-cap regions a point in the inner layer (EI) and a polar angle measurement are used for each track.

Precise knowledge of the magnetic field and of the relative chamber positions is essential to achieve the desired momentum resolution of $\sigma_{p_T}/p_T = 10\%$ for 1 TeV muons. The alignment of the precision tracking chambers, both internally and with respect to each other, relies on an optical alignment monitoring system combined with chamber position measurement using straight muon tracks while the magnetic field is turned off. The magnetic field is measured with approximately 1800 Hall probes in the muon spectrometer volume.

1.3.2 Trigger and Data Acquisition System

ATLAS uses a three-level trigger system to reduce the event rate from the 40 MHz bunch crossing rate to approximately 200 Hz written to tape. The first trigger level (L1) is implemented in custom-made electronics. The second (L2) and third (Event Filter) levels use commercial computer farms.

The L1 trigger (see Figure 1.9) takes decisions within $2.5\ \mu\text{s}$ and reduces the event rate to about 100 kHz. It searches for high transverse momentum muons, electrons, photons, jets and

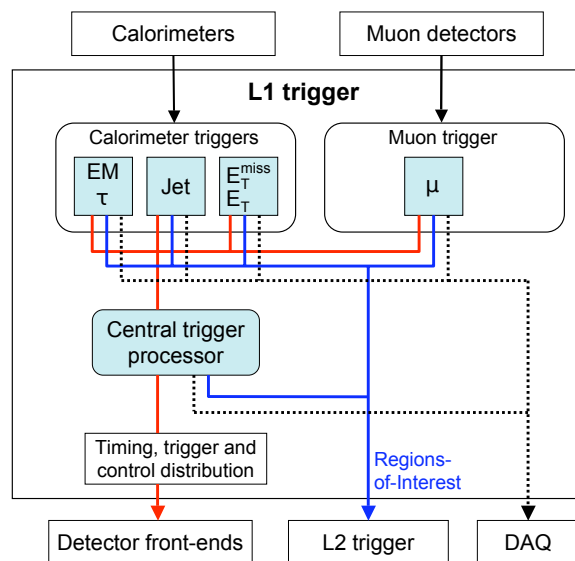


Figure 1.9: Schematic of the first level (L1) trigger [2].

τ -leptons decaying into hadrons as well as for events with large transverse energy or large missing transverse energy using information from the RPC and TGC muon trigger chambers and from the calorimeters with reduced granularity. The L1 decision is taken by the Central Trigger Processor (CTP) which also provides selection criteria like passed thresholds and regions-of-interest (RoI) information to the L2 trigger.

The L2 trigger uses the RoI information provided by the L1 trigger as seeds for the processing of the full detector information with simplified reconstruction programs within the RoIs. It reduces the event rate to about 3.5 kHz with an average processing time of 40 ms.

The final event selection is performed by the third stage, the “Event Filter”, which uses the full ATLAS event reconstruction software. It reduces the event rate to 200 Hz with a typical processing time of four seconds per event. With an average event size of 1.3 MB, the average output bandwidth is almost 300 MB/s.

1.3.3 Data Taking and Analysis

During the first period of operation from 2010 to 2012, now called Run 1, the LHC has delivered integrated luminosities of $L = 5.5 \text{ fb}^{-1}$ at a centre-of-mass energy of $\sqrt{s} = 7 \text{ TeV}$ and of $L = 22.8 \text{ fb}^{-1}$ at $\sqrt{s} = 8 \text{ TeV}$ to the ATLAS and CMS experiments [11].

With the recorded data sets, the Standard Model (SM) of particle physics has been confirmed in the new energy regime culminating in the discovery of the last missing SM particle, the Higgs

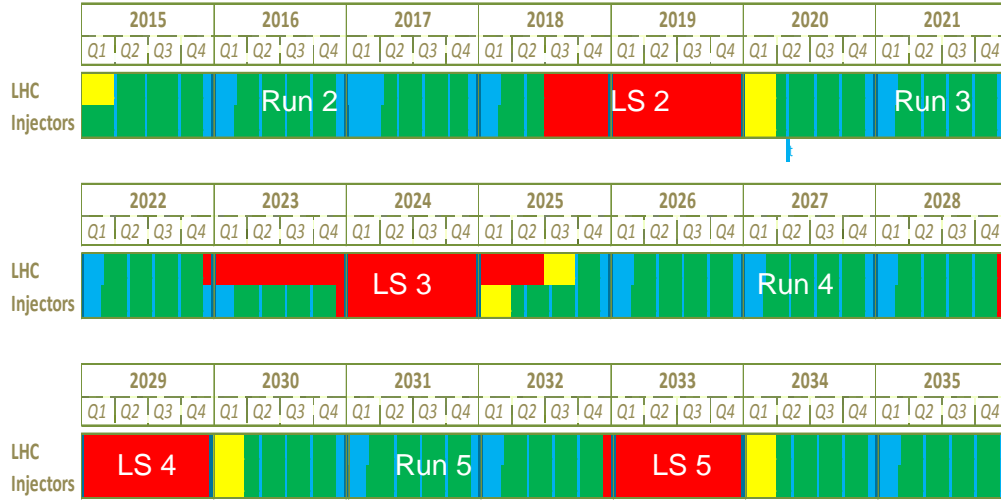


Figure 1.10: CERN LHC and HL-LHC schedule [15].

boson, in 2012 [4, 5] with a mass of $m_H \approx 125.5$ GeV [12, 13] and rate compatible with the SM prediction.

Despite a huge variety of searches, no evidence for physics beyond the Standard Model has been found yet. The searches will continue with LHC Run 2 in 2015 at an increased centre-of-mass energy of 13 TeV.

Whether or not new physics will be found in Run 2, an increase of the integrated luminosity is desirable to study the still open questions of the Standard Model like the naturalness or hierarchy problems or the origins of dark matter and of the matter–antimatter asymmetry.

1.4 Towards Higher Luminosity

1.4.1 LHC Upgrades

During Run 2, which is planned to last from mid 2015 to mid 2018, the LHC will reach the design luminosity and energy. After the so-called Phase-I upgrades of the LHC with improvements to the injectors including a new linear accelerator LINAC4 [14] replacing the current LINAC2 (see Figure 1.1), the instantaneous luminosity will be doubled to $2 \cdot 10^{34} \text{ cm}^{-2} \text{ s}^{-1}$. In this configuration, the LHC will be operated until 2023 and deliver at least 300 fb^{-1} of proton–proton collisions to the ATLAS and CMS experiments.

After Phase-II upgrades from 2023 to 2025, the LHC will reach an instantaneous luminosity of $7 \cdot 10^{34} \text{ cm}^{-2} \text{ s}^{-1}$ (High-Luminosity LHC or HL-LHC) and deliver 3000 fb^{-1} within the following ten years.

1.4.2 ATLAS Upgrade Projects

With the increase of the instantaneous luminosity beyond the design value and extended running time, the LHC experiments need to adapt to the higher demands on rate capability, radiation hardness, particle multiplicities and trigger selectivity in order to benefit from the higher luminosity. This section gives an overview of planned ATLAS upgrade projects in the coming decade. The goal of the upgrades is to at least maintain and even improve upon the design performance at the higher luminosity.

Detector Consolidation Phase-0

The biggest upgrade project during the first long LHC shutdown (2013–2014) is the installation of the “Insertable *B*-Layer” (IBL), a fourth layer added inside the present pixel detector on a new beam pipe [16]. The IBL improves the decay vertex reconstruction and hence the *b*-hadron and τ -lepton identification and compensates for deterioration of present pixel detector due to radiation damage.

The other important upgrade project is the installation of additional muon tracking chambers to improve the momentum resolution in a so far poorly instrumented region of the barrel Muon Spectrometer [17]. A new type of smaller diameter drift tube (sMDT) chambers is used which will be described in the next chapter.

Phase-I Upgrades

The Phase-I upgrades of the Muon Spectrometer in 2018–2019 anticipate necessary improvements for HL-LHC [18]. The main project is the replacement of the inner end-cap layer of the Muon Spectrometer, the so-called Small Wheel, by the New Small Wheel (NSW) using detector technologies with higher rate capability and spatial trigger detector resolution [19].

Phase-II Upgrades

The Phase-II upgrades are planned for 2022–2024 and enable efficient operation at HL-LHC conditions for additional ten years to collect collision data corresponding to 3000 fb^{-1} [20]. Complete replacement of the inner tracking detector, which reaches the end of its lifetime after 400 fb^{-1} , is required. The new tracker has to deal with a much higher track multiplicity from up to 200 interactions per bunch crossing and tolerate more than an order of magnitude higher radiation doses.

To limit the trigger rate without discarding interesting events, the selectivity of the L2 trigger has to be reached already at L1. With trigger latencies above $30 \mu\text{s}$, inner detector

track reconstruction information can be incorporated into the L1 trigger and combined with more complex calorimeter and muon triggers [21]. The low-momentum muon trigger rate can be suppressed by higher momentum resolution of the L1 muon trigger using the high spatial resolution of the MDT chambers [22, 23].

2

The ATLAS MDT and sMDT Chambers

2.1 Introduction

This chapter introduces the ATLAS Monitored Drift Tube (MDT) chambers used as precision tracking detectors in the current ATLAS Muon Spectrometer and a new type of drift tube chambers with smaller tube diameter called sMDT chambers developed for upgrades of the muon detector.

MDT and sMDT chambers consist of several layers of drift tubes operated in proportional mode with low gas amplification in order to prevent ageing. Knowing the time when a muon passes the detector, the drift time of the primary ionisation electrons can be measured in each drift tube and translated into a drift radius. The chambers are designed to provide a spatial resolution of 35 μm in order to achieve the desired muon momentum resolution in the Muon Spectrometer.

The ATLAS MDT chambers are exposed to unprecedentedly high photon and neutron background irradiation with counting rates of up to 500 Hz/cm². The chamber resolution and efficiency degrade due to the background radiation rates which increase with the LHC luminosity. Hence, a new type of MDT chambers with reduced tube diameter and, therefore, higher rate capability, the sMDT chambers, has been developed. In addition, the sMDT chambers are more compact allowing for the instrumentation of confined detector regions.

2.2 Monitored Drift Tube Chambers

Monitored Drift Tube (MDT) chambers constitute the majority of the precision tracking chambers in the ATLAS Muon Spectrometer. In this chapter, the layout and functionality of the MDT chambers and their performance as well as the limitations of their background rate capability are discussed.

2.2.1 Mechanical Design and Functionality

The basic components of the MDT chambers are aluminium drift tubes with 29.970 mm outer diameter and 400 μm wall thickness filled with Ar/CO₂ (93/7) gas at 3 bar absolute pressure*. Electrons created by ionisation of the Argon atoms by traversing charged particles drift towards a gold-plated tungsten-rhenium anode wire with 50 μm diameter which is kept at a potential of +3080 V with respect to the tube walls (see Figure 2.1). The ionisation is a stochastic process. Clusters of electron–ion pairs are created along the muon path with a density of around 100 cm^{-1} (cf. Figure 2.2) and a typical size of 3 electron–ion pairs.

Within about 150 μm of the wire, the drifting ionisation electrons gain enough kinetic energy in the radial electric field between collisions that they ionise further Argon atoms in an avalanche multiplying the primary ionisation charge by a factor of $2 \cdot 10^4$, the gas amplification or gas gain. With the knowledge of the time when the muon passed the tube from an external source — in the case of ATLAS this is the bunch crossing time delivered by the LHC corrected for the time-of-flight of the muon from the interaction point to the detector and propagation times — one can determine the electron drift time by measuring the avalanche arrival time at the wire. The drift time can be translated into the drift radius at which the muon crossed the tube, once the space-to-drift-time relationship $r(t)$ has been determined using dedicated calibration algorithms [24–26].

The tube gas volume is sealed by end-plugs consisting of insulating plastic (Noryl) and a central brass insert that holds the anode wire concentrically with respect to the aluminium reference rings with an accuracy of 10 μm (see Figure 2.1). The wire tension is adjusted with high accuracy to (350 ± 15) g during the tube assembly to define the wire sag and the wire position over the whole tube length with an accuracy of 10 μm . The metal inserts also facilitate gas inlet and outlet and the electrical signal and high-voltage connections on opposite tube ends. The main MDT chamber parameters are summarised in Table 2.1

With few exceptions, the MDT chambers are composed of two multilayers of drift tubes separated by support frames (see Figure 2.3) consisting of three cross plates interconnected

*About 500 ppm of water are added to the gas mixture to increase the high-voltage stability and avoid cracking of the end-plugs due to drying out. The influence on the drift properties is negligible.

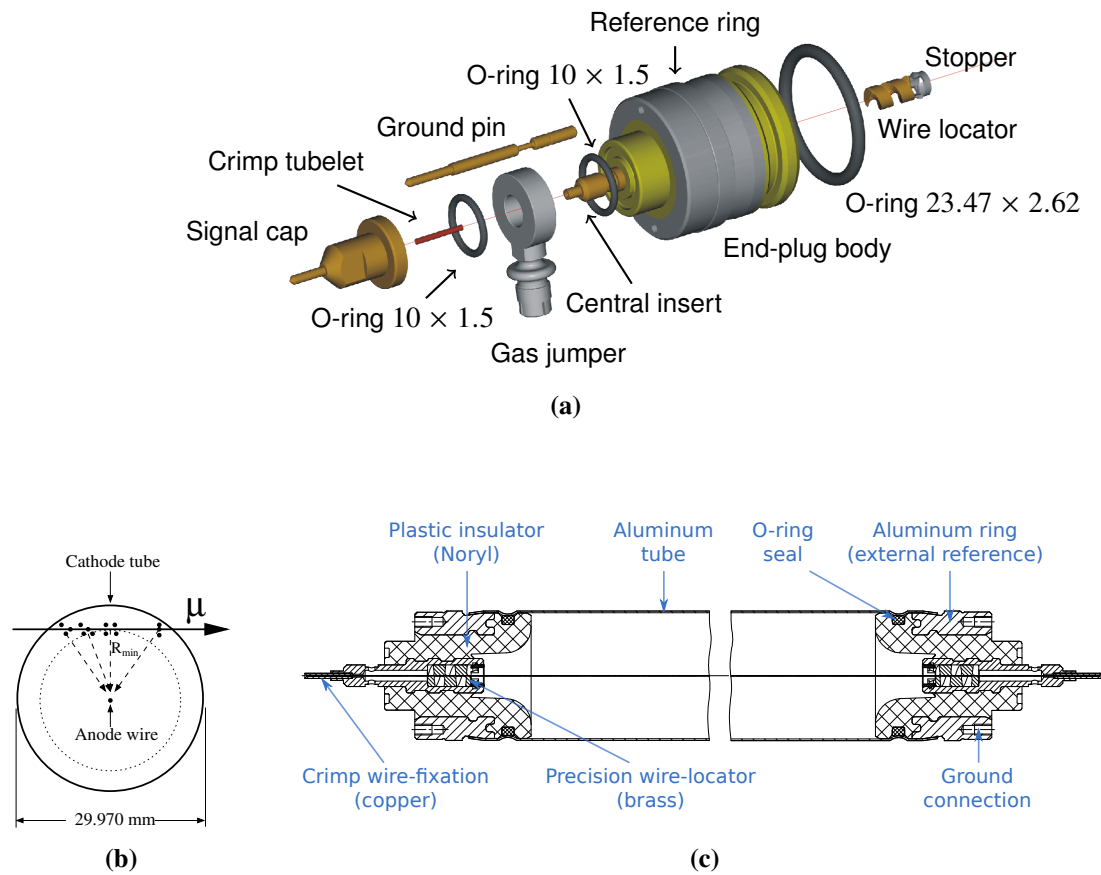


Figure 2.1: Exploded view of the MDT end-plug (a) and cross sections of an MDT drift tube in (b) transverse and (c) longitudinal direction [2].

Table 2.1: MDT chamber parameters [2]

Parameter	Design value
Tube material	Aluminium
Outer tube diameter	29.970 mm
Tube wall thickness	0.4 mm
Wire material	Gold-plated W/Re
Wire diameter	50 μ m
Gas mixture	Ar/CO ₂ /H ₂ O (93/7/ \leq 1000 ppm)
Gas pressure	3 bar (absolute)
Gas gain	$2 \cdot 10^4$
Wire potential	+3080 V
Maximum drift time	760 ns
Average drift tube spatial resolution (with time slewing correction)	80 μ m

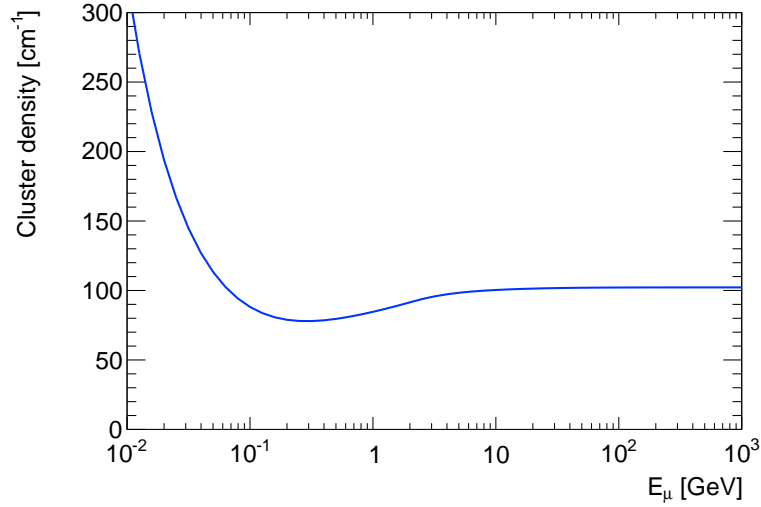


Figure 2.2: Cluster density as a function of the muon kinetic energy at nominal MDT operating parameters (see Table 2.1)

by two long beams in tube direction. An optical alignment system mounted on the support frame is used to monitor deviations from planarity under gravitational sag, mechanical stress and thermal gradients [27]. The MDT chambers in the barrel region are rectangular while they have trapezoidal shape in the end-caps.

The drift tubes are glued together in the multilayers with a wire positioning precision of better than $20\ \mu\text{m}$. The chambers in the middle and outer layer of the Muon Spectrometer have three drift tube layers per multilayer, while the chambers in the inner layer consist of four tube layers per multilayer to cope with the higher radiation background.

The middle cross plate can be moved with respect to the outer ones to compensate for the gravitational sag of the chambers and adjust it to the sag of the anode wires in order to maintain concentricity with the tube wall over the whole tube length.

To achieve a stand-alone muon momentum resolution of the Muon Spectrometer of $\sigma_{p_T}/p_T \approx 10\%$ for transverse momenta of $p_T = 1\ \text{TeV}$, the MDT chambers have been designed to reach a spatial resolution of $35\ \mu\text{m}$, which requires knowledge of the wire positions within a chamber of better than $20\ \mu\text{m}$ and an average single-tube resolution of $80\ \mu\text{m}$. The drift tube resolution will be discussed in more detail below.

In order to achieve this resolution, variations of the operating parameters, like temperature, gas pressure and composition and the magnetic field strength, have to be monitored with high precision and taken into account in the calibration of the $r(t)$ relation.

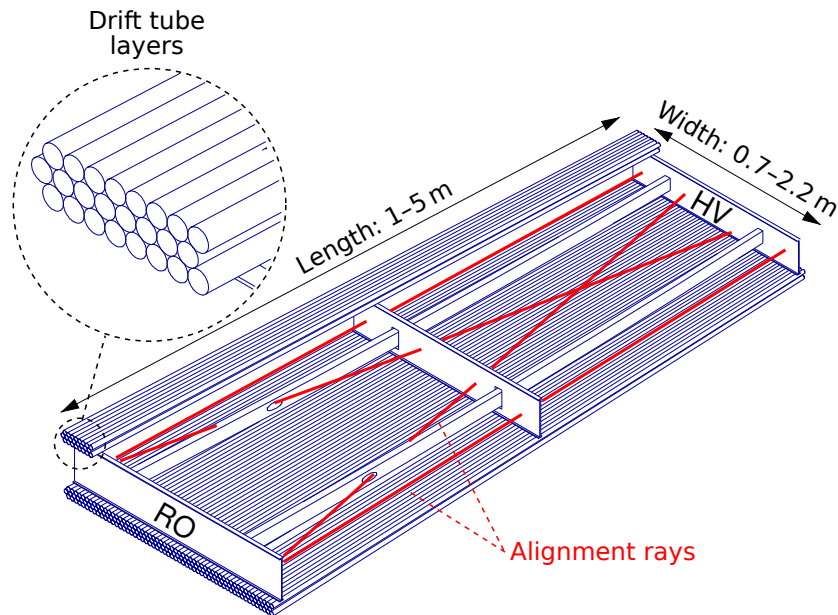


Figure 2.3: Schematic view of an ATLAS MDT chamber in the barrel region [2].

2.2.2 Front-End Electronics

The MDT front-end electronics comprises passive signal and high-voltage distribution boards, active read-out boards and detector control and monitoring units. A photograph of the MDT on-chamber electronics components is shown in Figure 2.4.

Passive Electronics Boards

Figure 2.5 gives an overview of the services connected to the drift tubes. The electrical connections to the anode wires and the tube walls are provided by passive so-called hedgehog boards via signal caps and ground pins on the end-plugs (see Figure 2.1). Each hedgehog board connects to 3×8 tubes in three-layer multilayers, and to 4×6 tubes in four-layer multilayers.

On the chamber end, the high-voltage hedgehog boards connect the tubes to the high-voltage supply via a 383Ω terminating resistor matching the tube impedance and a low-pass filter composed of a $1 \text{ M}\Omega$ resistor and a 470 pF capacitor cutting off noise with frequencies $>500 \text{ Hz}$. The $1 \text{ M}\Omega$ resistor also limits the current in case of a short, e.g. caused by a broken wire, until the high-voltage has been switched off. Additional low-pass noise filters with a cut-off frequency of approximately 725 Hz are installed close to the chamber in the high-voltage supply lines connecting each tube layer individually to further suppress pick-up noise. The circuit diagram is shown in Figure 2.6.

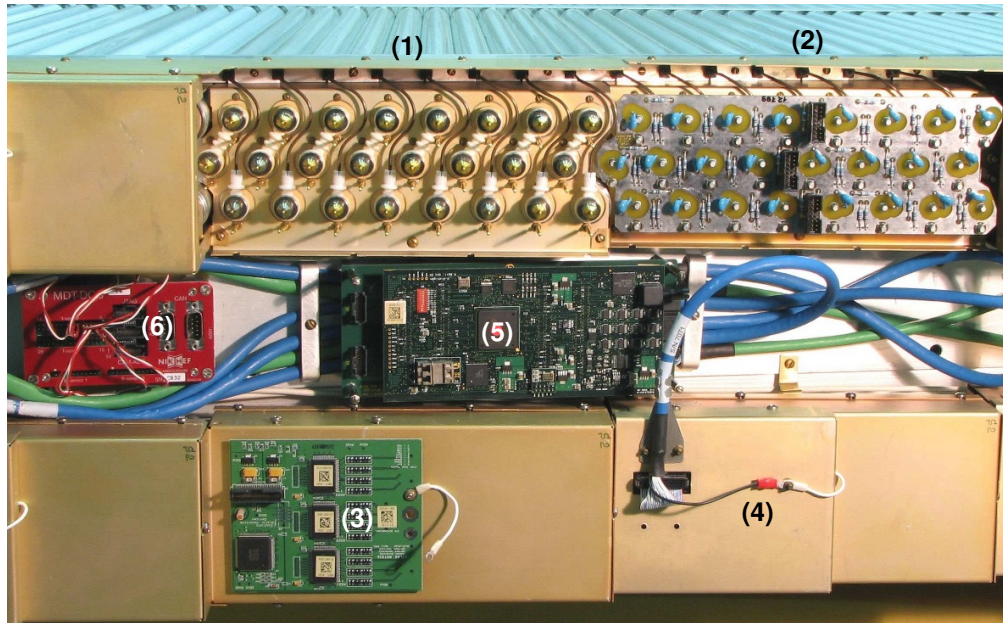


Figure 2.4: Photograph of the read-out end of an 2×3 layer MDT elx where the different electronics components are visible in sections of 3×8 tubes. In section (1) the bare tube ends with signal caps screwed on the end plugs and the gas supply tubelets are visible. Section (2) shows a signal hedgehog board attached to the tube ends via pins on the signal caps. In section (3) a mezzanine board is plugged onto the hedgehog board shielded by the inner Faraday cage cover. In section (4) the mezzanine board is enclosed in its own Faraday cage and connected via the blue shielded twisted-pair cable to the Chamber Service Module (CSM) (5), which collects the data from the drift tubes of a chamber and transmits it via an optical fibre cable to the data acquisition system. The red box (6) is the Muon Detector Control Module (MDM) [28].

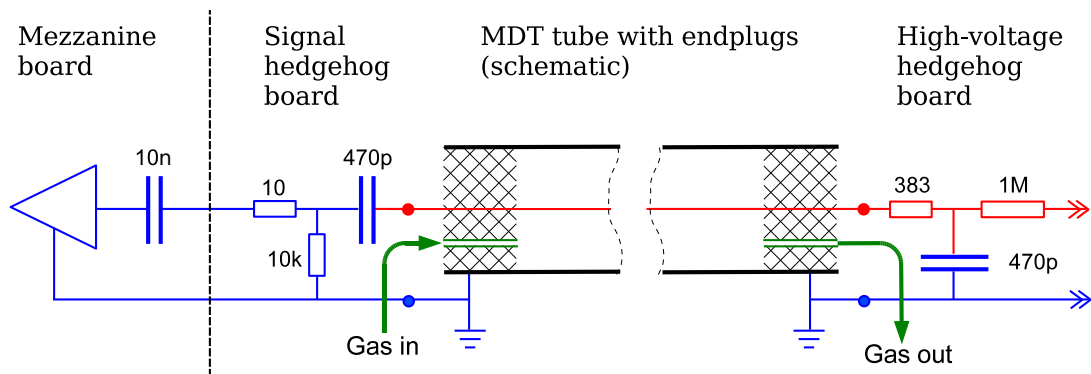


Figure 2.5: Electrical connections to an MDT drift tube. On the high-voltage side, the wire is terminated with the drift tube impedance of $383\ \Omega$ to avoid signal reflections. All electrical contacts between the tubes and the hedgehog boards (marked by dots) are gold-plated to ensure long-term stability [28].

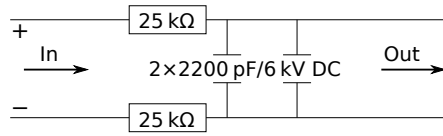


Figure 2.6: Circuit diagram of the noise filters used in the high-voltage connections to suppress pick-up noise [29].

Table 2.2: ASD analog specifications [30]

Input impedance	$Z_{in} = 120 \Omega$
Noise	$\sigma_{ENC} = 6000 e^-$ equiv. to 5 primary e^- (pe^-) (at gas gain $2 \cdot 10^4$)
Shaping function	bipolar
Shaper peaking time	$t_p = 15 \text{ ns}$
Sensitivity at discriminator input	$1.65 \text{ mV}/pe^-$ (at gas gain $2 \cdot 10^4$) equiv. to $8.9 \text{ mV}/fC$
Linear response range	1.5 V or $900 pe^-$
Nominal discriminator threshold	40 mV or $24 pe^-$ (equiv. to $5 \sigma_{ENC}$)

On the signal hedgehog boards on the opposite chamber end, a 470 pF capacitor decouples the read-out boards from the high-voltage. Two resistors form a protection network for the attached mezzanine boards carrying the active front-end electronics.

Active Front-End Electronics

Each signal hedgehog board is connected to a mezzanine board containing the ASD (Amplifier/Shaper/Discriminator) and TDC (Time-to-Digital Converter) chips.

The ASD [30] contains fully differential preamplifier, shaper and discriminator stages for 8 channels with the main specifications summarised in Table 2.2. Each mezzanine board contains 3 ASD chips for in total 24 drift tubes. Bipolar shaping was chosen in order to avoid baseline shift at high counting rates (see section 3.4). Figure 2.7 shows a block diagram of one ASD channel. After passing the amplification and shaping stages, the signals pass a discriminator (DISC1) with programmable threshold. The first threshold crossing time defines the arrival time of the signal.

The ASD can be operated in charge measurement (ADC) or time-over-threshold (ToT) mode. In ToT mode, the ASD digital (LVDS) output signal length corresponds to the time the analogue signal exceeds the threshold while in ADC mode it corresponds to the signal charge. The main application of the charge measurement is correction for time slewing, the dependence of the threshold crossing time on the signal amplitude. Smaller signals cross the discriminator threshold later than large signals resulting in a systematic variation in the drift time. Time slewing corrections using the charge measurement are described in section 4.3.3.

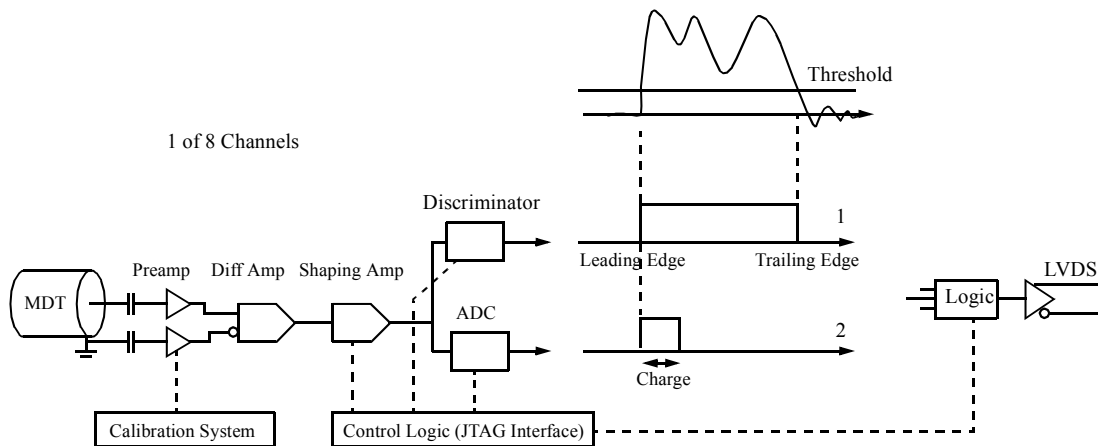


Figure 2.7: Block diagram of one ASD channel [28] (see text). The ASD chip can be operated (1) in time-over-threshold or (2) charge measurement mode.

The signal amplitude is measured by the charge in the rising edge with a Wilkinson ADC (Analogue-to-Digital Converter), hence a short integration gate with default width of 18.5 ns is used. The MDT signals can have a complicated shape and extend up to the maximum drift time of the tubes of 760 ns due to afterpulses of subsequently arriving ionisation clusters (see below).

Figure 2.8 shows the response of the Wilkinson ADC. A holding capacitor is charged during the integration time window, which is opened when the discriminator threshold is crossed. At the end of the integration gate, the rundown gate is opened and the holding capacitor is discharged with constant current until it falls below the threshold of a second discriminator (DISC2) terminating the rundown gate. The ADC digital output is the logic OR of the integration and rundown gate lengths.

Figure 2.9 shows the simulated response of the ASD to delta pulses with different integral charge. On purpose the response is not linear over the whole dynamic range in order to optimise the resolution of the charge measurement for small signals that are subject to stronger time slewing. The calibration curve translating the Wilkinson ADC response into signal charge is depicted in Figure 2.10. The smaller slope for low ADC counts improves the charge resolution for small signals.

The bipolar shaping together with the length of the MDT signals of up to 760 ns can cause multiple threshold crossings per hit increasing the required buffer size and read-out bandwidth. As only the first threshold crossing is of interest, adjustable additional dead time is implemented in the ASD chip. In ATLAS the maximum dead time setting is used which corresponds approximately to the maximum drift time of 760 ns. The overall dead time value depends on the operation mode and is the sum of the programmable dead time and the pulse length. In ToT mode the pulse length

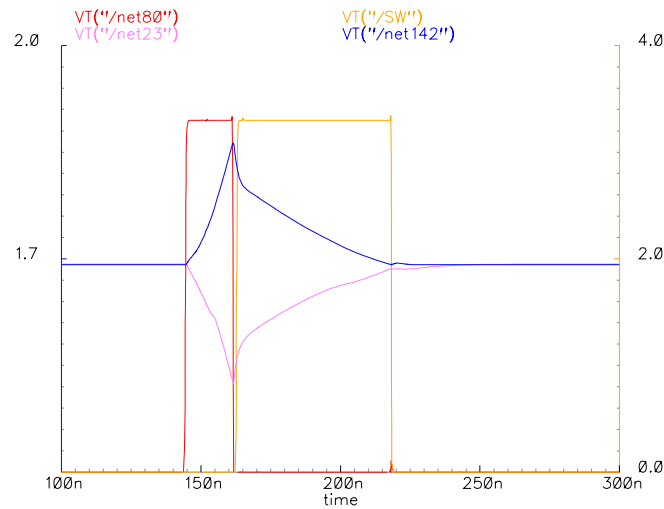


Figure 2.8: Response of the Wilkinson ADC of the ASD chip to a typical muon pulse. The digital signals are the integration gate (red) and the rundown gate (yellow). The integration gate is opened when the main discriminator threshold is crossed and has a programmable width (default value 18.5 ns) during which a holding capacitor (blue and purple) is charged up. At the end of the integration gate, the rundown gate is started and the holding capacitor discharged with a programmable constant current until the charge is zero which is sensed by another discriminator with programmable threshold. The output signal is formed as logic OR of the integration and rundown gate lengths [30].

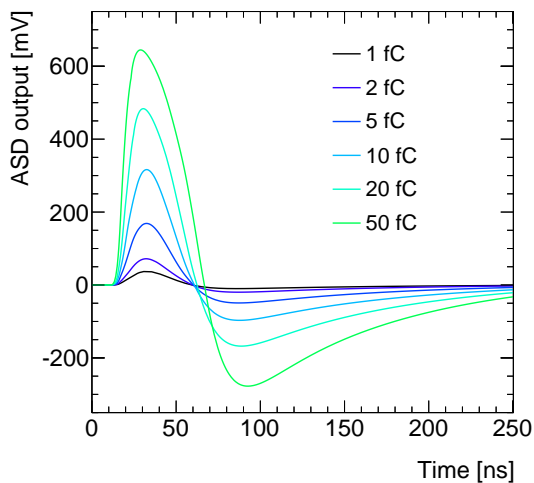


Figure 2.9: Simulated delta pulse response of the ASD chip.

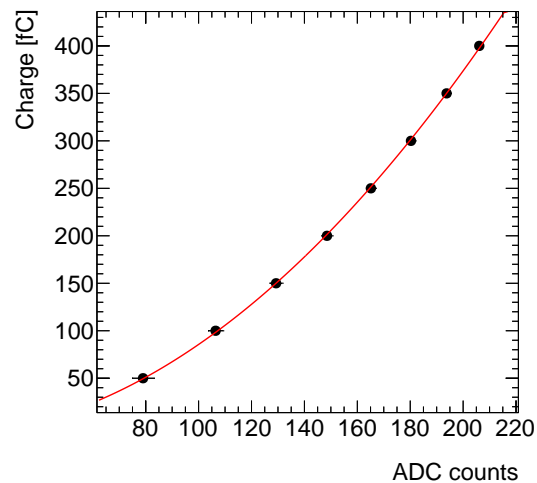


Figure 2.10: Calibration curve for the charge measurement of the Wilkinson ADC.

Table 2.3: Ranges and nominal values of the ASD operation parameters [30, 31]. Alternative to the ADC measurement also the time-over-threshold (ToT) information can be read out depending on the DCS settings.

Parameter	ATLAS nominal value	Range	Unit
DISC1 threshold	-38	-254–256	mV
DISC1 hysteresis	8.75	0–19	mV
Wilkinson ADC integration gate	18.5	8–45	ns
DISC2 threshold	94	32–256	mV
Wilkinson discharge current	4.5	2.4–7.3	μ A
Dead time ¹	820	220–820	ns
Channel mode	ON	ON, HI, LO	—
Operation mode	ADC	ADC, ToT	—

¹ The actual dead time varies between chips and also depends on the signal shape as well as on the operation mode and other operating parameters like the Wilkinson ADC integration gate, the rundown current and the DISC2 threshold. The specified values are measured ones (see section 5.3.1).

is the time-over-threshold while in ADC mode it is the length of the integration and run-down gates. The programmable dead time varies between chips, the ASD user’s manual specifies a maximum value in the neighbourhood of 600 ns. The overall dead time measured in chapter 5 is 220 ns for the minimum and 820 ns for the maximum dead time settings. The programmable ranges of the ASD operating parameters and the nominal values used in ATLAS are summarised in Table 2.3.

The digital (LVDS) output signals of each of 3 ASD chips on a mezzanine board are fed to a TDC chip designed specially for the ATLAS MDT chambers, the AMT-3* chip [32]. The AMT chip contains a 24-channel time-to-digital converter with 0.78125 ns time resolution for both the leading and trailing edges of the ASD digital signals. The leading edge corresponds to the electron arrival time, the time between leading and trailing edge to the time-over-threshold or the signal charge depending on the operation mode used with the ASD. Besides the time digitisation functionality it contains several buffer stages and a trigger matching mechanism that allow for keeping all hit information for several milliseconds until a trigger decision is taken by the central trigger processor and the information is read out or discarded from the buffers. At nominal parameter settings, each of the 24 channels can be operated without relevant data loss up to counting rates of 400 kHz and a trigger rate of 200 kHz without relevant data loss.

The digital data of each MDT chamber are collected by the chamber service module (CSM) and transmitted to the data acquisition system via an optical fibre. The CSM is connected by

*Atlas Muon TDC, version 3

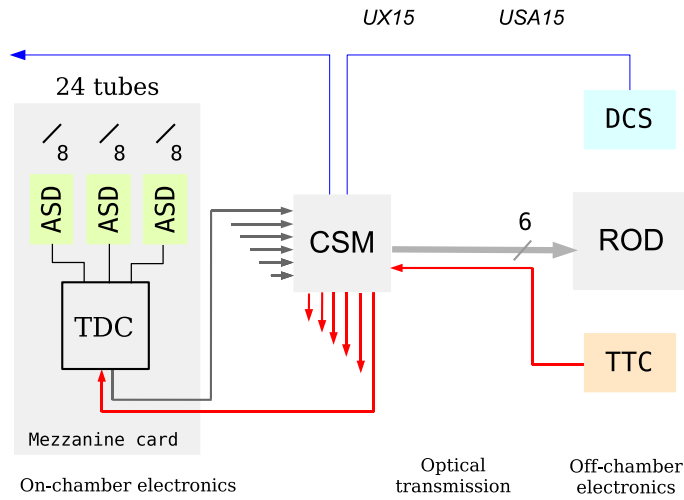


Figure 2.11: Schematic diagram of the MDT readout electronics [2].

a cable to each individual mezzanine card of a chamber, passes on trigger and global timing information from the Trigger and Control (TTC) system as well as the detector control (DCS) signals, serialises the data of the AMT-3 chips and supplies the mezzanine boards with low-voltage.

A schematic diagram of the MDT on- and off-chamber electronics is shown in Figure 2.11. The CSM is connected to the read-out driver (ROD) in the service cavern by an optical fibre while another fibre connects it to the TTC system. A third data path is used for the lower-speed detector control system (DCS). Each MDT chamber is equipped with an MDT-DCS Module (MDM) which initialises and monitors the on-chamber electronics settings via a JTAG protocol and reads the temperature and magnetic field sensors on the chamber. Communication with the MDMs is provided by the CAN bus* system.

2.2.3 Performance of the ATLAS MDT Chambers

The performance of the MDT chambers has been studied extensively in beam tests prior to their operation in ATLAS [33–36]. Figure 2.12 shows the MDT single-tube resolution as a function of the drift radius with and without time slewing correction (see section 4.3.3). The spatial resolution improves from approximately $200\ \mu\text{m}$ in the vicinity of the wire to approximately $60\ \mu\text{m}$ for drift radii $r \gtrsim 7\ \text{mm}$.

The dependence of the spatial resolution on the drift radius can be explained by simple

*Controller Area Network

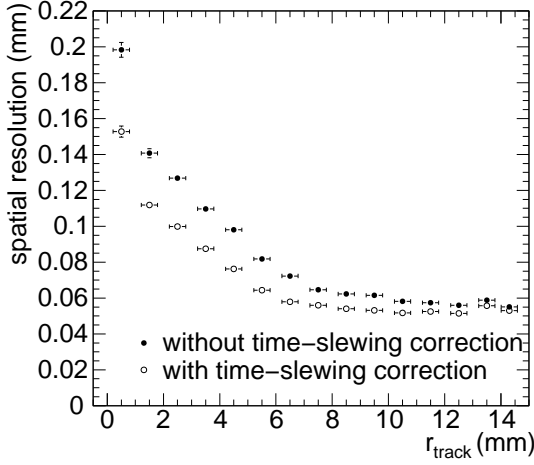


Figure 2.12: Dependence of the single-tube spatial resolution on the drift radius determined from an external reference measurement with and without time slewing correction [35].

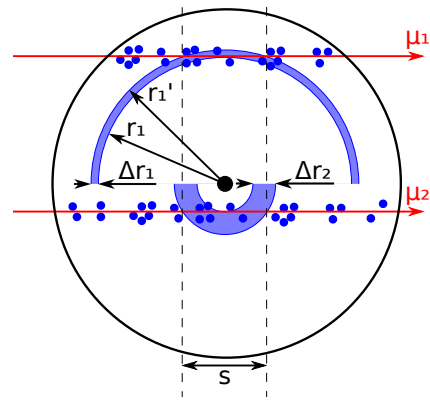


Figure 2.13: The improvement of the spatial resolution with increasing drift radius can be understood from simple geometrical considerations (see text).

geometrical considerations illustrated in Figure 2.13. Let s be the length of the section of the ionisation path containing the necessary number of primary ionisation electrons n for crossing the discriminator threshold. The difference in the distance of the first and the last ionisation cluster of this section to the wire is

$$\Delta r = r' - r = \sqrt{\frac{s^2}{4} + r^2} - r \xrightarrow{r \rightarrow 0} \frac{s}{2},$$

increasing steeply to $s/2$ towards the wire. For $s \ll r$, Δr becomes negligible. With a cluster density of $\sim 100 \text{ cm}^{-1}$, an average cluster size of ~ 3 primary electrons and a discriminator threshold equivalent to $n = 20$ primary electrons, s is about 0.67 mm. For larger drift radii, fluctuations Δs of s become important. The drift radius of the n^{th} ionisation cluster,

$$r' = \sqrt{\frac{s^2}{4} + r^2},$$

fluctuates by

$$\Delta r' = \frac{s \Delta s}{2\sqrt{s^2 + 4r^2}} = \frac{s \Delta s}{4r'}$$

which translates into fluctuation Δt of the drift time by

$$\Delta t = \frac{\Delta r'}{v(r')} = \frac{s \Delta s}{4r'} \frac{1}{v(r')}.$$

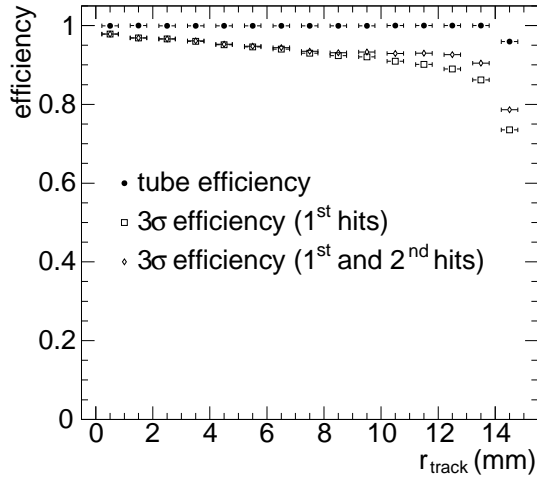


Figure 2.14: Dependence of the hit and the 3σ -efficiency of the drift tubes on the drift radius depending on the number of hits taken into account in the read-out window [35].

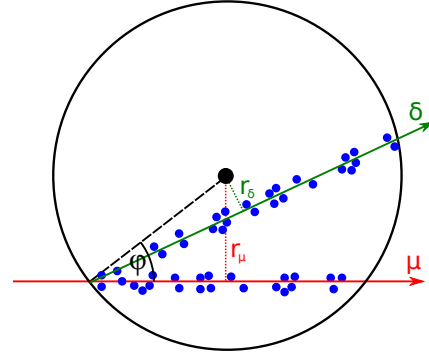


Figure 2.15: Illustration of the effect of δ -electrons knocked out of atoms in the tube wall by the muons on the tube efficiency (see text).

If $r \gg s$, then $r \approx r'$ and hence

$$\Delta t \approx \frac{s \Delta s}{4r} \frac{1}{v(r)}$$

In the range $0.5 \text{ mm} \lesssim r \lesssim 5 \text{ mm}$, where the electron drift velocity $v(r)$ is approximately constant (cf. Figure 3.6). This implies a r^{-1} behaviour of the time and, therefore, spatial resolution.

For $r \gtrsim 5 \text{ mm}$ the drift velocity is approximately proportional to r^{-1} (compare Figure 3.6), such that Δt is independent of r . The expected behaviour of the spatial resolution,

- approximately constant for $r \gtrsim 5 \text{ mm}$,
- proportional to r^{-1} in the range $0.5 \text{ mm} \lesssim r \lesssim 5 \text{ mm}$ and
- approaching $s/2 \approx 0.3 \text{ mm}$ near the wire,

agrees very well with the measurement shown in Figure 2.12.

Figure 2.14 shows the dependence of the drift tube efficiency on the drift radius. Two different efficiency measures are shown, the hit efficiency and the so-called 3σ -efficiency. While the hit efficiency is defined as the probability of detecting a hit independent of the measured drift radius, the 3σ -efficiency requires in addition that the detected hits have a drift radius matching the expected value from an external reference measurement within 3 times the spatial resolution as a function of r , which is relevant for the track reconstruction efficiency in the Muon Spectrometer.

The hit efficiency is 100% for $r \lesssim 14 \text{ mm}$ and drops slightly in the vicinity of the tube wall where the ionisation path becomes very short. The 3σ -efficiency is only 100% close to the wire

and decreases with increasing r . The reason for this efficiency loss are δ -rays, fast electrons knocked out of atoms by the muons, which mainly occurs in the tube walls where the density is much higher than in the gas volume. Figure 2.15 illustrates the masking of muon hits by δ -electrons. For isotropic δ -electron emission around the muon impact point, the probability of masking a muon hit is

$$P_{\text{mask}} \propto \frac{\varphi}{\pi} = \frac{1}{\pi} \arcsin \frac{r_{\mu}}{r_{\text{max}}}.$$

The dependence of the 3σ -efficiency on the drift radius is then

$$\epsilon(r) = 1 - P_{\delta} \cdot P_{\text{mask}} = 1 - \frac{P_{\delta}}{\pi} \arcsin \frac{r_{\mu}}{r_{\text{max}}},$$

with the probability for δ -electron emission P_{δ} which is on the order of 10 % according to simulation [37]. The overall 3σ -efficiency of the MDT tubes is, therefore, about 95 %.

2.2.4 Performance in the Presence of Radiation Background

The majority of the hits in the ATLAS MDT chambers does not originate from muons but from radiation background. The Muon Spectrometer is permeated by a high background of photon and neutron radiation with energies on the order of 1 MeV created in secondary reactions of the proton collision products in the beam pipe, the shielding and the detector material. The overall background rate scales with the instantaneous LHC luminosity.

The background hits cause a degradation of the spatial resolution and 3σ -efficiency of the MDT drift tubes due to effects described in detail in the following chapter. Figure 2.16 shows the measured dependence of the average MDT drift tube resolution and 3σ -efficiency on the photon background flux. The measurements have been performed at the Gamma Irradiation Facility [38] which simulates the radiation background in the ATLAS cavern.

At the highest expected rates of 500 Hz/cm², the average single-tube spatial resolution degrades from 80 μm to about 120 μm and the 3σ -efficiency from 95 % to about 88 % at the maximum electronics dead time setting. With the upgrade of the LHC to HL-LHC, the background flux is expected to increase by a factor of 5 proportional to the luminosity. In the following section, new drift tube chambers with reduced tube diameter are discussed which are characterised by a much higher rate capability than the MDT chambers sufficient for operation at HL-LHC even in detector regions where the background flux is too high for MDT chambers already at nominal LHC luminosity.

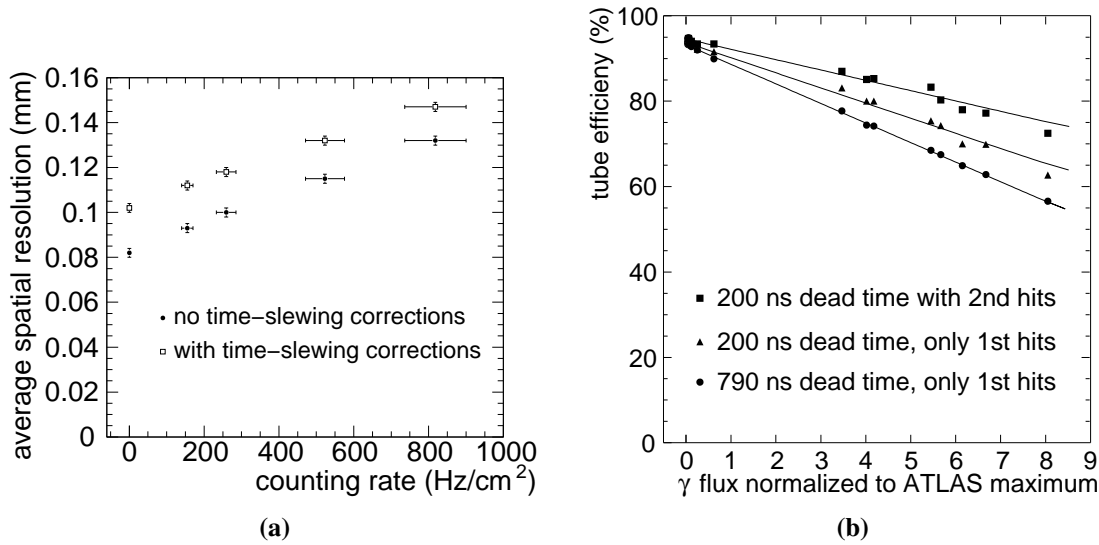


Figure 2.16: Dependence of the average single-tube (a) spatial resolution and (b) 3σ -efficiency on the photon background rate. The maximum expected background rate in the MDT chambers at nominal LHC luminosity is 500 Hz/cm^2 . The 3σ -efficiency is shown for minimum and maximum adjustable electronics dead time and depending on the number of hits taken into account in the read-out window [35].

2.3 Small-Diameter Muon Drift Tube Chambers

A new type of MDT chambers with reduced outer tube diameter of 15.000 mm instead of 29.970 mm, called Small-Diameter Muon Drift Tube (sMDT) chambers [39, 40], has been developed in order to increase the rate capability by about an order of magnitude, while maintaining compatibility with the MDT chamber services and read-out in the ATLAS detector. Therefore, all operating parameters except the tube diameter are kept. The sMDT chambers are operated with the same gas mixture and pressure and the same gas amplification of $2 \cdot 10^4$ as the MDT chambers resulting in a slightly lower wire potential of +2730 V instead of +3080 V.

A photograph of MDT and sMDT drift tubes in comparison is shown in Figure 2.17. The improved rate capability of the sMDT chambers in comparison with the MDT chambers is discussed in chapter 3. A further advantage of sMDT chambers is the smaller chamber height which allows for installation in up to now uninstrumented regions of the Muon Spectrometer or more tube layers for higher tracking redundancy.



Figure 2.17: Photograph of sMDT (left) and MDT (right) drift tubes.

2.3.1 Technical Implementation

The main technical challenges of the sMDT chambers arise from the four times higher packing density compared to the MDT chambers limiting the space for service connections and complicating the high-voltage stability.

The Drift Tubes

Figure 2.18 shows an exploded view of an sMDT tube. The central component is the end-plug consisting of insulating plastic (Crastin) with a precisely machined brass insert. A brass insert carries in a fitting hole on the inside of the tube a helical-shaped so-called twister with inner diameter equal to the anode wire diameter to position the wire with few micron precision with respect to a cylindrical reference surface on the brass insert protruding from the plastic body of the end-plug to the outside of the tube. The external reference surface is used to position the tubes (and hence the wires) accurately with respect to each other during the chamber assembly and to measure their coordinates at the tube ends with a coordinate measuring machine (CMM).

A small copper crimp tubelet inserted in the brass piece is used to fix the anode wire after tensioning to 350 g and establishes the electrical connection to the brass insert. The end-plugs are fixed in the aluminium tubes by crimping the tube wall. O-ring seals make the connection gas tight.

In contrast to the MDT chambers, the sMDT chambers do not have individual ground connection of the tube wall via the end-plug because of lack of space and cost saving. Instead, ground connectors are screwed into the space between three adjacent tubes during chamber assembly. The electrical connection to the anode wire is established via a signal cap with gold plated contact pin screwed onto the brass insert which also seals the tube via O-rings with the injection-moulded plastic gas connector in between.

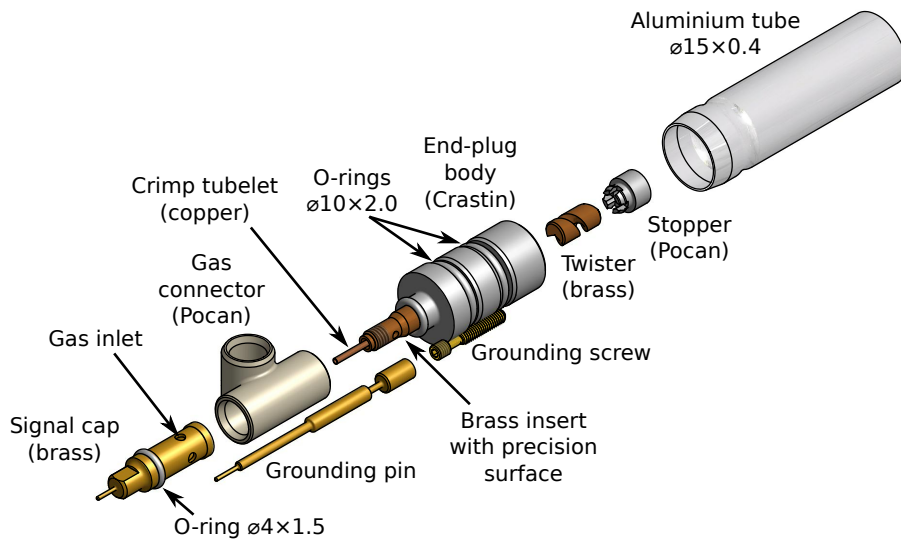


Figure 2.18: Exploded view of an sMDT drift tube.

Chamber Assembly

Each assembled drift tube is tested for gas tightness, high-voltage stability and wire tension before it is assembled in a chamber. The first step in the sMDT chamber assembly is the gluing of drift tubes to multilayers. In contrast to the MDT assembly, where the tube layers were glued one after the other to the support frame and the glue cured over night, the sMDT multilayers can be glued in one step, enabled by the use of new end-plug design and special two-dimensional assembly jiggling which keeps the tubes in position until the glue is cured (see Figure 2.19a).

A multilayer is built by stacking layers of drift tubes. Before a new layer is added, the former one is locked into position by a “comb” which encloses the precise reference surfaces of the end-plugs. An automated glue dispenser, shown in Figure 2.19b, distributes the glue on top of the last tube layer. In the next step, the two multilayers are glued to the support frame using special jiggling to achieve precise alignment of the multilayers with respect to each other. After the gluing of the tube layers, the gas distribution system is mounted.

All of the above assembly steps are carried out in a temperature controlled clean room to prevent disturbances of the chamber geometry. A photograph of an sMDT chamber with mounted gas distribution system is shown in Figure 2.19c.

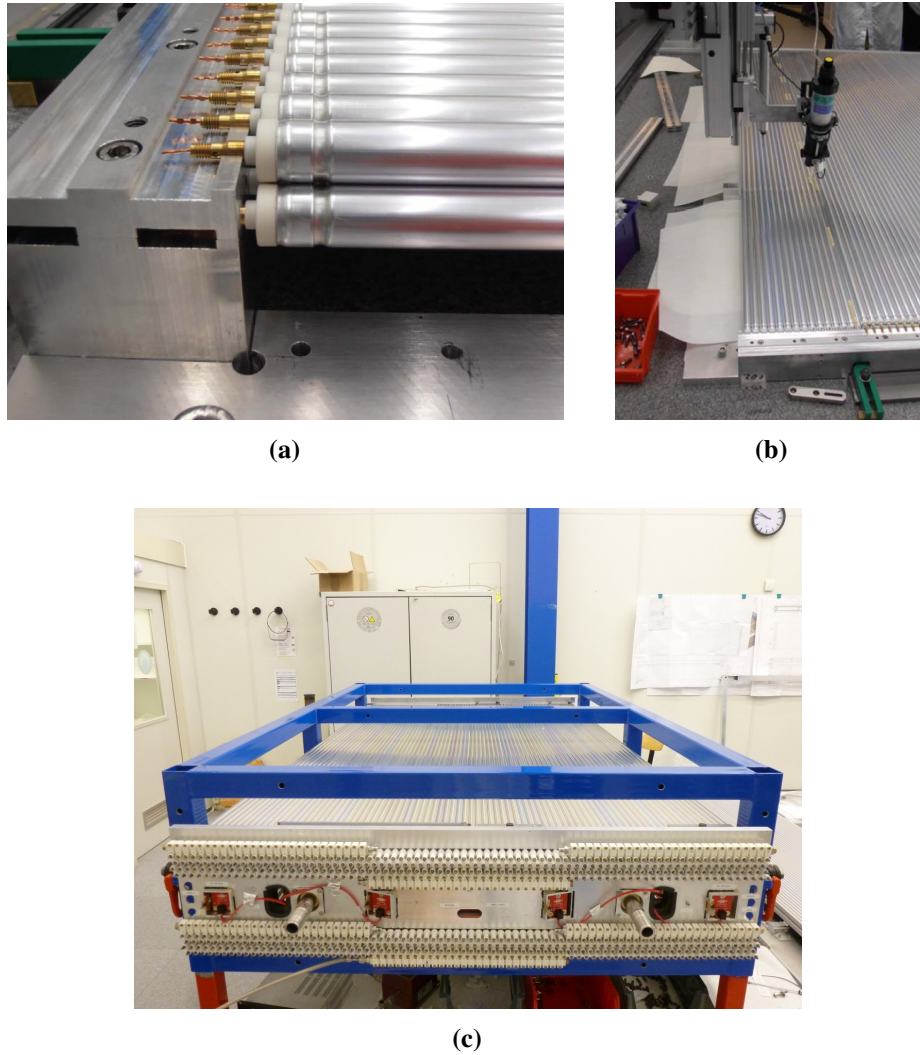


Figure 2.19: Photographs of the different stages of the sMDT chamber assembly: (a) the first two drift tube layers of a multilayer in the assembly jigging, (b) application of glue with an automated glue dispenser, (c) assembled chamber with two multilayers, the support frame carrying the optical in-plane alignment system and with the gas distribution system mounted.

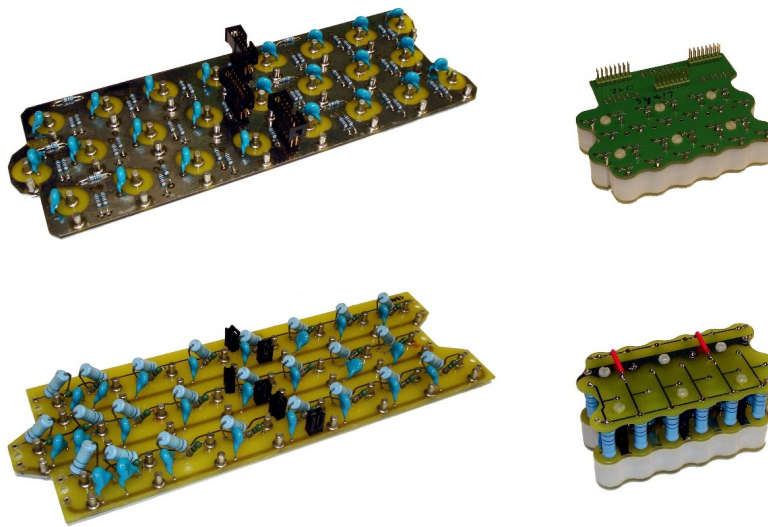


Figure 2.20: Photographs of the (top) signal and (bottom) high-voltage hedgehog boards for (left) MDT and (right) sMDT chambers with the passive components for 24 channels each. A 3-dimensional layout using multiple PCBs and individual plastic housing for the high-voltage capacitors was chosen for the sMDT hedgehog boards to achieve good high-voltage stability despite the higher packing density.

The Read-Out Boards

New hedgehog boards matching the smaller tube pitch have been designed for the sMDT chambers. The four times higher packing density of the tubes in the sMDT chambers requires special caution with respect to high-voltage stability. A 3-dimensional layout using multiple printed circuit boards and insulating plastic housing for the high-voltage capacitors was chosen. Figure 2.20 shows photographs of the sMDT and MDT signal and high-voltage hedgehog boards in comparison.

2.3.2 The sMDT Prototype Chamber

The first complete sMDT chamber was built in 2010 [41] and is shown in Figure 2.21. In this chamber, three different tube lengths — 55 cm, 75 cm and 95 cm — are used to approximate the trapezoidal shape needed for the end-cap regions of the Muon Spectrometer. The chamber consists of 2×8 tube layers with 72 tubes each and a 90 mm high support frame. With 1152 drift tubes in total, this chamber contains more than twice as many as the largest MDT chamber.

The sMDT prototype chamber has been studied in several beam tests and under photon irradiation at CERN (see chapter 6). Its wire positions have been measured in the cosmic ray test stand at the Ludwig-Maximilians-Universität in Garching in order to validate the mechanical precision of the assembly procedure [42,43]. For these measurements the chamber part with 75 cm



Figure 2.21: The sMDT prototype chamber mounted in a transport frame.

and 95 cm long tubes was equipped with read-out electronics with standard MDT mezzanine boards.

2.3.3 Application of sMDT Chambers in ATLAS

The first two sMDT chambers have been installed in the ATLAS detector in April 2014 during the first long LHC shutdown (LS1) in previously not instrumented detector regions in the middle barrel layer of the Muon Spectrometer in order to improve the muon momentum resolution [17]. A computer model and a photograph of one of these chambers are shown in Figure 2.22. The locations of the two extra chambers in the middle barrel layer of the Muon Spectrometer (BME chambers) are indicated in Figure 2.23.

The next sMDT chambers to be constructed and installed will further improve the coverage of the middle barrel layer of the Muon Spectrometer in the region of the detector feet. Figure 2.23 shows the locations of the 12 additional BMG sMDT chambers to be installed in the winter shutdown 2016/17 of the LHC.

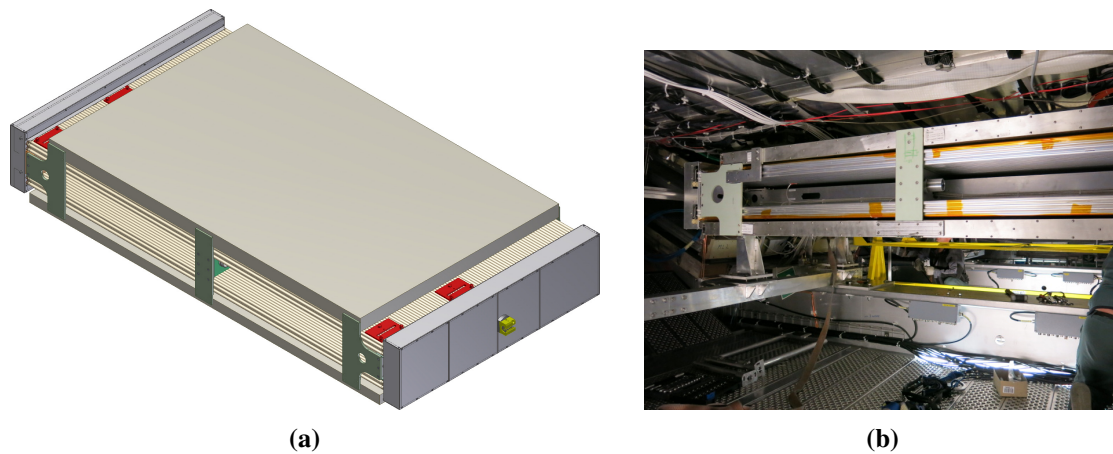


Figure 2.22: CAD model (a) and photograph (b) of a BME (barrel, middle, extra) sMDT chamber installed in April 2014. The chamber consists of 2×4 layers of 15 mm diameter drift tubes with 78 tubes each. The two multilayers are separated by a spacer frame containing the in-plane alignment system which monitors mechanical deformations and enclosed between two Resistive Plate Chambers (RPC) for triggering.

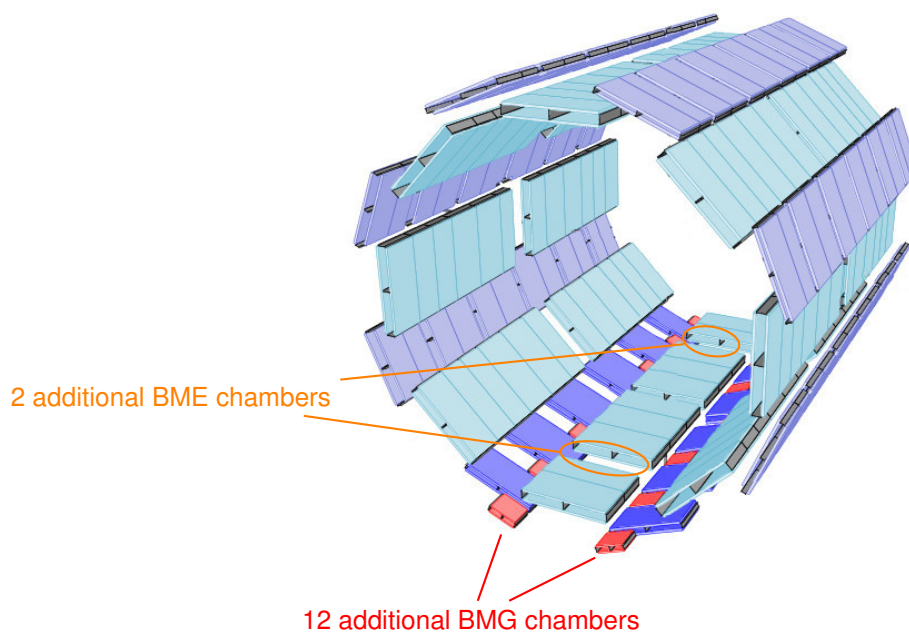


Figure 2.23: The middle layer of the muon spectrometer in the barrel region with the positions of new additional chambers, two in the “elevator region” (BME) and twelve in the “feet region” (BMG), indicated. While the BME chambers have already been installed during the first long shutdown in spring 2014, the BMG chambers are planned to be constructed and installed during the annual Christmas technical stops in the following years.

3

High-Rate Phenomena in MDT and sMDT Chambers

3.1 Introduction

The majority of hits in the MDT chambers are caused by the background radiation which permeates the ATLAS cavern. The background hits produce space charge in the drift tubes which modifies the electric field and hence the drift velocity and the gas amplification and cause degradation of the spatial resolution. In addition, limitations of the front-end electronics with respect to signal shaping and dead time lead to loss of drift tube efficiency and resolution increasing with the background hit rate. The background radiation consists mostly of photons and neutrons with energies of about 1 MeV originating from secondary interactions of proton collision products in the beam pipe, shielding, support structure and the detector components.

The detection efficiencies of the drift tubes for neutrons and photons of around 1 MeV energy have been measured and calculated to be approximately $3 \cdot 10^{-4}$ and $5 \cdot 10^{-3}$, respectively, with 50 % uncertainty [44–46]. Together with simulations of the particle flux (see Figure 3.1), these results determine the expected counting rates of the detectors. A safety factor of 5 was added to account for the large uncertainties in the background flux and detection efficiencies [46]. Measurements during the first LHC runs indicate that the expectations are quite reliable [47, 48].

Radiation induced ageing effects of the MDT chambers have been studied in detail up to a charge accumulation on the wire of 0.6 C/cm (see for example [49]). The consequence of these studies was the choice of an Ar/CO₂ gas mixture in the MDT chambers which contains no hydrocarbons such that deposits on the anode wire due to polymerisation in the avalanches are prevented if there is no contamination of the gas. All materials used in the MDT and sMDT tubes have been qualified against outgassing. sMDT tubes showed no ageing for charge accumulation on the wire up to 9 C/cm [50].

In this chapter, the immediate effects of the background radiation on the performance of drift tube chambers are discussed after a short review of the background rates expected under LHC design and HL-LHC conditions.

3.2 Radiation Background Expectations

The majority of background hits observed in the detectors are uncorrelated in time with the proton–proton collisions and referred to as “cavern background”. Detailed simulations showed that the cavern background increases strongly with decreasing distance to the beam pipe [46]. In the Muon Spectrometer, the highest irradiation regions are around the end-cap toroid magnets (see Figure 3.1). The counting rates in the MDT chambers are shown in Figure 3.2. The highest background flux in the Muon Spectrometer is experienced by the innermost detector layer in the end-cap region, the so-called Small Wheels, followed by the middle end-cap layers, the Big Wheels. The Small Wheels are the only regions where the rate capability of the MDT chambers is not sufficient for HL-LHC. Figure 3.3 shows the expected hit rates in the Small Wheels as a function of the radial distance from the beam line.

3.3 Space Charge Effects

The large number of ions created in the ionisation avalanche in the vicinity of the wire and drifting slowly to the tube wall leads to space charge in the tubes which modifies the electric field. For nominal operating parameters (cf. Table 2.1), the average ion drift time is roughly 3 ms for MDTs and 1 ms for sMDTs. This means, that at the expected high background fluxes space charge is always present in the drift tubes. The space charge shields the wire potential, reduces the gas amplification and causes fluctuations in the drift velocity and the space-to-drift-time relationship $r(t)$ in time which cannot be taken into account in the calibration. The consequences can be seen in Figure 3.4, which shows the radial dependence of the MDT single-tube spatial resolution for different background fluxes. Two effects at small and large drift radii can be distinguished — reduction of the gas amplification and variations of the drift velocity due to space charge fluctuations.

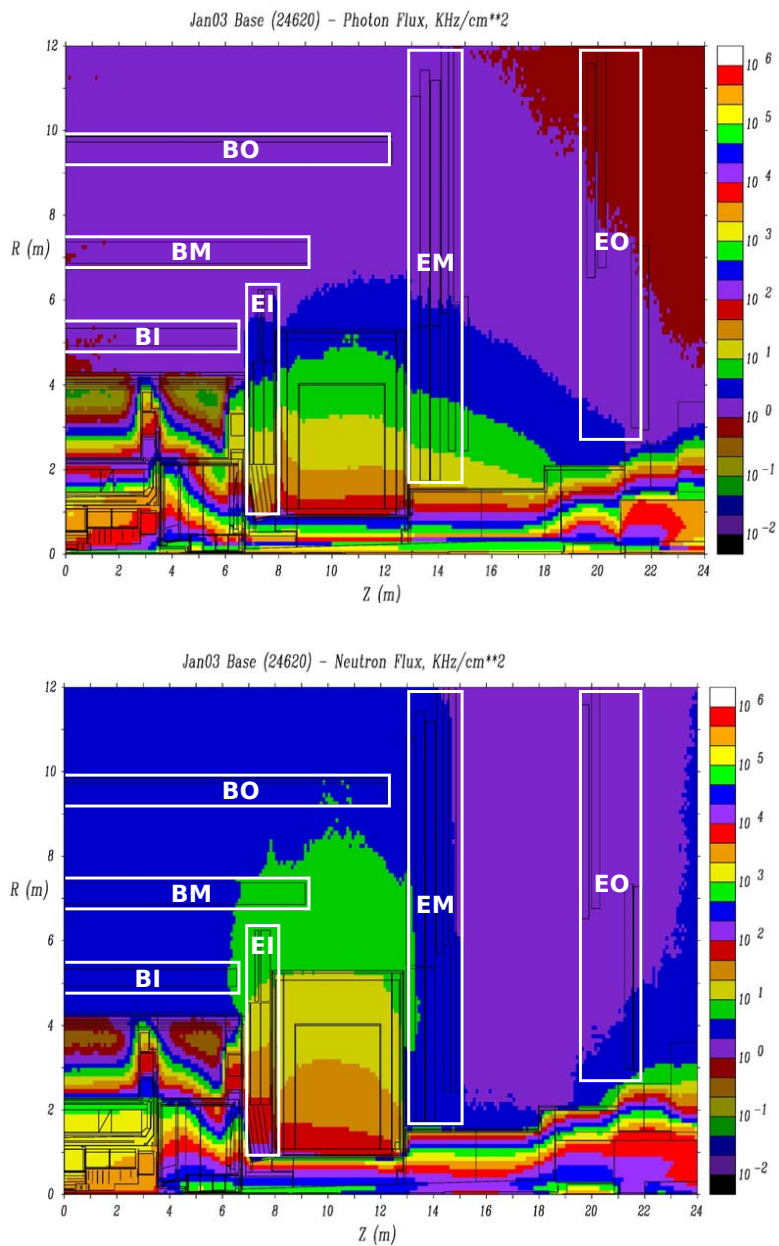


Figure 3.1: Simulated flux of (top) photons and (bottom) neutrons in one quadrant of the ATLAS detector at the LHC design luminosity of $1 \cdot 10^{34} \text{ cm}^{-2} \text{ s}^{-1}$ [46]. The inner (I), middle (M) and outer (O) layers of muon chambers in barrel (B) and end-caps (E) are indicated.

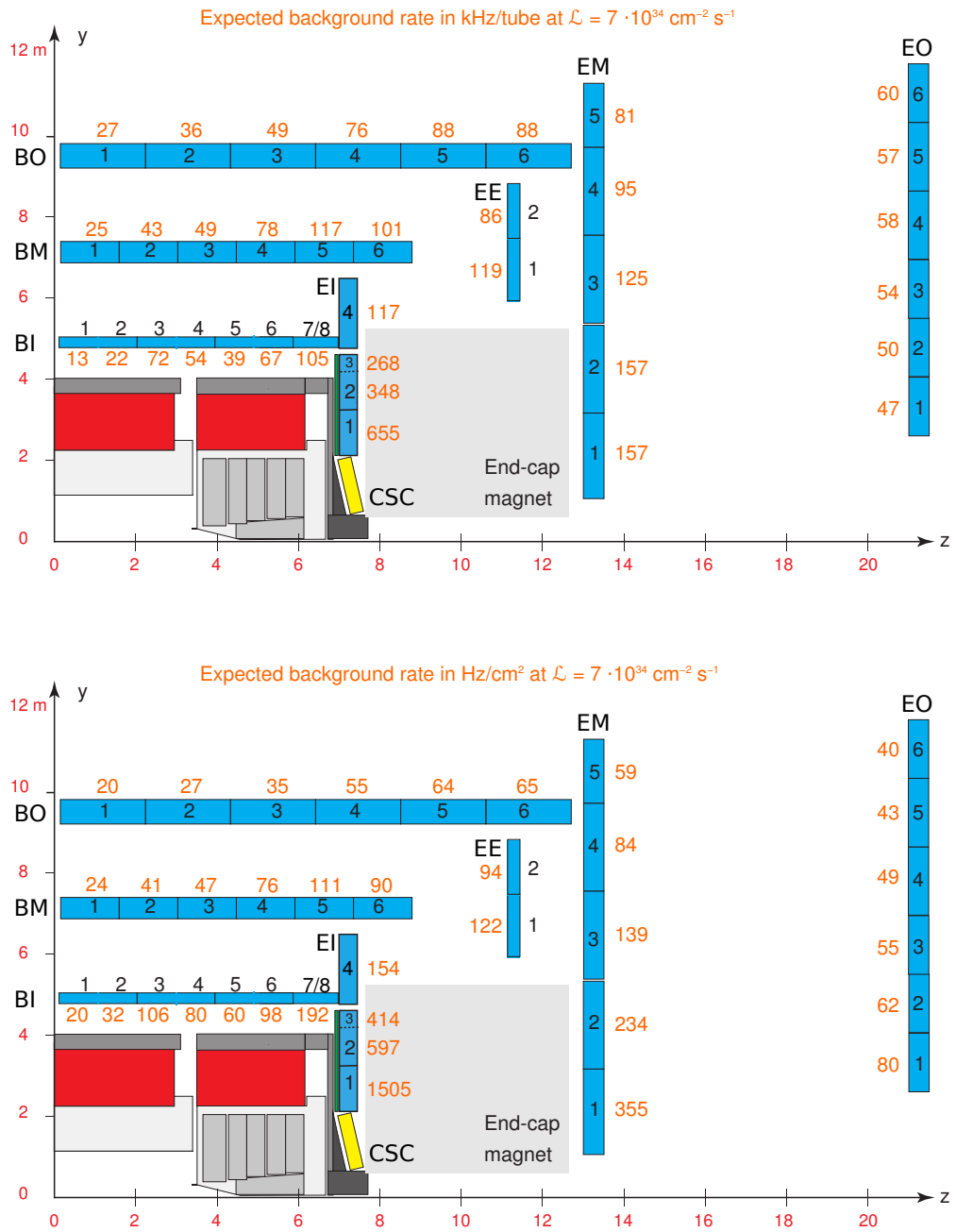


Figure 3.2: Expected background rates in the ATLAS muon chambers (top) per drift tube and (bottom) per cm² at $\sqrt{s} = 8 \text{ TeV}$. The rates have been measured in 2012 data and extrapolated to HL-LHC luminosity of $\mathcal{L} = 7 \cdot 10^{34} \text{ cm}^{-2} \text{ s}^{-1}$. The uncertainty is approximately 10% [51].

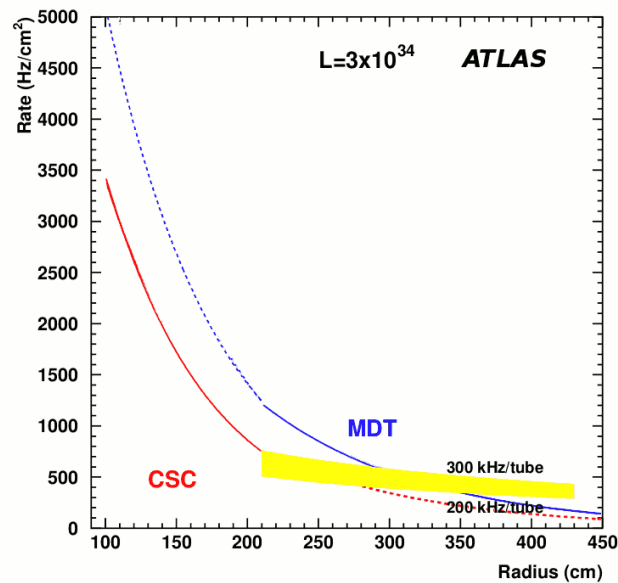


Figure 3.3: Expected hit rate in the inner end-cap layer of the ATLAS Muon Spectrometer, the so-called Small Wheels, as a function of the radial distance from the beam axis for MDT chambers and CSCs (cathode strip chambers) at an instantaneous luminosity of $3 \cdot 10^{34} \text{ cm}^{-2} \text{ s}^{-1}$ and $\sqrt{s} = 7 \text{ TeV}$ [19]. The rate difference between MDT chambers and CSCs is due to the different sensitivity to the background radiation. The expected rate capability of the MDT chambers is indicated by the yellow band. It can be seen that the MDT rate capability is already exceeded at three times the nominal LHC luminosity. In HL-LHC operation, an instantaneous luminosity of up to $7 \cdot 10^{34} \text{ cm}^{-2} \text{ s}^{-1}$ is expected implying a further increase of the background rates by more than a factor of 2.

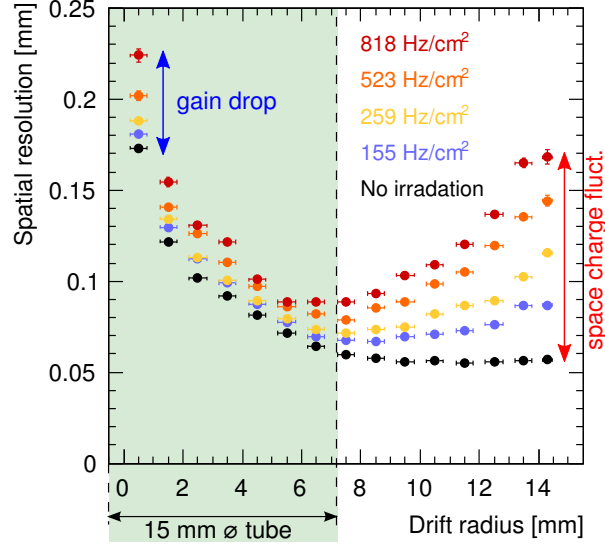


Figure 3.4: Radial dependence of the MDT spatial resolution for different photon irradiation rates [35]. The degradation of the resolution with increasing background flux due to space charge fluctuations is limited to the region $r \gtrsim 6$ mm and increases with the drift distance. Loss of gas gain due to shielding of the wire potential decreases the signal amplitude and increases time slewing, i.e. its contribution follows the radial amplitude dependence of the signal and dominates at small radii.

3.3.1 Gain Drop

The space charge of the slowly drifting ions causes a reduction of the electric field strength in the vicinity of the anode wire and consequently of the gas amplification. With a constant discriminator threshold, a lower gas amplification is equivalent to a higher threshold, which deteriorates the resolution due to additional time slewing.

The gas amplification G in heavy noble gases in the absence of space charge is well modelled by Diethorn's equation [52]

$$\ln G = \frac{r_{\min} E(r_{\min}) \ln 2}{\Delta V} \ln \frac{E(r_{\min})}{E_{\min}(\rho_0) \frac{\rho_{\text{gas}}}{\rho_0}}, \quad (3.1)$$

where r_{\min} is the radius of the anode wire, E the electric field strength, and ρ_{gas} and ρ_0 the actual and the normal gas density, respectively. E_{\min} and ΔV are parameters of the model which have to be measured. E_{\min} can be interpreted as the electric field required to start the avalanche and ΔV as the ionisation potential of the gas. Measured values for Ar/CO₂ (93/7) are $E_{\min} = 24$ kV/cm and $\Delta V = 34$ V [53].

The modification of the electric field E due to the space charge can be calculated in a two-dimensional static model proposed in [53, 54]. In this model, the charge distribution composed of the anode wire line charge density ρ_{wire} and the ion space charge ρ_{ion} is assumed to be cylindrically symmetric around the anode wire. A background hit deposits on average the charge Q_{prim} which is multiplied by the gas amplification factor G in the vicinity of the wire. Hence, the total current per unit length on the wire at an irradiation rate of N_c per unit length is $N_c G Q_{\text{prim}} = \rho_{\text{ion}} \cdot 2\pi r \cdot v_{\text{ion}}(r)$. The charge density ρ_{ion} caused by background hits is then given by

$$\rho_{\text{ion}}(r) = \frac{N_c G Q_{\text{prim}} dt}{2\pi r dr}.$$

The ion drift velocity is $v_{\text{ion}}(r) = dr/dt = \mu E(r)$ with approximately constant ion mobility μ in the low-field region outside the avalanche ($r \gtrsim 100 \mu\text{m}$). Measurements of the mobility of Ar^+ ions in Ar gas can be found in [55, 56]. We use a constant value of $\mu(1 \text{ bar}) = 1.535 \text{ cm}^2/\text{Vs}$ in the low-field region. With

$$\rho_{\text{ion}}(r) = \frac{N_c G Q_{\text{prim}}}{2\pi r \mu E(r)},$$

one finds the electric field

$$E(r) = \sqrt{c_1} \frac{k}{r} \sqrt{1 + \frac{r^2}{k^2}}, \quad (3.2)$$

with parameters $c_1 = \frac{N_c G Q_{\text{prim}}}{2\pi \epsilon_0 \mu}$ and k , as the solution of Maxwell's first equation in cylindrical coordinates and for cylindrical symmetry

$$(\text{div } \vec{E})(r) = \frac{1}{r} E(r) + \left(\frac{\partial E}{\partial r} \right)(r) = \frac{1}{\epsilon_0} [\rho_{\text{wire}} \delta(r) + \rho_{\text{ion}}(r)].$$

From the boundary condition that the potential difference between the anode wire and the tube wall equals the operating voltage V_0 , one obtains the transcendental equation in k ,

$$k \ln \frac{r_{\text{max}} \left(k^2 + k \sqrt{k^2 + r_{\text{min}}^2} \right)}{r_{\text{min}} \left(k^2 + k \sqrt{k^2 + r_{\text{max}}^2} \right)} + \sqrt{k^2 + r_{\text{max}}^2} - \sqrt{k^2 + r_{\text{min}}^2} = V_0 \sqrt{\frac{2\pi \mu \epsilon_0}{N_c G Q_{\text{prim}}}}, \quad (3.3)$$

which can be solved numerically. By inserting equation (3.2) into equation (3.1), the dependence of the gas amplification on the irradiation rate N_c is obtained. As the lower gas amplification affects the amount of space charge, the procedure has to be iterated. Convergence is typically reached after only few iterations.

A first order approximation can be obtained with $r \ll k$ and $k \gg r_{\max}$ in equations (3.2) and (3.3), which gives

$$E(r) = \sqrt{c_1} \frac{k}{r} \quad \text{and} \quad k \ln \frac{r_{\max}}{r_{\min}}.$$

Solving for k gives the electric field

$$E(r) = \frac{V_0}{r \ln \frac{r_{\max}}{r_{\min}}} \left(1 - \frac{r_{\max}^2 N_c G Q_{\text{prim}} \ln \frac{r_{\max}}{r_{\min}}}{8\pi\epsilon_0 \mu V_0^2} \right) + \frac{N_c G Q \ln \frac{r_{\max}}{r_{\min}}}{4\pi\epsilon_0 \mu V_0} \cdot r.$$

Assuming r -independent space charge ρ_{ion} one obtains

$$E(r) = \frac{V - \delta V}{r \ln \frac{r_{\max}}{r_{\min}}} + \frac{\rho_{\text{ion}} \cdot r}{2\epsilon_0},$$

where

$$\delta V = \frac{r_{\max}^2 N_c G Q_{\text{prim}} \ln \frac{r_{\max}}{r_{\min}}}{8\pi\epsilon_0 \mu V_0}$$

gives the effective voltage drop the gain drop causes which, as a function of the flux $N = \frac{N_c}{2r_{\max}}$, is given by

$$\delta V = \frac{r_{\max}^3 N G Q_{\text{prim}} \ln \frac{r_{\max}}{r_{\min}}}{4\pi\epsilon_0 \mu V_0} \propto r_{\max}^3.$$

For photons converting mainly in the tube walls, $Q_{\text{prim}} = \text{const.}$, i.e. a reduction of the tube radius r_{\max} by a factor of 2 makes the drift tubes 8 times less sensitive to gain drop. For penetrating particles like high energy hadrons, $Q_{\text{prim}} \propto r_{\max}$ and, therefore, $\delta V \propto r_{\max}^4$.

Figure 3.5 shows the calculated gas amplification G normalised to the nominal value G_0 in the absence of space charge as a function of the photon background flux registered by the MDTs ($r_{\max} = 14.6$ mm) and sMDTs ($r_{\max} = 7.1$ mm). The flux where the gas amplification drops below 80 % of the nominal value is approximately 1 kHz/cm² for MDTs and 10 kHz/cm² for sMDTs. Here, the primary ionisation charge $Q_{\text{prim}}^\gamma = 1300 e$ per photon hit measured for MDTs is also used for the sMDTs as a conservative estimate. Photons convert mainly in the tube walls where the density is much higher than in the gas. The average range of the emerging Compton-electrons in the gas volume is comparable to the tube diameter, hence the dependence of Q_{prim}^γ on the tube diameter is weak. Indirect measurements for sMDTs (see chapter 8) suggest a lower value of $Q_{\text{prim}}^\gamma \approx 900 e$ in this case, which implies an even better rate capability, indicated in Figure 3.5 by a dashed line.

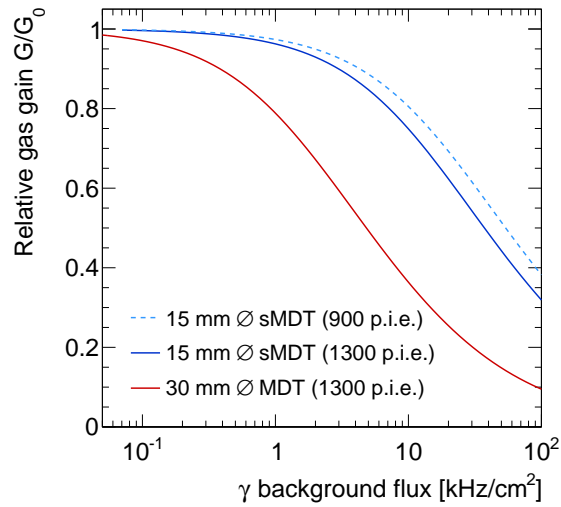


Figure 3.5: Relative gas amplification in MDT and sMDT tubes at nominal operating conditions as a function of the photon background flux detected by the drift tubes for $Q_{\text{prim}} = 900 e$ and $1300 e$.

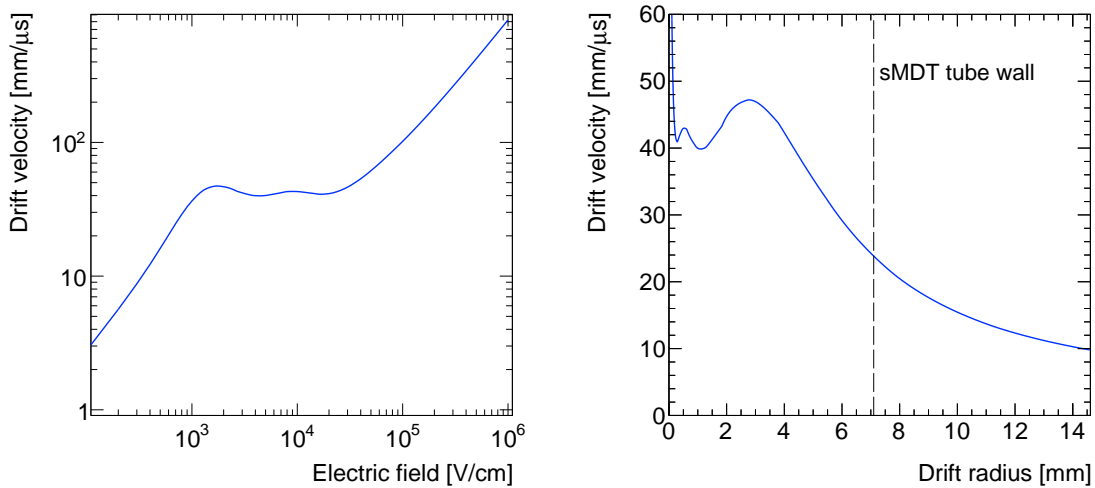


Figure 3.6: Drift velocity in Ar/CO₂ (93/7) at 3 bar absolute pressure as a function of the electric field strength (left) and of the drift radius (right) in Ar/CO₂ (93/7) at 3 bar absolute pressure calculated with the Magboltz program [57].

3.3.2 Space Charge Fluctuations

Ar/CO₂ (93/7) is a non-linear drift gas, i.e. the drift velocity depends strongly on the electric field and, therefore, on the drift radius (cf. Figure 3.6). Consequently, the space-to-drift-time relationship $r(t)$ is non-linear. The space charge in the drift tubes fluctuates in time. The number of background hits contributing to the space charge in a time interval follows a Poisson distribution. For a background rate of 500 Hz/cm in an MDT tube and an ion drift time to the tube wall of 3 ms, the number of hits per centimetre is $4.5^{+3.3}_{-2.0}$ with large variations.

The fluctuations of the space charge and, therefore, of the electric field and of the drift velocity cause the degradation of the spatial resolution for $r \gtrsim 5$ mm (cf. Figure 3.4). For sMDT tubes with $r_{\max} = 7.1$ mm, the effect of space charge fluctuations is essentially eliminated.

3.4 Read-Out Electronics Effects

3.4.1 Signal Characteristics

The moving ionisation charge multiplied in the avalanche close to the wire induces a current on the anode wire which is registered by the front-end electronics which measures the arrival time and ionisation charge of the hit.

In a cylindrical drift tube with inner tube diameter r_{\max} and wire diameter r_{\min} , where the wire is at a negative potential $-V_0$ with respect to the tube wall, the electric field is given by

$$E(r) = \frac{V_0}{r \ln \frac{r_{\max}}{r_{\min}}}.$$

As first approximation, the avalanche is considered to occur only on the wire surface, i.e. the electrons arrive promptly at the wire while the ions start drifting outwards at $r = r_{\min}$. The dependence of the ion velocity on the electrical field strength, $v_{\text{ion}} = \mu E$, leads to the differential equation

$$v_{\text{ion}}(r) = \frac{dr(t)}{dt} = \mu \frac{V_0}{r \ln \frac{r_{\max}}{r_{\min}}}$$

with the solution for the ion trajectory

$$r(t) = r_{\min} \sqrt{1 + \frac{t}{t_0}}, \text{ with } t_0 = \frac{r_{\min}^2 \ln \frac{r_{\max}}{r_{\min}}}{2\mu V_0}.$$

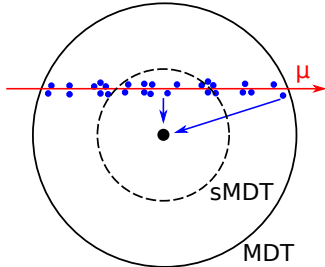


Figure 3.7: Cross section of an MDT tube with an incident muon track (red line) and ionisation clusters (blue circles). The dashed line indicates the boundary of an sMDT tube.

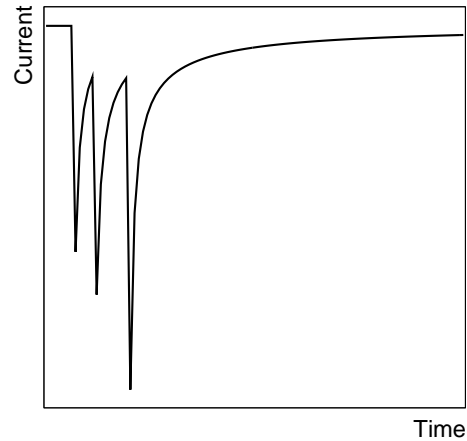


Figure 3.8: Illustration of the signal induced by three distinct ionisation clusters.

The current induced on the anode wire is according to Ramo's theorem [58]

$$I(t) = -eE_w v_{\text{ion}}(t) = -\frac{e}{2 \ln \frac{r_{\text{max}}}{r_{\text{min}}}} \frac{1}{t + t_0},$$

where $E_w = E/V_0$ is the weighting field, i.e. the electric field component in the direction of v_{ion} normalised to the anode wire potential. Hence, the signal of a single electron is negative and drops hyperbolically with a time constant t_0 that is on the order of few nanoseconds. The overall signal generated by a charged particle hit is the sum of the currents induced by all ion and electron ionisation clusters multiplied in the avalanche. Such a signal from just three clusters is illustrated in Figure 3.8.

Figure 3.9 shows more realistic muon signals simulated with the Garfield program [59] for both MDT and sMDT drift tubes. Due to the shorter ionisation path in sMDT tubes illustrated in Figure 3.7, the overall signal length as well as the total amount of charge are smaller than for the MDT tubes, which are significant advantages in terms of space charge and dead time.

In Figures 3.8 and 3.9, long signal tails due to the slow ion drift to the tube wall are visible causing a shift of the baseline for subsequent signals increasing with the rate. Several methods are available for cancellation of this tail (see Figure 3.10). Bipolar shaping provides baseline stability up to the highest rates with the drawback of causing an undershoot of equal area as the positive signal pulse which distorts subsequent pulses. The alternative unipolar signal shaping using pole-zero filters to cancel the tail avoids the undershoot but is subject to baseline shift depending on the rate since the long ion tail depends on the ion mobility and, therefore, on

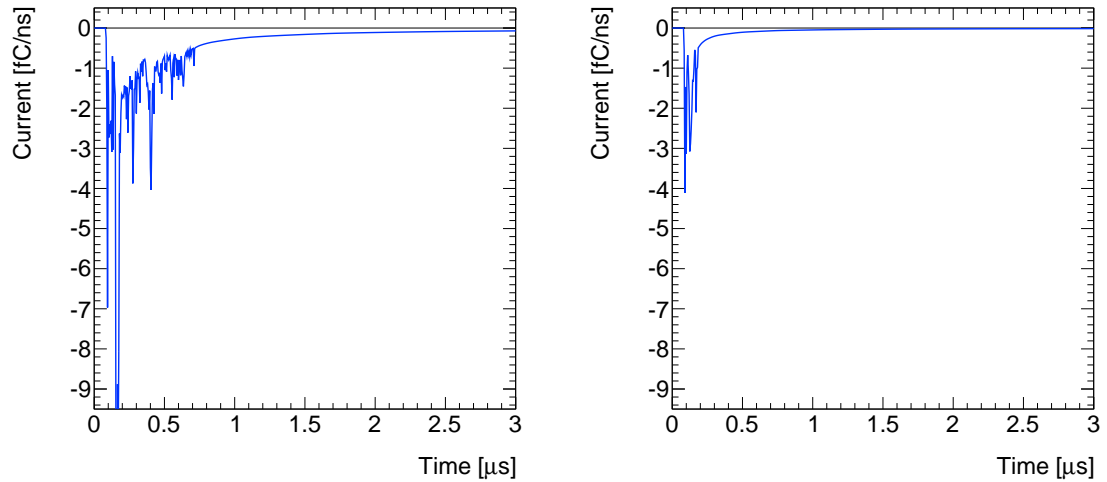


Figure 3.9: Typical signals induced by muon tracks with impact radius $r = 4$ mm in MDT (left) and sMDT (right) drift tubes as simulated with the Garfield program [59].

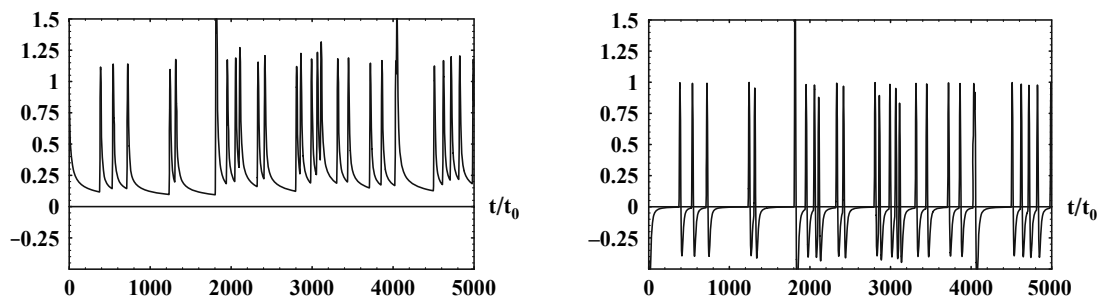


Figure 3.10: A fast random sequence of signals (with inverted polarity) processed by (left) unipolar shaping and (right) bipolar shaping [55]. With unipolar shaping, there is a baseline shift increasing with the signal rate.

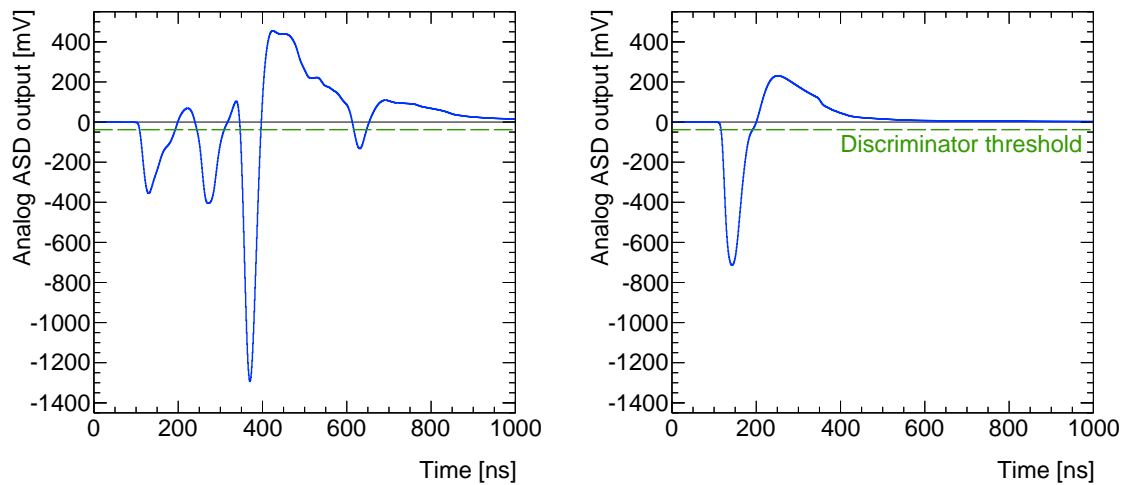


Figure 3.11: Typical simulated signals created by muon tracks with drift radius $r = 4$ mm in MDT (left) and sMDT (right) drift tubes.

the exact environmental conditions which makes it very hard to tune the time constants of the pole-zero filters. For the MDT chambers bipolar shaping was chosen because of the baseline stability at high rates.

Figure 3.11 shows the same simulated signals as in Figure 3.9 convoluted with the full analogue response function of the ASD read-out chip* (cf. Figure 2.9) which corresponds to the signal fed to the discriminator. With this shaping scheme, each hit can result in several discriminator threshold crossings as illustrated in Figure 3.11, in particular for the MDT tubes.

Only the first threshold crossing time for each hit is of interest for the drift time measurement, while the following ones increase the effective dead time and the required read-out bandwidth. In order to suppress secondary discriminator threshold crossings, adjustable additional dead time is implemented in the ASD chip (cf. section 2.2.2). The nominal ATLAS setting for the dead time is approximately 820 ns (cf. Table 2.3), compound of the average pulse width (carrying the charge measurement) of about 200 ns and the additional programmable dead time of around 620 ns at maximum.

3.4.2 Dead Time Effects

The electronics dead time does not only prevent secondary threshold crossings for the same hit, it also reduces the efficiency for good muon hits which are masked by preceding background hits.

*Parasitic capacitances, like the one of the tube, that slightly modify the shaping are neglected.

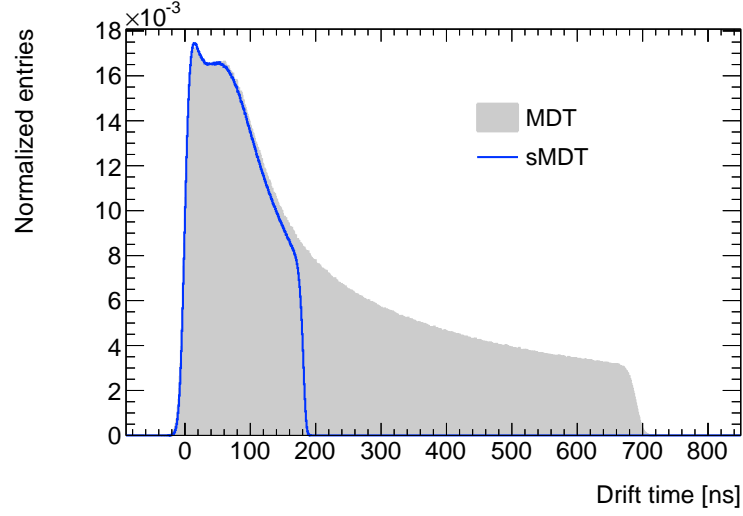


Figure 3.12: Comparison of the drift time spectra of MDT (30 mm diameter) and sMDT (15 mm diameter) drift tubes.

The muon efficiency depends linearly on the observed counting rate n and on the dead time t_{dead} :

$$\varepsilon(n) = \varepsilon_0 - n \cdot t_{\text{dead}}.$$

The observed counting rate n depends likewise on the dead time. As long as the average time over threshold is shorter than the dead time, the behaviour is *non-paralysing*, i.e. the effective dead time is not extended by subsequent threshold crossings. The real hit rate N in the non-paralysing case is [60]:

$$N = \frac{n}{1 - n \cdot t_{\text{dead}}}.$$

The dependence of the efficiency on the real counting rate is therefore

$$\varepsilon(N) = \frac{\varepsilon_0}{1 + N \cdot t_{\text{dead}}}. \quad (3.4)$$

For secondary threshold crossings which are correlated in time with the primary threshold crossing, this has to be modified to

$$\varepsilon(N) = \frac{\varepsilon_0}{1 + N \cdot m_{\text{hit}} \cdot t_{\text{dead}}}, \quad (3.5)$$

where m_{hit} is the average number of threshold crossings per hit in the tube. To obtain high efficiency, the dead time should be as short as possible while minimising secondary threshold crossings.

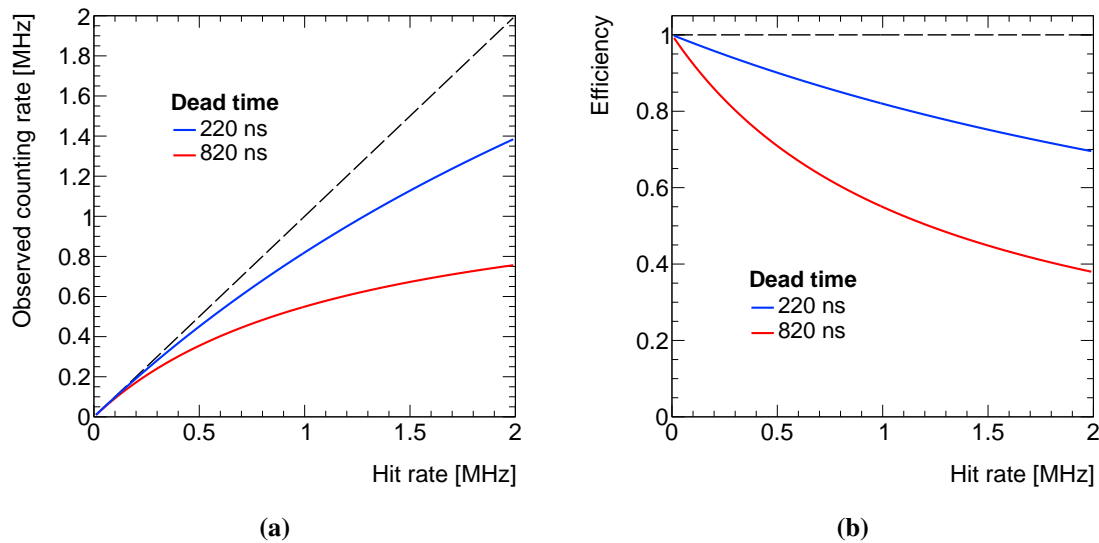


Figure 3.13: Calculated dependence of (a) the observed counting rate and (b) the muon efficiency on the real hit rate for minimum and maximum dead time setting of the ASD chip (δ -electron effects are not taken into account).

The baseline operation mode of the ATLAS MDT chambers is with the maximum dead time of 820 ns which slightly exceeds the maximum drift time and thus leads to a threshold crossing multiplicity very close to unity. For the sMDT chambers, the minimum adjustable dead time of 220 ns can be used without increase in the threshold crossing number, because the maximum drift time is just 185 ns (see Figure 3.12 and section 4.3.1). This yields a major improvement in the efficiency as can be seen in Figure 3.13b.

3.4.3 Signal Pile-Up Effects

A disadvantage of the bipolar shaping scheme is the large and long undershoot of equal area as the associated positive signal pulse. Signal pulses from muons succeeding a background pulse after a short enough time interval are superimposed on top of the undershoot effectively shifting the baseline for the successive pulses and consequently the discriminator threshold crossing time as illustrated in Figure 3.14.

We call this effect signal pile-up. It causes additional efficiency loss and degrades the resolution of the secondary hits as can be seen in the measurements presented in chapter 6. In chapter 8, simulation results are shown for modified signal shaping using active baseline restoration, which cures the signal pile-up problem.

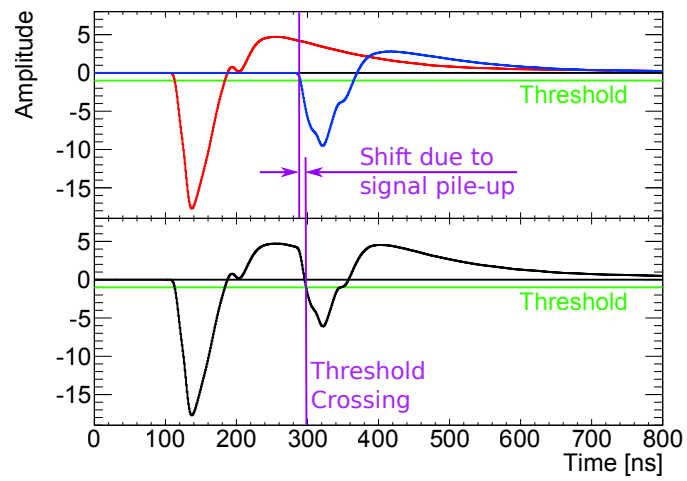


Figure 3.14: Illustration of the signal pile-up effects due to the undershoot (here overshoot for inverted polarity) caused by bipolar shaping. Top: two independent successive pulses, bottom: superposition of the two pulses.

4

Calibration and Data Analysis Methods

In this chapter calibration and data analysis methods of drift tube detectors are discussed.

4.1 Background Rate Measurement

The background rate can be measured with the drift tubes themselves using the side bands of the muon drift time spectra. The observed background counting rate is given by

$$n = \frac{\text{number of counts in side band}}{\text{time interval of side band} \times \text{number of muon triggers}}. \quad (4.1)$$

For high counting rates, when the average time between two hits approaches the electronics dead time t_{dead} , the observed counting rate needs to be corrected for the masking of background hits due to the dead time in order to obtain the real rate of ionising interactions in the tube. If not otherwise stated, the correction is always applied in the following. The real counting rate, corrected for the dead time effect, is given by

$$N = \frac{n}{1 - n \cdot t_{\text{dead}}} \quad (4.2)$$

as discussed in section 3.4.2.

Another possibility to measure the real hit rate is via the produced ionisation charge or the current drawn by a drift tube from the high-voltage power supply which is given by

$$I = I_{\text{dark}} + Q \cdot G \cdot N \quad (4.3)$$

with the average ionisation charge Q per particle crossing, the gas amplification G , the hit rate N in the drift tube connected to the corresponding high voltage channel and the dark current I_{dark} . If Q is known, the hit rate can be directly determined from the current as long as it is low enough for space charge effects on the gas gain to be negligible. For higher rates, the space charge induced gain drop needs to be taken into account, for instance by means of the prediction by Diethorn's equation described in section 3.3.1. The dark current in MDT and sMDT chambers is around 0.1 nA per tube (see section 6.3.3) and can often be neglected.

4.2 Gas Amplification Measurement

Two methods are used to measure the gas gain drop due to space charge. If the hit rate is known, e.g. from equations (4.1) and (4.2), then equation (4.3) can be used to measure the gas amplification:

$$G = \frac{I - I_{\text{dark}}}{Q \cdot N}. \quad (4.4)$$

The second method compares the average rising edge charge q and q_0 measured by the Wilkinson ADC of the ASD chip (see section 2.2.2) with and without irradiation, respectively. Muon and background hits generate different amounts of ionisation charge. In order to avoid bias, only charge measurements for muons are used. Muon hits are selected requiring that the measured drift radii match a reconstructed reference track within three times the drift tube spatial resolution ($3\sigma(r)$). The resulting charge distributions are fitted with a Landau distribution. As the charge also depends on the drift radius r (cf. Figure 4.2), only hits in the range $4 \text{ mm} \leq r < 5 \text{ mm}$ at the maximum of the charge vs. drift radius function are used for sMDT tubes. The most probable value (MPV) of the fitted Landau distribution give q and q_0 .

4.3 Drift Tube Calibration Methods

4.3.1 Drift Time Measurement

Accurate drift radius measurement requires high drift time resolution. The time t_{TDC} measured by the TDC chip comprises several contributions besides the electron drift time t_{drift} :

$$t_{\text{TDC}} = t_{\text{drift}} + t'_0 - t_0^{\text{trigger}} + t_{\text{prop}} =: t_{\text{drift}} + t_0.$$

The individual contributions are:

Channel offset t'_0 : The signal path lengths vary between different drift tube channels. The resulting time offsets of typically a few nanoseconds are determined by fitting the rising edge of the drift time spectrum of each tube.

Trigger time offset t_0^{trigger} : The trigger signal is usually derived from the coincidence of several trigger detectors with different signal path lengths. The corresponding time offset t_0^{trigger} can be determined by fitting the rising edge of a drift time spectrum containing only events triggered by the particular trigger detector.

Signal propagation time t_{prop} : The length of the drift tubes in ATLAS is about 1 to 6 m. The signal propagation time along the tube needs to be taken into account to limit additional time jitter to less than 1 ns. This is not necessary for beam test measurements where the illuminated detector area is small, but for the measurements with cosmic ray muons which use the full chamber area.

To determine $t_0 = t'_0 - t_0^{\text{trigger}} + t_{\text{prop}}$, a fitting procedure that has been developed for the drift time spectra of both MDT and sMDT chambers, as there is no significant difference in the shapes of the rising and falling edges of their drift time spectra. The rising edge is fitted with a modified Fermi function

$$G(t) := p_0 + \frac{A_0}{1 + e^{-\frac{t-t_0}{T_0}}} \quad (4.5)$$

in an optimised range. The parameter p_0 accounts for flat background caused by uncorrelated noise or background radiation. A_0 is the amplitude of the Fermi function and T_0 is the time where $A_0/2$ is reached describing the steepness of the edge. The detailed algorithm is described in [61].

Similarly, the maximum drift time t_{max} is determined from a fit of the falling edge of the drift time spectrum with the function

$$H(t) := p_{\text{max}} + \frac{\alpha_{\text{max}}t + A_{\text{max}}}{1 + e^{\frac{t-t_{\text{max}}}{T_{\text{max}}}}}, \quad (4.6)$$

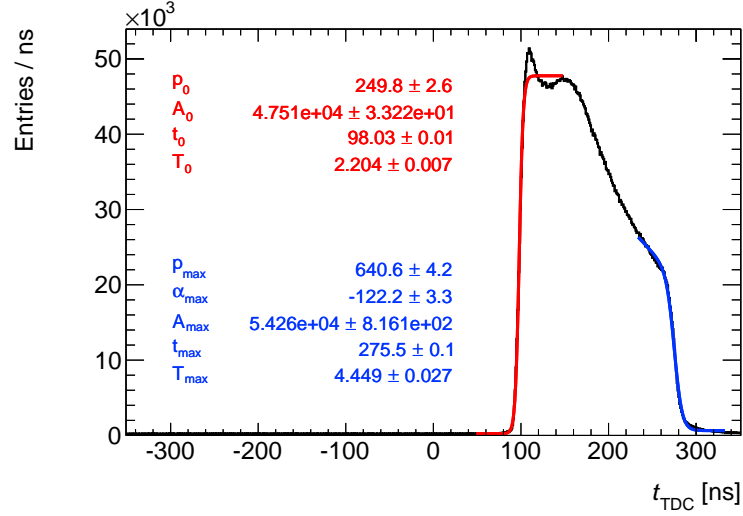


Figure 4.1: Drift time spectrum of a uniformly illuminated sMDT chamber fitted with equation (4.5) at the rising edge (red) and equation (4.6) at the falling edge (blue) for the determination of the minimum and maximum drift times, respectively.

where the slowly falling region $t < t_{\max}$ is modelled by a straight line with intercept A_{\max} and slope α_{\max} . It should be noted, that the slope of the falling edge is significantly smaller than the slope of the rising edge. This is caused by the efficiency loss close to the tube wall (cf. Figure 2.14) which leads to less entries at the end of the drift time spectrum. For the MDTs, the convention

$$t'_{\max} = t_{\max} + 2 \cdot T_{\max}$$

is used to account for the effect of the efficiency loss on the maximum drift time. Figure 4.1 shows a typical drift time spectrum of a uniformly illuminated sMDT chamber fitted with equations (4.5) and (4.6). The maximum drift time is not needed for the further calibration steps, but it is a good indicator of the correct gas mixture and pressure. The values obtained for the sMDTs after t_0 subtraction are $t_{\max} = (177.5 \pm 0.1)$ ns and $t'_{\max} = (186.4 \pm 0.1)$ ns.

4.3.2 Calibration of the Space-to-Drift Time Relationship

An accurate space-to-drift-time relationship $r(t)$ is obtained with the analytic autocalibration method described in [25, 26, 62]. The method is based on the redundant measurement of muon tracks in multiple drift tube layers. Starting from an initial, less accurate $r(t)$ relationship obtained e.g. by the integration of the drift time spectrum as described in [63], the analytic autocalibration estimates the deviation between the initial and the true $r(t)$ relationship based on the track residuals to obtain a correction function applied to the initial $r(t)$ relationship. For

further improvement, the procedure is repeated and converges typically after five to ten iterations. As shown in [62], the method provides space-to-drift-time relationships with an accuracy of better than $20\ \mu\text{m}$.

4.3.3 Time Slewing Correction

The use of a fixed discriminator threshold for the drift time measurement introduces a dependence of the threshold crossing time on the pulse amplitude, so-called time slewing. The charge measurement by the Wilkinson ADC implemented in the front-end electronics (ASD chip) and operated with a short gate (the nominal ATLAS setting is $18.5\ \text{ns}$; see Table 2.3) allows for partial recovery of the resolution degradation caused by the time slewing by applying a linear correction

$$t_{\text{corr}} = t - c(r) \cdot [Q - Q_{\text{peak}}(t)]$$

to the measured drift time t as explained in [64], where $c(r)$ is a drift radius dependent correction factor and $Q - Q_{\text{peak}}(t) =: \Delta Q$ the deviation of the measured charge in ADC counts from the peak of the charge distribution as a function of r (see Figure 4.2). $Q_{\text{peak}}(t)$ is determined from a fit of the sum of a Gaussian and a Landau distribution with equal mean/MPV in the range from 60 to 160 ADC counts.

To obtain $c(r)$, the deviation

$$\Delta t = t - t(r_{\text{track}})$$

of the measured drift time t from the expected drift time $t(r_{\text{track}})$, the time slewing, is evaluated, where r_{track} is the distance between the (externally measured) muon track and the anode wire and $t(r)$ is the inverse of the space-to-drift-time relationship $r(t)$. The correction function $c(r)$ is determined from a linear fit to the distribution $\Delta t(\Delta Q)$.

Figure 4.3 shows an example of the distribution in one impact radius bin superimposed with the mean values of Δt in each bin of ΔQ and a linear fit to the mean values. The slopes $\delta\Delta t/\delta\Delta Q$ of the fitted lines in all impact radius bins are depicted in Figure 4.4. The correction function $c(r)$ is, finally, a parabola fitted to the slopes in each bin. Tests showed that a second order polynomial fit yields good results while higher order parametrisations do not lead to an improvement.

4.4 Spatial Resolution

The single-tube spatial resolution is the fundamental ingredient for the drift tube detector and track segment resolution. It is also needed for the determination of the muon detection efficiency using reference tracks reconstructed in the chamber. Thus, the first step is the measurement of the

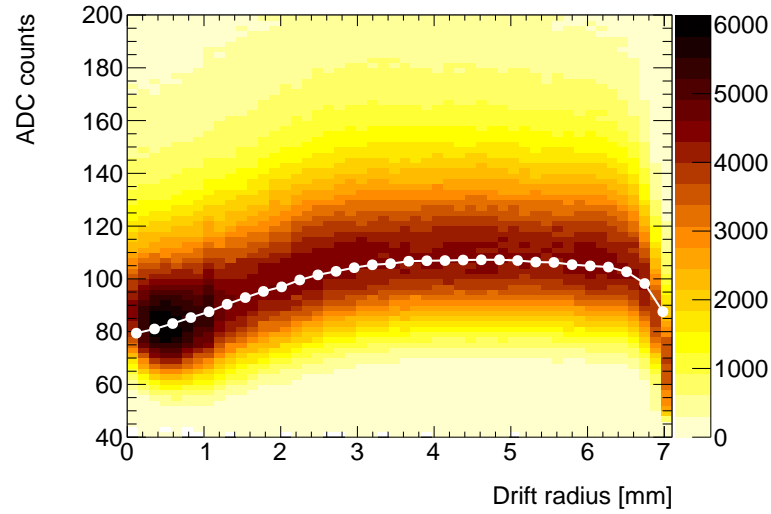


Figure 4.2: Rising edge charge in ADC counts as a function of the drift radius. The white dots indicate the peak of the charge distribution in bins of the drift radius (see text). The dependence on the drift radius reflects the arrival time distribution of the ionisation clusters at the anode wire. With increasing drift radius ionisation clusters arrive in shorter time intervals for geometrical reasons, increasing the rising edge charge measured by the ADC. Near the tube wall, the number of ionisation clusters decreases rapidly and the rising edge charge drops.

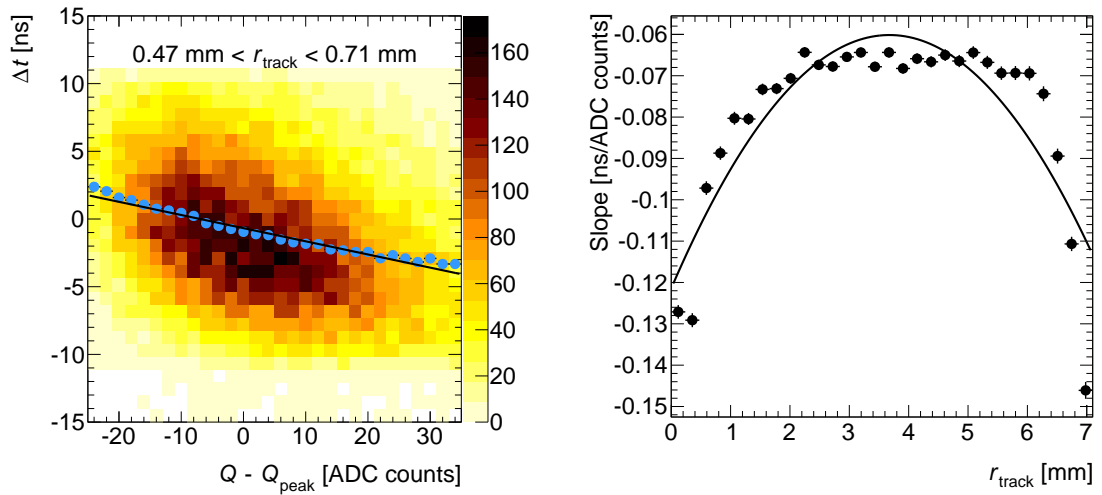


Figure 4.3: Dependence of the time slewing Δt on the deviation ΔQ of the measured ADC counts from the peak in the bin $0.47 \text{ mm} < r_{\text{track}} < 0.71 \text{ mm}$.

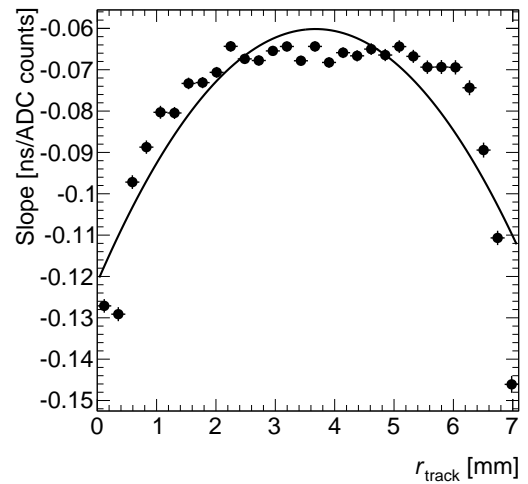


Figure 4.4: Dependence of the time slewing correction factor on the drift radius. The markers show the obtained values in slices of the impact parameter, the solid line indicates the fit of a quadratic curve.

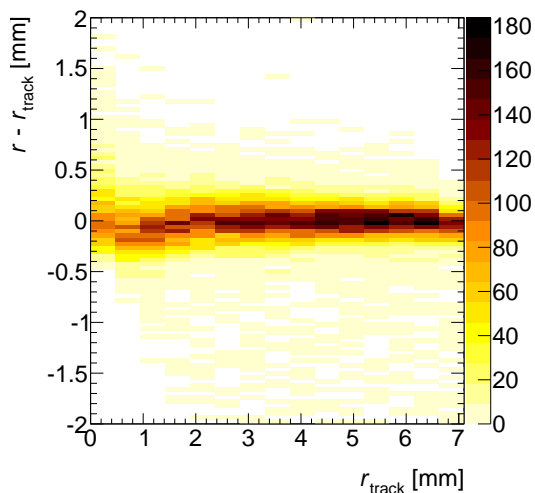


Figure 4.5: Distribution of the track residuals $r - r_{\text{track}}$ as a function of r_{track} for an sMDT tube.

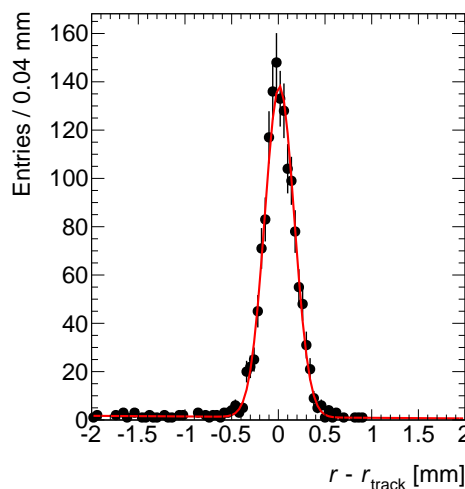


Figure 4.6: Projection of the bin $3.31 \text{ mm} < r_{\text{track}} < 3.79 \text{ mm}$ of the residual distribution fitted with equation (4.7).

spatial resolution as a function of the drift radius of the drift tubes used for track reconstruction. An iterative method [65] relying only on muon hits recorded in the same chamber is used.

Starting from an approximate resolution function taken from simulation or from previous measurements, muon tracks are reconstructed without the tube under study and the measured drift radii r in this tube compared to the distance r_{track} of closest approach of the extrapolated track to the drift tube centre in the (y, z) -plane perpendicular to the wire. The variance of the distribution of the track residuals $\delta := r - r_{\text{track}}$ is the quadratic sum of the drift tube spatial resolution $\sigma_{\text{tube}}(r)$ and the uncertainty $\sigma_{\text{track}}(y_{\text{track}}, z_{\text{track}})$ in the track extrapolation to the tube:

$$\text{Var}(\delta) = \sigma_{\text{tube}}^2(r) + \sigma_{\text{track}}^2(y_{\text{track}}, z_{\text{track}}).$$

Figure 4.5 shows a typical residual distribution for hits in an sMDT tube excluded from the track fit. The residuals are distributed symmetrically around zero in the intermediate impact radius range, whereas at small and large radii boundary effects can be seen: drift times with $t < 0$ and $t > t_{\text{max}}$ are interpreted as drift radii $r = 0$ and $r = r_{\text{max}}$, respectively. Thus, there are no entries with

$$\delta < -r_{\text{track}} \quad \text{and} \quad \delta > r_{\text{max}} - r_{\text{track}}$$

rendering the residual distribution asymmetrically in these ranges. To determine the spatial

resolution, a Gaussian function with constant offset N_b accounting for background and noise hits

$$f(\delta) := N \cdot e^{-\frac{1}{2} \left[\frac{\delta - \mu}{\sigma_{\text{residual}}} \right]^2} + N_b, \quad (4.7)$$

is fitted to the residual distribution in each bin of the impact radius r_{track} (see Figure 4.6).

In the following, the width σ_{residual} of the fitted Gaussian is used instead of the variance $\text{Var}(\delta)$ which is very sensitive to outliers, i.e. uncorrelated background or noise hits.

The uncertainty in a point (y, z) on a track fitted to N measured drift radii is determined according to the method described in [65]:

$$\sigma_{\text{track}}(y, z) = \frac{1}{D} \left[\Lambda_{22} - 2z\Lambda_{12} + z^2\Lambda_{11} \right] \quad (4.8)$$

with

$$(\Lambda_{11}, \Lambda_{12}, \Lambda_{22}) = \sum_{j=0}^N \frac{(1, z_j, z_j^2)}{\sigma_{j, \text{tube}}^2}$$

and

$$D = \Lambda_{11}\Lambda_{22} - \Lambda_{12}^2.$$

For each measured residual, the corresponding σ_{track} is calculated. The drift tube spatial resolution in the i^{th} drift radius bin is then

$$\sigma_{\text{tube}}(r_i) = \sqrt{\sigma_{\text{residual}}(r_i)^2 - \langle \sigma(r_i)_{\text{track}} \rangle^2} \quad (4.9)$$

with the mean track error $\langle \sigma(r_i)_{\text{track}} \rangle$ in the bin under the assumption of a constant number of hits entering the track fit.

The obtained single-tube resolution $\sigma_{\text{tube}}(r)$ is used in the tracks fits of further iterations. This method converges quickly, typically after less than five iterations, and is insensitive to the initial resolution function which can even be constant.

Once the spatial resolution of the drift tubes used for reference track reconstruction is known, a final iteration is performed using a track fit to all drift tubes. The average spatial resolution of a drift tube finally is given by

$$\bar{\sigma} = \sqrt{\frac{1}{r_{\text{max}}} \int_0^{r_{\text{max}}} \sigma_{\text{tube}}^2(r) dr}. \quad (4.10)$$

4.5 Drift Tube Efficiency

The definition of the drift tube detection efficiency

$$\varepsilon_{\text{det}} = \frac{n_{\text{det}}}{n_{\text{exp}}}, \quad (4.11)$$

with the numbers of detected and expected hits, n_{det} and n_{exp} , respectively, has the disadvantage that fake hits caused by δ -electrons, secondary discriminator threshold crossings, noise hits, and background radiation hits also contribute.

Hence, to define a real muon detection efficiency relevant for muon track reconstruction in (s)MDT chambers, the so-called 3σ -efficiency is used, defined as the probability to measure a drift radius deviating by less than three times the drift tube spatial resolution (see previous section) from the expected value from reference track extrapolation. With a spatial drift tube resolution of roughly $100\ \mu\text{m}$, corresponding to a time resolution of $\sim 3\ \text{ns}$ (the drift velocity is in the range 10 to $50\ \mu\text{m}/\text{ns}$; cf. Figure 3.6), the fake contribution for the 3σ -efficiency is less than 1% for background rates up to $1\ \text{MHz}$.

5

MDT Chambers Under Photon Irradiation

5.1 Introduction

An extensive test beam programme has been carried out with the MDT chambers prior to their operation in ATLAS, where the performance in the presence of background radiation and its dependence on ambient conditions like temperature and magnetic field strength have been studied in detail [33, 35, 36]. These measurements provided input for the ATLAS detector simulation affecting the muon reconstruction efficiency and momentum resolution. The main focus was on the operating parameters to be used in ATLAS.

New interest in the high-rate performance of the MDT chambers arose with the planned upgrade of the LHC to the HL-LHC (see section 1.4). A significant improvement of the efficiency of the MDT chambers at high counting rates can be achieved by reducing the adjustable dead time of the ASD front-end chip. The maximum dead time of approximately 820 ns (cf. Table 2.3) slightly exceeds the maximum drift time of the MDT tubes and was chosen for ATLAS operation in order to prevent multiple discriminator threshold crossings for a particle hit, which complicate the track finding and increase the required read-out bandwidth. These criteria are, however, not critical and can be overcome by using novel track finding approaches such as the one proposed in [66]. Another effect to be taken into account with a shorter dead time is signal pile-up,

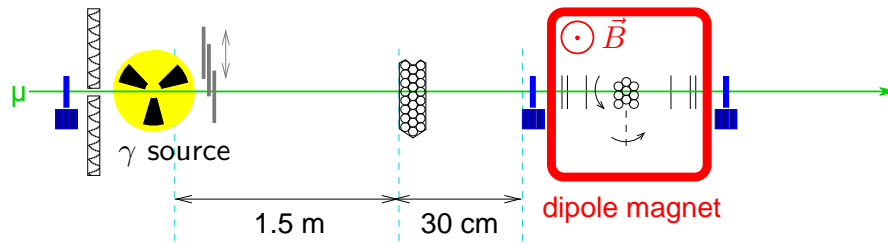


Figure 5.1: Sketch of the experimental setup used in 2004 [35] at the CERN Gamma Irradiation Facility in the X5 muon beam. A bundle of 15 cm long drift tubes was mounted on a rotation table in the middle of the beam hodoscope inside a large dipole magnet. A bundle of 377 cm long drift tubes was installed in front of the photon source outside of the magnet for high-rate studies. Scintillation counters upstream of the source and before and after the beam hodoscope are used as muon beam trigger.

described in section 3.4.3, which causes a deterioration of the spatial resolution and efficiency.

In this chapter, new measurements of the MDT spatial resolution using data recorded in 2004 [35] at the CERN Gamma Irradiation Facility (GIF) in a 90 GeV muon beam for the minimum ASD dead time setting of 220 ns are presented. These measurements complement the previous ones with respect to signal pile-up effects.

5.2 Experimental Setup

Two MDT drift tube bundles were used in the test setup shown in Figure 5.1. A small one with 15 cm long tubes was mounted on a rotation table inside a large dipole magnet. A bigger one with 377 cm long tubes, the tube length of the MDT BOS chambers*, was installed in front of the photon source for high-rate studies. A beam hodoscope consisting of 2×3 silicon strip detectors with $5 \times 5 \text{ cm}^2$ active area was mounted downstream and upstream of the small bundle. Each of the four inner strip detectors measured the lateral positions of the incident muon tracks with $10 \mu\text{m}$ accuracy. The two outermost detector planes measured the vertical muon track positions with similar accuracy. One of the vertical detectors had to be turned off due to high leakage currents.

The background radiation was generated by the ^{137}Cs source of the GIF emitting 662 keV photons in 85 % of the decays. A filter system in front of the source renders the flux uniform in the vertical direction. The photon flux can be adjusted over a wide range by means of a set of movable filters. At the time of the measurements, the activity of the ^{137}Cs source was approximately 650 GBq.

*The chambers in the small sectors of the outer layer of the barrel region [67].

Data were recorded with operating parameters close to the nominal ATLAS settings listed in Tables 2.1 and 2.3. Differences were the slightly lower discriminator threshold of -34 mV instead of -38 mV and the variation of the programmable dead time. The lower discriminator threshold slightly improves the spatial resolution, but it also implies a higher noise rate and more afterpulsing caused by the imperfect ion tail cancellation of the ASD chip discussed below.

5.3 Measurements Under Photon Background Radiation

For the resolution and efficiency studies, hits in the long MDT bundle were analysed and compared with tracks of the 90 GeV muons reconstructed with the beam hodoscope and extrapolated to the MDT bundle. For both the maximum and minimum programmable dead times, data points were recorded at two different irradiation levels (attenuation factors 5 and 10 with respect to the maximum photon flux). In addition, a measurement with minimum dead time and attenuation factor 2 was performed.

5.3.1 Dead Time Measurement

The actual dead time of the ASD chip after a hit depends in ADC mode on the measured charge which is encoded in the digital output pulse length (cf. section 2.2.2). This intrinsic dead time is the lower limit of the adjustable dead time range, a programmable dead time between 17 ns and 600 ns is added to this intrinsic dead time. The measured counting rates and muon efficiencies depend on the total dead time, which is the minimum time interval $\Delta t = t_2 - t_1$ between two subsequent hits 1 and 2 in an event.

Figure 5.2 shows the distributions of Δt for minimum and maximum programmable dead time. For uncorrelated background hits, the time interval between two hits follows an exponential distribution

$$f(\Delta t) = \lambda \cdot e^{-\lambda \Delta t}$$

with the counting rate parameter λ . The measured Δt distributions differ from an exponential distribution due to the dead time which cuts off small values of Δt and the limited length of the read-out window of approximately $1.25 \mu\text{s}$ which defines the upper limit on the measurable Δt values. The dead time t_{dead} is measured by fitting a Fermi distribution

$$g(\Delta t) = N \cdot \frac{1}{1 + e^{-\frac{\Delta t - t_{\text{dead}}}{T_{\text{dead}}}}$$

in the range around the rising edge. Values of $t_{\text{dead}} = (222.0 \pm 0.4)$ ns and (823.1 ± 1.5) ns are obtained for minimum and maximum dead time setting, respectively. These values are used in the following for the dead time correction of the measured counting rates according to equation (4.2).

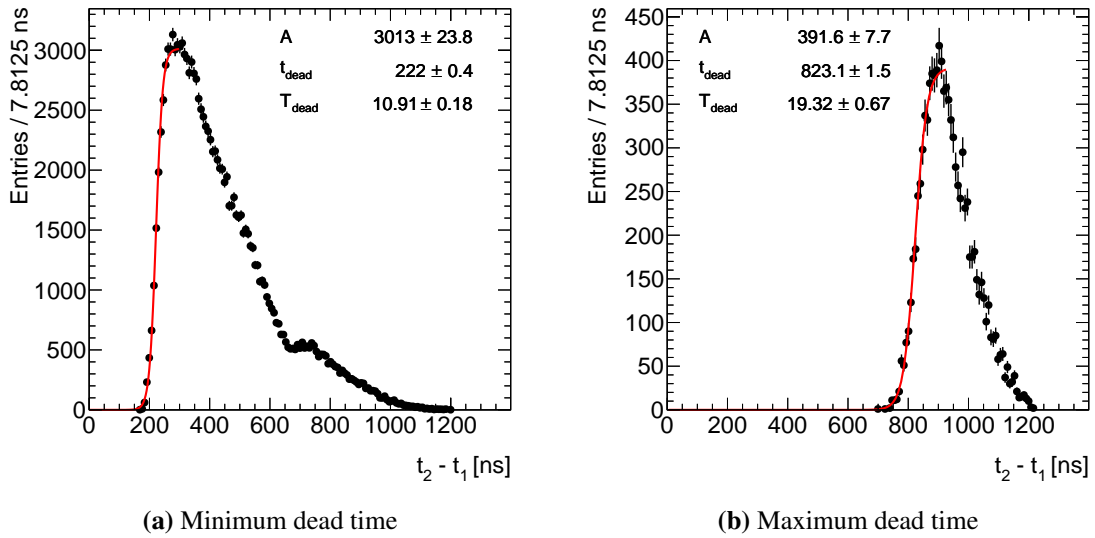


Figure 5.2: Distribution of the time difference $\Delta t = t_2 - t_1$ between first and second hit for (a) minimum and (b) maximum dead time setting. The bump at $\Delta t \approx 700$ ns in the left figure is due to the imperfect ion tail cancellation of the ASD chip.

5.3.2 Afterpulsing

The low discriminator threshold used in the test beam measurements slightly improves the spatial resolution, but also causes higher sensitivity to baseline fluctuations. A consequence besides the generally higher noise rate is the accumulation of hits with $\Delta t \approx 700$ ns in Figure 5.2a. These extra hits are due to the imperfect ion tail cancellation of the ASD chip. Figure 5.3 shows the measured analog ASD response to 100 ns long rectangular input pulses. The slight undershoot of the baseline with maximum around $\Delta t \approx 700$ ns causes an effectively lower threshold for hits in this range and, hence, an enhanced probability for noise hits above the discriminator threshold.

These noise spikes have small amplitudes and are very short usually resulting in small charge measurements of less than 40 ADC counts. As these small pulses cause neither space charge nor signal pile-up effects, they have to be eliminated for the measurement of the rate dependence of the spatial resolution by requiring more than 40 ADC counts. For the measurement of the dead time effect on the efficiency, on the other hand, the noise hits have to be taken into account in the counting rate measurement. The details of the different rate measurements are described in the following section.

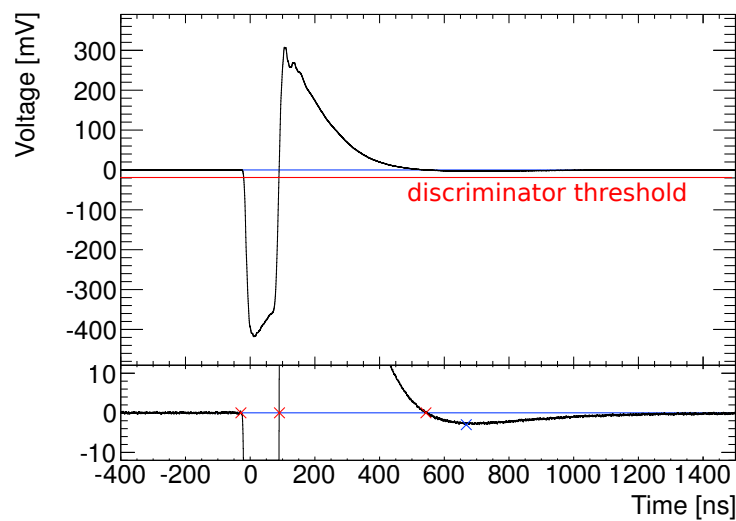


Figure 5.3: Measured analog response of the ASD chip to a 100 ns long rectangular input current pulse after the last shaping stage. On the enlarged scale (bottom), a secondary undershoot of the baseline at $t \approx 700$ ns is visible. The response shown is averaged over several hundred pulses to make the afterpulse visible, which is otherwise hidden in the noise. This “afterpulse” is correlated in time with the original pulse and is due to the imperfect ion tail cancellation of the ASD chip. It increases the probability for noise hits on top of it to cross the discriminator threshold around $t \approx 700$ ns after the first pulse.

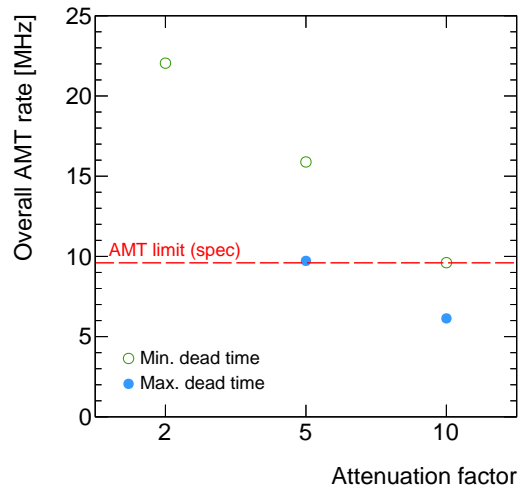


Figure 5.4: Total counting rate of all 24 drift tubes read out by one AMT chip for minimum and maximum dead time. The dashed line indicated the specified rate limit of the AMT [32].

5.3.3 Counting Rate Measurement

Both the background fluxes and the counting rates reached in the tests exceed by far the maximum rates expected in ATLAS. This is especially true for the latter which depend, for a given uniform flux, on the drift tube length. In general, the background flux in the ATLAS muon spectrometer increases with decreasing distance to the beam line, while the tube length decreases compensating partially for the higher flux in the counting rate and occupancy. In the GIF setup 2004, 377 cm long tubes as in the outermost MDT chambers of the barrel region were operated at photon fluxes exceeding the maximum expected values in the inner end-cap layer. Hence, the counting rates and occupancies are very high.

Figure 5.4 shows the total measured (i.e. not dead time corrected) counting rate of all 24 drift tubes that are read out by the AMT-3 chip on a mezzanine board versus the photon source attenuation factor. The AMT-3 user's manual [32] specifies a maximum rate of 9.6 MHz (400 kHz per channel) if all 24 channels are used, which is the case under photon irradiation even though only 4 out of the 24 drift tubes are in the active area of the beam trigger. The specified maximum rate is vastly exceeded with attenuation factors 2 and 5 and minimum dead time. For rates beyond the specification, the hit buffer of the AMT chip starts to overflow resulting in a loss of hits. Figure 5.5 shows drift time spectra with minimum dead time for attenuation factors 10, 5 and 2, and closed photon source. The effect of overflowing hit buffer can clearly be seen for the highest irradiation level in Figure 5.5d. These data with a total counting rate of over 20 MHz are, therefore, not usable for efficiency and resolution studies.

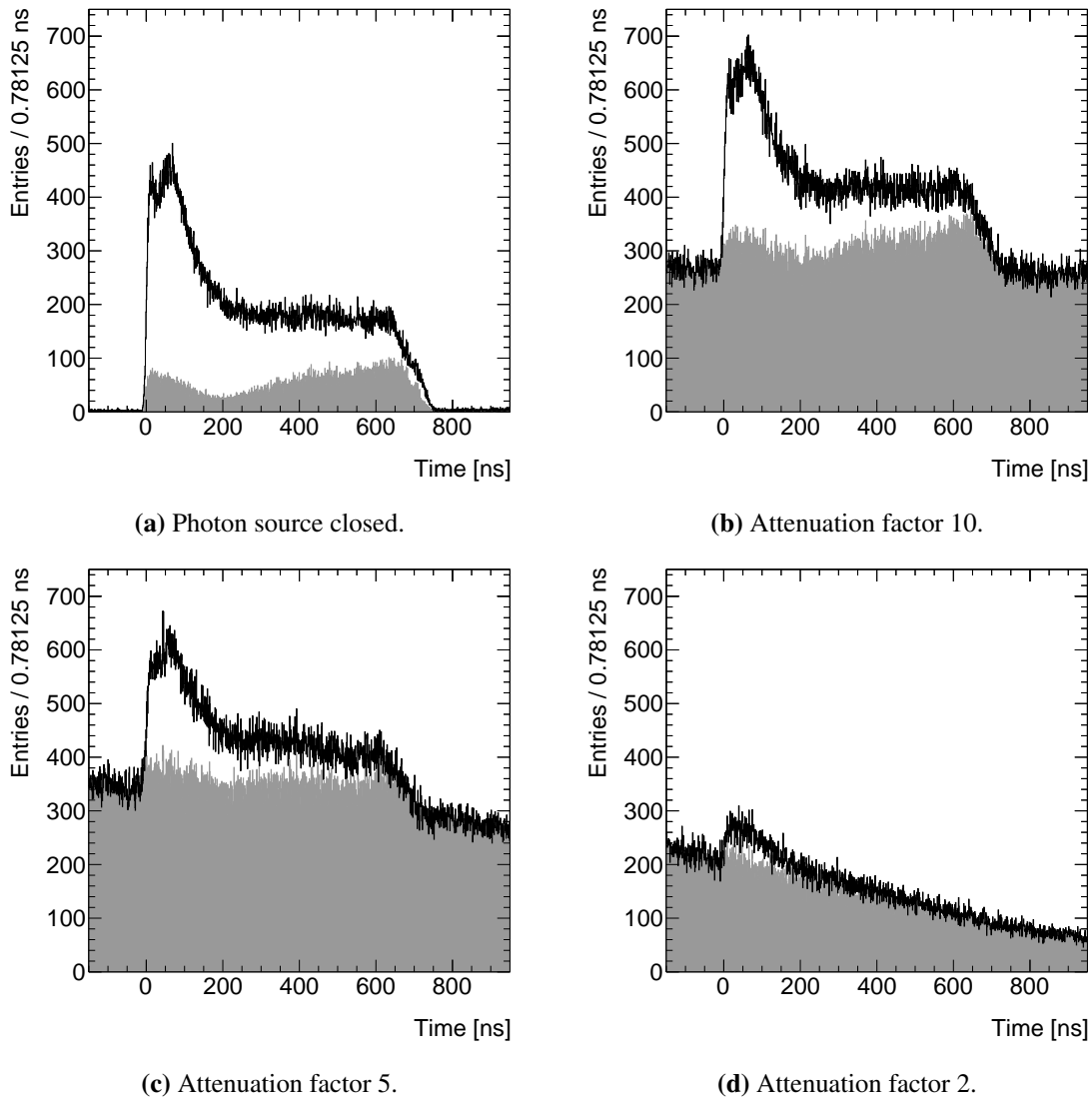


Figure 5.5: Cumulative drift time spectra of all 24 irradiated tubes read out with minimum dead time at different irradiation levels. The black histogram shows all hits, the grey area only hits with drift radii deviating more than 1 mm from the muon track reconstructed by the beam hodoscope. In the case without background irradiation (a) the latter are uniformly distributed noise hits plus, in the range $t_0 < t < t_{\max}$, hits of δ -electrons (predominantly at small drift times) and hits from secondary discriminator threshold crossings (predominantly at large drift times). With increasing irradiation levels (b, c), the fraction of hits with deviating drift radii increases. At the highest irradiation level (d), the contribution of uncorrelated background hits is no longer flat but decreases approximately exponentially with the measured drift time due to overflowing hit buffers of the AMT chip.

Table 5.1: Counting rates and hit multiplicities measured in the four MDT tubes in the active area of the beam hodoscope at two irradiation levels (attenuation factors 10 and 5) with minimum and maximum dead time and with and without the requirement of >40 ADC counts to eliminate small (predominantly noise) hits. The rates are corrected for the measured dead times (cf. section 5.3.1) according to equation (4.2). The last column specifies the hit multiplicity for minimum dead time, the ratio of the fourth rate column to the second, where the hit multiplicity is equal to 1.

Channel number		Rate [kHz/tube]				Hit multiplicity
		Max. dead time, N^{\max}		Min. dead time, N^{\min}		
		All hits	ADC > 40	All hits	ADC > 40	
Att. 10	7	465 ± 7	259 ± 5	597 ± 8	328 ± 6	1.27 ± 0.03
	15	315 ± 6	228 ± 5	424 ± 7	303 ± 6	1.32 ± 0.04
	16	251 ± 5	224 ± 5	347 ± 6	300 ± 6	1.34 ± 0.04
	23	305 ± 6	241 ± 5	402 ± 7	308 ± 6	1.28 ± 0.04
Att. 5	7	801 ± 8	456 ± 6	1015 ± 11	661 ± 9	1.45 ± 0.03
	15	625 ± 7	461 ± 6	782 ± 10	595 ± 9	1.29 ± 0.03
	16	495 ± 7	430 ± 6	634 ± 9	557 ± 8	1.30 ± 0.03
	23	533 ± 7	429 ± 6	697 ± 9	565 ± 8	1.32 ± 0.03

$\underbrace{\hspace{10em}}$	$\underbrace{\hspace{10em}}$	$\underbrace{\hspace{10em}}$	$\underbrace{\hspace{10em}}$
“counting rate”	“hit rate”	“counting rate”	“hit rate”
N_{count}^{\max}	N_{hit}^{\max}	N_{count}^{\min}	N_{hit}^{\min}

Another observation from Figure 5.4 is the difference in counting rate between minimum and maximum dead time at the same irradiation level. With minimum dead time, the total counting rate is roughly 50 % higher due to the higher hit multiplicity caused by secondary discriminator threshold crossings. Table 5.1 summarises the rates measured in the four drift tubes covered by the beam hodoscope separately with minimum and maximum dead time, both with and without requiring >40 ADC counts which eliminates very small and short pulses, i.e. noise hits. For a given irradiation level, the rates obtained in the individual drift tubes agree very well when requiring >40 ADC counts, while without this requirement they vary significantly between the channels, in particular channel 7 shows a much higher noise level.

Depending on the nature of the rate effect to be studied, it makes sense to include or exclude the noise hits in the rate measurement. The spatial resolution depends mainly on space charge effects and, hence, on the rate of particle hits, referred to as “hit rate”, which is obtained with maximum dead time (where the hit multiplicity is 1) and the requirement of >40 ADC counts listed in the second rate column of Table 5.1.

The 3σ -efficiency, on the other hand, depends mainly on the counting rate including noise hits, as in the first and third rate column of Table 5.1.

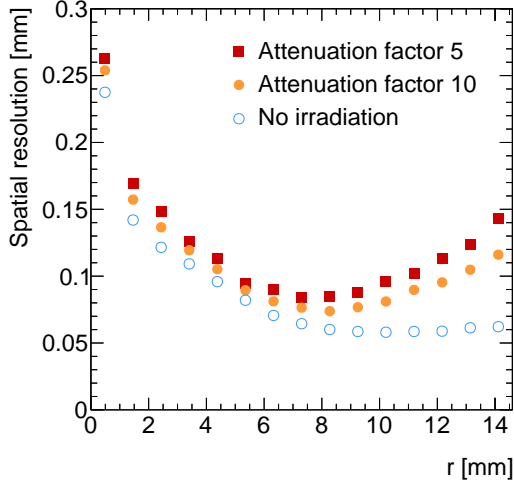


Figure 5.6: Single-tube spatial resolution as a function of the drift radius for different irradiation rates and maximum dead time averaged over the four drift tubes.

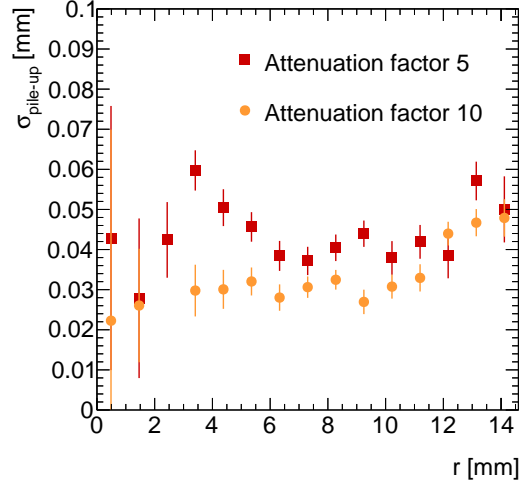


Figure 5.7: Degradation of the single-tube spatial resolution for minimum dead time averaged over the four drift tubes (see text).

The hit multiplicity for minimum dead time is, according to equations (4.1) and (4.2),

$$m_{\text{hit}} = \frac{N^{\min}}{N^{\max}} = \frac{n^{\min} (1 - n^{\max} \cdot t_{\text{dead}}^{\max})}{n^{\max} (1 - n^{\min} \cdot t_{\text{dead}}^{\min})}. \quad (5.1)$$

The results for m_{hit} are given in Table 5.1. When read out with minimum dead time, photon signals in MDT tubes cross the discriminator threshold on average 1.3 times.

5.3.4 Spatial Resolution

Figure 5.6 shows the single-tube spatial resolution as a function of the drift radius for maximum dead time at the different irradiation levels. The spatial resolution is determined from the distribution of the track residuals $\delta = r - r_{\text{track}}$, where r is the drift radius measured in a MDT tube and r_{track} the expected value from the track reconstructed with the beam hodoscope and extrapolated to the tube. The residual distribution is fitted with a Gaussian function plus flat background (see equation (4.7)) in bins of the drift radius. The width σ of the Gaussian function defines the spatial resolution. Time slewing corrections are applied as described in section 4.3.3.

Without photon irradiation, the spatial resolution improves with increasing drift radius from about 250 μm in the vicinity of the wire to approximately 60 μm for $r > 7$ mm. With increasing irradiation rate, the spatial resolution degrades due to space charge effects. With the non-linear

Ar/CO₂ drift gas, space charge fluctuations (cf. section 3.3.2) have a strong impact on the spatial resolution, predominantly for $r > 6$ mm. The degradation at smaller drift radii is mainly caused by the drop of the gas amplification due to space charge, which is equivalent to an increase of the discriminator threshold (cf. section 3.3.1). Signal pile-up does not contribute significantly to the degradation of the spatial resolution when the MDT tubes are read out with the maximum dead time of 820 ns, as the typical baseline restoration time is approximately 600 ns.

To study the effect of signal pile-up, the spatial resolution for maximum and minimum dead time are compared. Figure 5.7 shows the extra contribution to the spatial resolution due to pile-up effects when the minimum dead time is used

$$\sigma_{\text{pile-up}}(r) = \sqrt{\sigma_{\text{max}}^2(r) - \sigma_{\text{min}}^2(r)},$$

where $\sigma_{\text{max}}(r)$ and $\sigma_{\text{min}}(r)$ are the measured spatial resolutions for maximum and minimum dead time, respectively. The space charge effects are essentially the same for minimum (220 ns) and maximum (820 ns) dead time as the drift times of the ions forming the space charge are much longer (~ 3 ms). Hence, the degradation of the spatial resolution can be fully attributed to signal pile-up. As can be seen from Figure 5.7, the degradation shows no strong radial dependence and is on average 35 μm and 45 μm for the measurements with attenuation factors 10 ($N_{\text{hit}}^{\text{max}} = 260$ kHz/tube) and 5 ($R_{\text{hit}}^{\text{max}} = 439$ kHz/tube), respectively. The dependence of the average drift tube spatial resolution on the photon hit rate is shown in Figure 5.8 both for minimum and maximum dead time. The function

$$\bar{\sigma}(N) = \sqrt{P_1^2 + N \cdot \left(\frac{P_2}{1 + N \cdot P_3} \right)^2}, \quad (5.2)$$

derived in [53], is fitted to the data points and plotted as a dashed line, where P_1 is the average resolution at zero rate and $\frac{P_2}{1+N \cdot P_3}$ the amplitude of the resolution deterioration.

5.3.5 Efficiency

In contrast to the spatial resolution which degrades slightly at high rates for operation with minimum compared to maximum dead time, the 3σ -efficiency (see section 4.5) improves significantly. Figure 5.9 shows the radial dependence of the 3σ -efficiency for the different irradiation levels.

The predominant cause of efficiency loss at high counting rates is due to the electronics dead time as described by equation (3.4). The 3σ -efficiency depends on the counting rate, including accidental hits from noise or afterpulsing that also trigger the dead time mechanism of the ASD chip. Both the noise and the afterpulsing rate depend strongly on the discriminator threshold which was set to the quite low value of -34 mV, resulting in relatively high accidental rates,

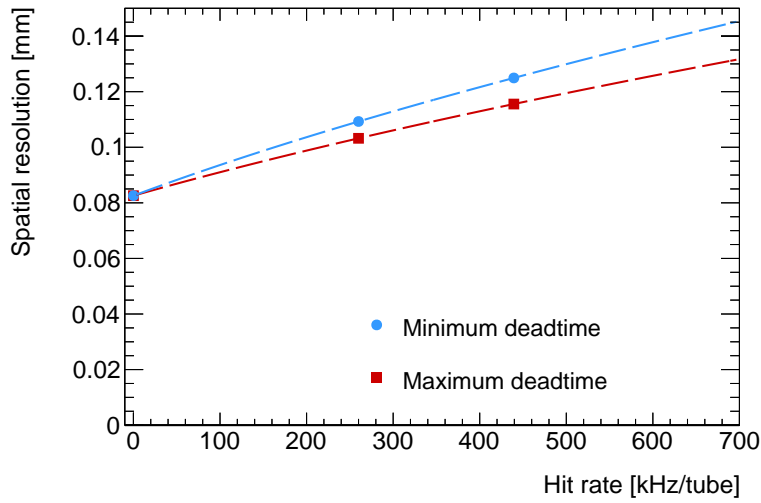


Figure 5.8: Overall single-tube spatial resolution as a function of the photon hit rate for the minimum (220 ns) and maximum (820 ns) dead times. The dashed lines show fits of equation (5.2) to the data points.

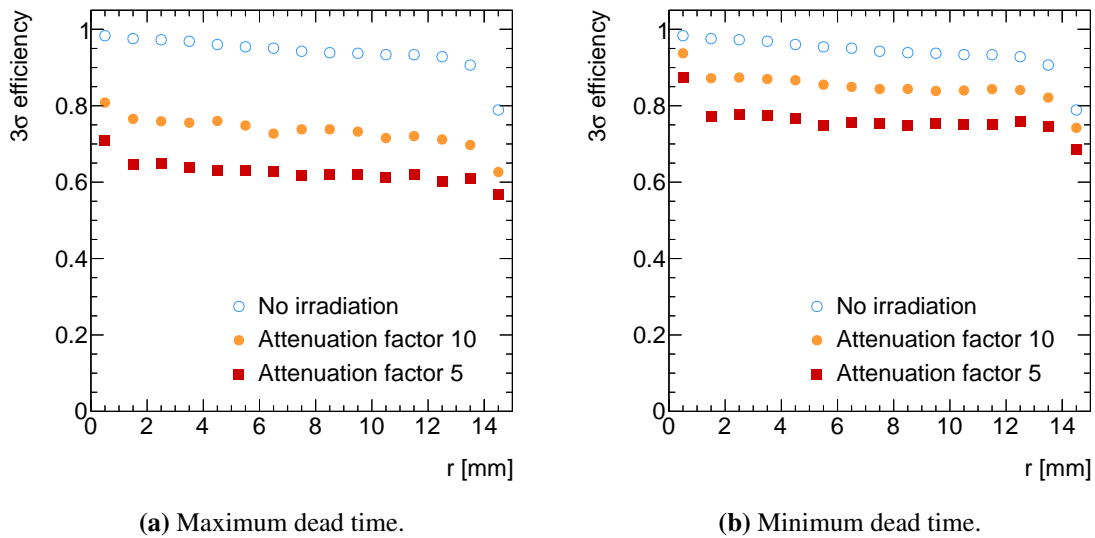


Figure 5.9: Average 3σ -efficiency of the four drift tubes in the active area of the beam telescope as a function of the drift radius for different irradiation rates.

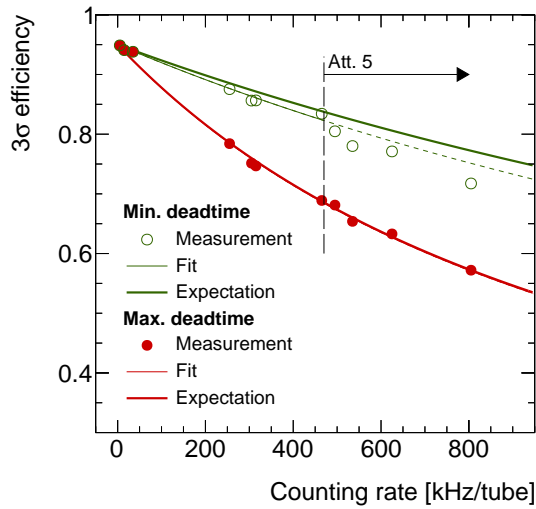


Figure 5.10: Dependence of the 3σ -efficiency of MDT tubes on the dead time corrected counting rate. The measurements are compared to expectations according to equations (3.4) and (3.5) for fixed dead times of 222 ns and 823 ns and to fits with the dead time as free parameter (see text). For maximum dead time, the fit and the expectation coincide. The difference for minimum dead time is due to signal pile-up not included in the expectation.

in particular in one drift tube (channel 7). The channel dependence is due to variations of the amplifier gain and discriminator threshold among the different channels of the ASD chips caused by the production process.

Figure 5.10 shows the average 3σ -efficiency as a function of the dead time corrected counting rate N_{count} without the requirement of >40 ADC counts. Four different counting rates, corresponding to the four MDT tubes in the active area of the beam hodoscope, are obtained for each attenuation setting (see Table 5.1). Fits of equations (3.4) and (3.5), respectively, with the dead time as a free parameter are shown together with the expectation for fixed minimum and maximum dead time of 222 ns and 823 ns, respectively. For attenuation level of 5 and the minimum dead time, the total rate exceeded the specifications of the AMT chip as mentioned above, causing additional efficiency losses due to buffer overflows. Indeed, one can see a step in the efficiency. The corresponding points were excluded from the fit. The results of the fit for minimum and maximum dead time are (252.9 ± 3.5) ns and (826.0 ± 5.6) ns, respectively. While there is perfect agreement with the expectation for the maximum dead time, there is a significant deviation for the minimum dead time which is due to signal pile-up.

6

sMDT Chambers Under Photon Irradiation

6.1 Introduction

Approximately 70% of the hits recorded by the ATLAS MDT chambers are caused by the photon component of the cavern radiation background with an average photon energy of about 1 MeV [46]. As this is the predominant background in the muon detectors of the LHC experiments, the Gamma Irradiation Facility (GIF) [38] was built at CERN in 1997 in order to facilitate testing of large-area muon detectors under conditions close to the ones during LHC operation.

In this chapter, measurements carried out at the GIF with the sMDT prototype chamber described in section 2.3.2 are discussed. The tests were performed in view of the potential use of sMDT chambers in the high-rate regions of the ATLAS Muon Spectrometer at HL-LHC [43]. The experimental setup is described in section 6.2, the data acquisition and the irradiation and ambient conditions are discussed in section 6.3 and the calibration of the test setup and the data analysis in sections 6.4 and 6.5, respectively.

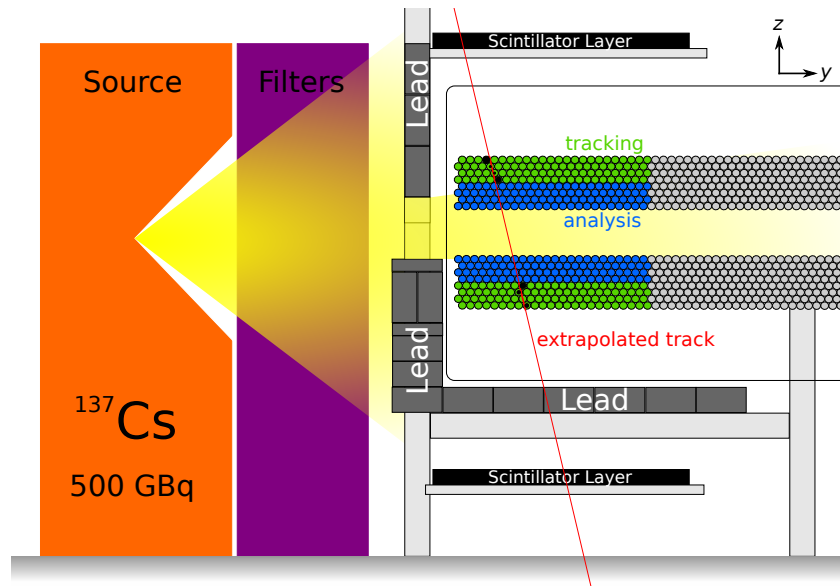


Figure 6.1: Schematic view of the experimental setup at the GIF with the sMDT chamber mounted horizontally, as close as possible to the source in order to achieve the maximum possible photon flux. The chamber is divided into two sections, a test part (blue) exposed to the photon flux and a tracking part (green) shielded against the irradiation with lead like the two layers of scintillation counters used to trigger in coincidence on cosmic ray muons. An additional layer of lead above the bottom scintillator layer absorbs low energy muons that are subject to strong multiple scattering.

6.2 Experimental Setup

The GIF uses a ^{137}Cs source emitting 662 keV photons in 85 % of its decays. A series of absorbers in front of the source allows to adjust the photon flux over four orders of magnitude. To achieve homogeneous irradiation of large detectors, a thin lens-shaped filter is used rendering the photon flux uniform in the vertical direction. ^{137}Cs was chosen because the photon energy is close to the average photon energy of the cavern background of the LHC experiments and because of its long half-life of 30 years which still allowed the high-rate measurements presented in this chapter.

When put into operation, the GIF was accompanied by a narrow high-energy muon beam (X5) which allowed to record many events with muon tracks within short time like for the measurements with MDT tubes in 2004 described in the previous chapter. Originally, the ^{137}Cs source had an activity of 740 GBq offering a maximum photon flux of $0.8 \cdot 10^7 \text{ cm}^{-2} \text{ s}^{-1}$ at 50 cm distance. By the time of the present measurements, the activity had dropped to around 500 GBq and the muon beam was no longer available. Hence, cosmic ray muons had to be used for the tests.

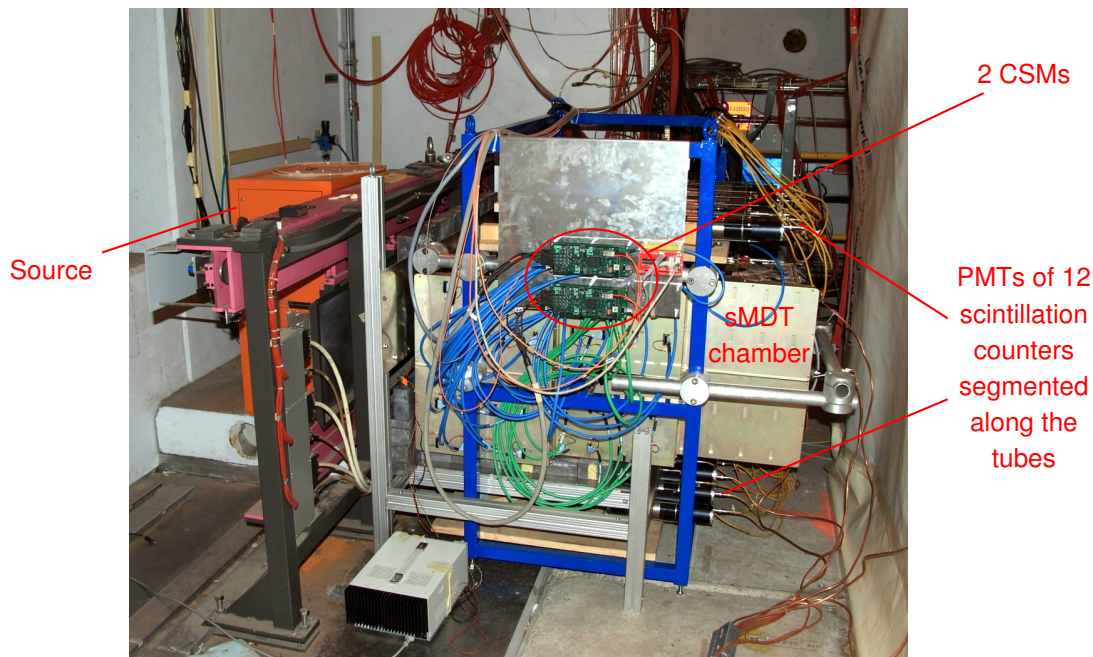


Figure 6.2: Photograph of the experimental setup at the GIF (cf. Figure 6.1).

A schematic view of the experimental setup is shown in Figure 6.1. Figure 6.2 shows a photograph of the installation. The 2×8 layer sMDT prototype chamber described in section 2.3.2 was mounted horizontally, as close as possible to the photon source in order to reach the maximum possible flux. The tubes closest to the source and connected to the read-out electronics are 95 cm long. The sMDT chamber served both for reconstruction of reference tracks of cosmic ray muons and as test device. For this purpose, the chamber was divided into a tracking and a test part: The tracking part comprised the four top and four bottom tube layers which were shielded against the source with lead to allow for clean reconstruction of cosmic ray muon tracks. The test part comprised the 2×4 tube layers in between which were exposed to the full photon flux decreasing with distance from the source.

Two layers of scintillation counters were used in coincidence to provide a cosmic ray trigger and to measure the precise muon passage times. The output signals of all scintillation counters were fed to discriminators. The discriminator outputs of each layer were connected by logic ORs and the resulting two signals by a logic AND to form the trigger signal. To avoid unnecessary time jitter between the two layers, the OR signal of the upper layer was delayed by a few ten nanoseconds. In addition, the discriminator outputs of all scintillation counter signals were fed to a TDC module that was read out synchronously with the sMDT chamber. A 5 cm thick layer of lead above the bottom scintillation counter layer was used to harden the cosmic ray muon energy spectrum to reduce the influence of multiple scattering on the spatial resolution.

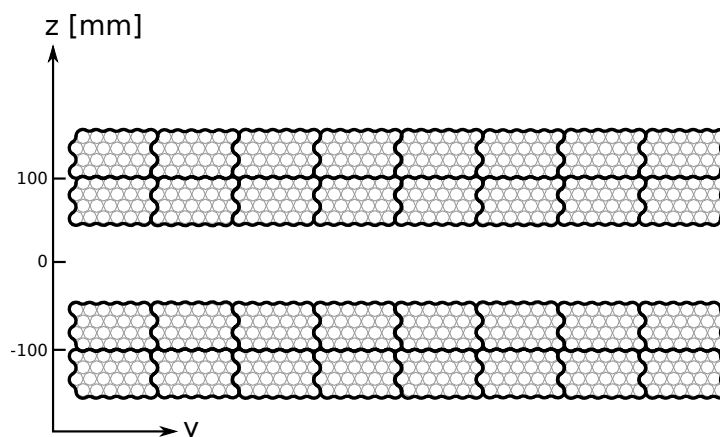


Figure 6.3: Mapping of the drift tubes to the mezzanine boards. The 24 drift tubes in each of the black bordered areas are read out by one mezzanine board with one AMT chip with limited total rate (see text).

The sMDT chamber was operated at nominal ASD operating parameters (see Table 2.3) with Ar/CO₂ (93/7) gas at 3 bar absolute pressure and a wire potential of 2730 V corresponding to the nominal gas gain of $2 \cdot 10^4$ of the MDT chambers. The gas flow corresponded to roughly five chamber gas volume exchanges per 24 hours.

6.3 Data Acquisition and Ambient Condition Monitoring

In this section, the electronics settings and environmental conditions under which data were recorded are described.

6.3.1 Front-End Electronics

The standard ATLAS MDT active front-end electronics described in section 2.2.2 with minimum dead time setting matching the shorter maximum drift time of 185 ns was used to read out the sMDT chamber. The mezzanine board connecting to 24 drift tubes contain three 8-channel Amplifier/Shaper/Discriminator (ASD) chips and one 24-channel ATLAS Muon TDC (AMT) chip (see Figure 6.3). The AMT can handle counting rates of up to 400 kHz per channel when all 24 channels are used. This is too low for the rates targeted for the present measurements. In order to allow for the study of the sMDT performance at very high rates, a fraction of the 24 channels was deactivated increasing the maximum counting rate for the remaining channels (see below).

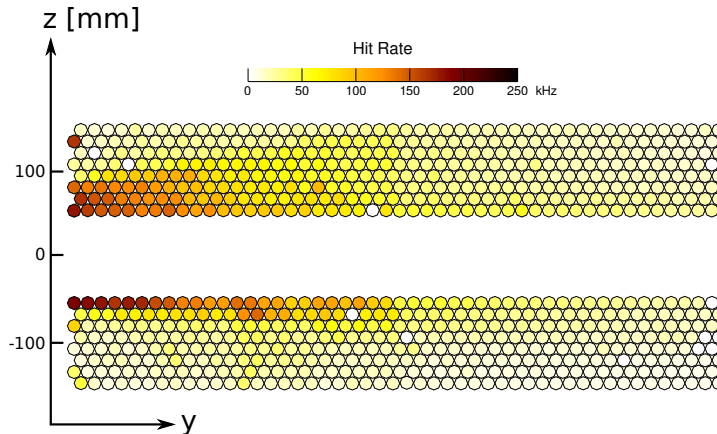


Figure 6.4: Counting rates in the sMDT chamber in the GIF with attenuation factor 5.

6.3.2 Irradiation Conditions

To optimise the lead shielding and select the channels to be deactivated, the counting rate distribution in the chamber was measured as a first step. For this purpose, the photon flux was reduced by a factor 5 by means of the adjustable absorbers in front of the source to measure the counting rate in all drift tubes without hitting the rate limit of the AMT. About 10 000 random triggers were taken and the hit rate distribution in the chamber calculated according to equations (4.1) and (4.2). The result is visualised in Figure 6.4.

One can see that the lead shielding is very effective, especially in the bottom multilayer where the irradiation is mostly constrained to the uppermost tube layer. In the upper multilayer, the effect of the shielding is more blurred due to photon scattering in the aluminium bar supporting the lead blocks. A few dead channels can be seen caused by broken wires that required to disconnect tubes from the high-voltage distribution.

After the validation of the shielding, the attenuation factor of the source was set to 1 corresponding to maximum flux to select the channels to be deactivated. Figure 6.5 shows the counting rate distribution obtained after these modifications. For the further analysis, only the left half of the chamber with counting rates in the range of 500 to 1200 kHz per channel in the irradiated test part and $\lesssim 150$ kHz in the shielded tracking part is of interest.

To verify that the rates do not exceed the electronics limits, the error words in the AMT output were enabled indicating amongst errors buffer overflows. The only AMT errors observed during the whole measurement period were few ten coarse time counter errors in the first CSM channel (AMT0) of each multilayer occurring at the very beginning of each run before the first general reset of the AMT chips is performed. No further errors were encountered afterwards.

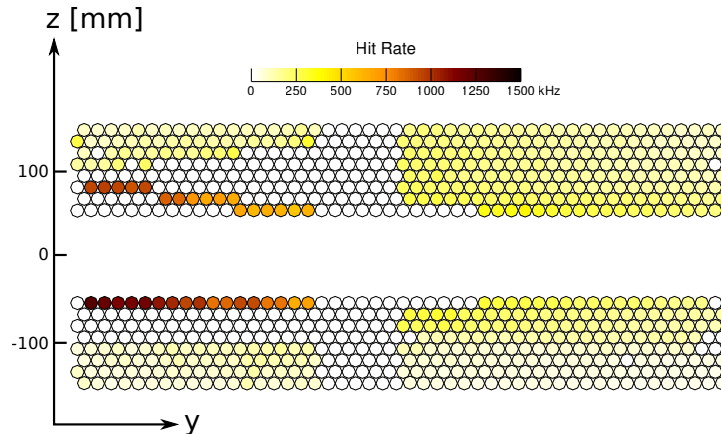


Figure 6.5: Counting rates in the sMDT chamber in the GIF with attenuation factor 1. Part of the channels on the mezzanine boards in the strongly irradiated region are deactivated (white).

6.3.3 Monitoring of Ambient Conditions and Slow Control

Ambient conditions like temperature, humidity, and gas pressure can affect the performance of the chamber in the following ways:

- The drift properties in the gas depend on the temperature. The maximum drift time t_{\max} increases by approximately 1.5 ns K^{-1} temperature increase due to reduction of the drift velocity.
- Variations of the gas pressure and consequently of the gas density affect the ionisation charge density and the gas amplification.
- The ambient humidity increases leakage currents in the high-voltage distribution.

For these reasons, temperature and humidity were monitored and recorded throughout the whole measurement period (cf. Figure 6.6). The pressure of the gas mixture in the chamber was set to 3 bar absolute within ± 1 mbar over the whole measurement period (cf. Figure 6.7).

Also the currents drawn by the high-voltage channels supplying the two multilayers were monitored (see Figure 6.8). The dark current of each multilayer was with few ten nanoamperes very low despite high relative humidity of 40 to 65 %. With the source opened, the current increases linearly with the hit rate, the gas amplification and the primary ionisation charge of the photons according to equation (4.3). As expected, the currents drawn by the two multilayers differ reflecting the different hit rates (compare Figure 6.4).

The daily variations of the currents are in phase with the variations of the temperature and reflect variations of the gas amplification due to variations of the gas density. The gas amplification

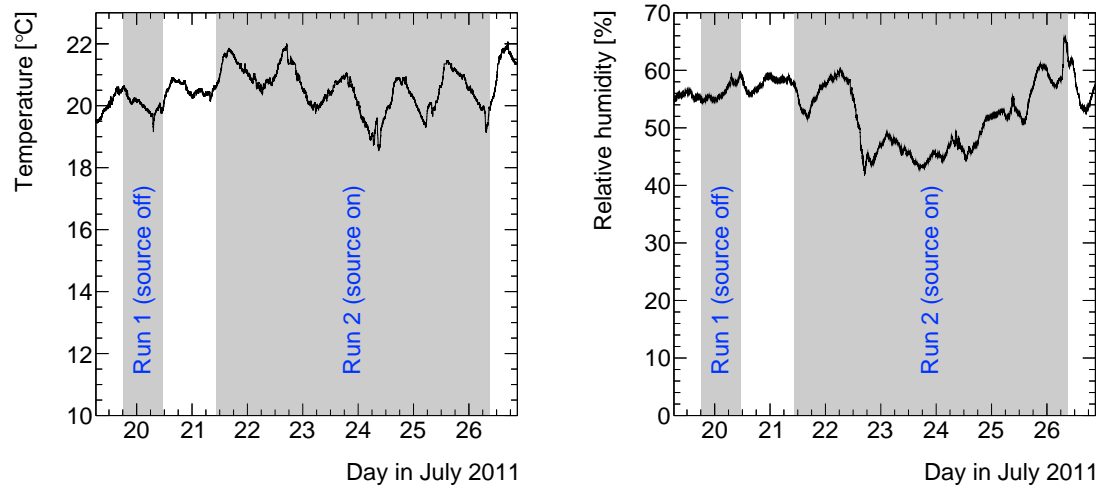


Figure 6.6: Temperature (left) and relative humidity (right) variations during the measurement campaign.

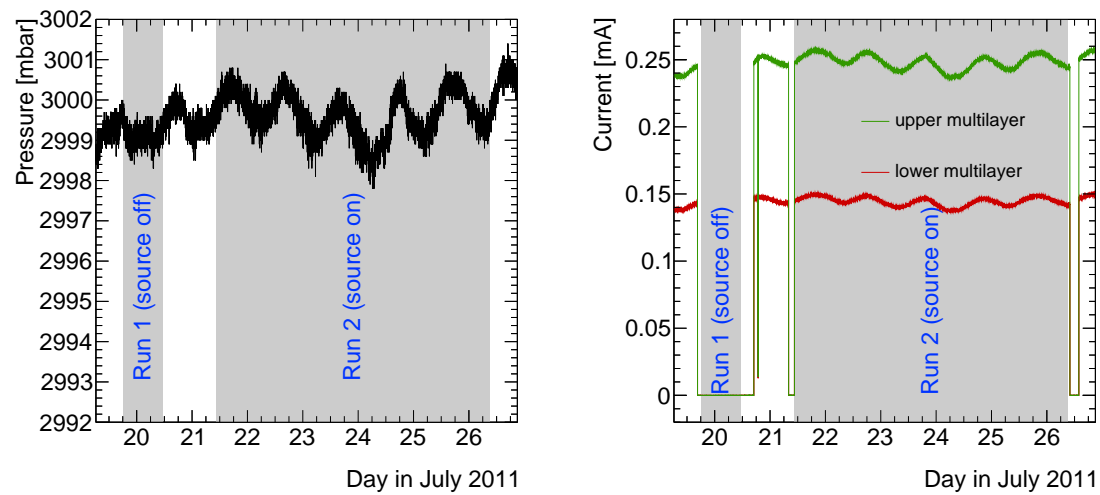


Figure 6.7: Variation of the gas pressure during the measurement campaign.

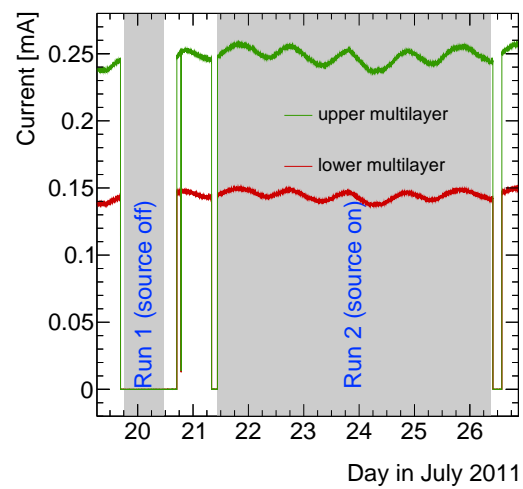


Figure 6.8: Variation of the currents drawn by the two multilayers during the measurement campaign.

according to Diethorn's equation (cf. equation (3.1)) is given by

$$G = \left[\frac{E(r_w)\rho_0}{E_{\min}(\rho_0)\rho_{\text{gas}}} \right]^{\frac{r_w E(r_w) \ln 2}{\Delta V}}$$

with the electric field $E(r_w)$ at the wire surface, the gas densities ρ_{gas} and ρ_0 (at $T_0 = 20^\circ\text{C}$), and the gas mixture dependent parameters $E_{\min}(\rho_0)$ and ΔV . For constant pressure with $\rho_{\text{gas}} \propto T^{-1}$ on obtains

$$G \propto \left(\frac{T}{T_0} \right)^{\frac{\alpha E(r_w) \ln 2}{\Delta V}} \approx \left(\frac{T}{T_0} \right)^{10},$$

i.e. temperature increases by 1 to 2 K cause gain increases by 3 to 7 %. The pressure variations have the opposite effect on the gas amplification, but they are $< 1\%$ such that the temperature effects dominate.

6.4 Data Preparation

In this section, the setup specific calibration procedure is discussed. The general methods are described in chapter 4.

6.4.1 Time and Drift Distance Calibration

As discussed in section 4.3.1, several time offsets have to be considered in order to avoid time jitter in the drift time measurement. In the GIF test setup, special care had to be taken for the timing of the trigger signals from the 2×12 scintillation counters arranged in two layers, above and below the sMDT chamber.

For a trigger, at least one hit in each scintillation counter layer is required. The signals of the upper layer were delayed by few nanoseconds such that the trigger time is always defined by the hit in this layer. The scintillation counters are also read out with a TDC module (CAEN V775N) allowing to correct for the trigger time offset

$$t_0^{\text{trigger}} = t_0^{\text{sct},i}, \quad (6.1)$$

given by the time $t_0^{\text{sct},i}$ measured in the i^{th} scintillation counter of the upper layer that caused the trigger (cf. section 4.3.1).

By calibrating the scintillation counter times with respect to the minimum drift times (t_0) of the drift tubes, two time jitter contributions are corrected for at the same time: propagation time variations both in the scintillation counters and along the drift tubes. First, the drift tube t_0 -values are determined as described in section 4.3.1 ignoring the trigger time offset ($t_0^{\text{trigger}} = 0$). The drift

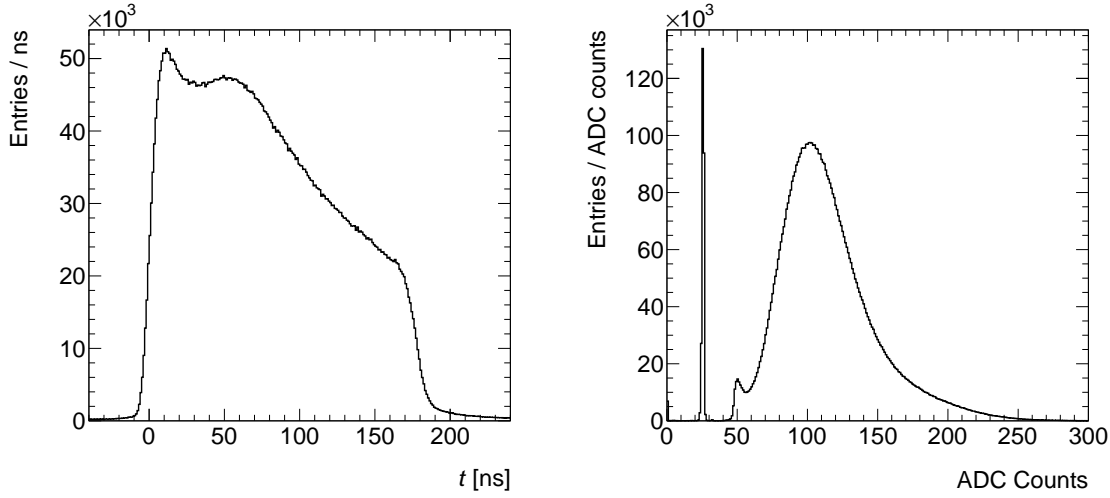


Figure 6.9: Cumulative drift time (left) and ADC (right) spectra of all sMDT drift tubes after time slewing corrections with the gamma source switched off. The small peak around 50 ADC counts is the end of the noise distribution which is cut off at 45 ADC counts by the discriminator. The sharp peak at 25 ADC counts is caused by failing charge measurement due to very small and short (noise) signals. Usually hits with less than 40 ADC counts are rejected in the track reconstruction.

times are corrected for these t_0 -offsets and the drift time spectrum is split into 12 spectra, each corresponding to a scintillation counter that triggered the event.

Equation (4.5) is then fitted to each of the 12 drift time spectra providing the trigger time $t_0^{\text{sct},i}$ for the drift tubes for each scintillation counter. Applying equation (6.1) changes the drift tube t_0 -values. Hence, t_0 and $t_0^{\text{sct},i}$ are determined iteratively. A cumulative drift time spectrum of all drift tubes after the trigger time corrections without irradiation is shown in Figure 6.9. Afterwards, the space-to-drift-time relationship $r(t)$ is obtained using the autocalibration method described in section 4.3.2.

6.4.2 Time Slewing Correction

Time slewing corrections are applied as described in section 4.3.3. Figure 6.10 shows the distributions of the time slewing Δt of a hit as a function of $\Delta Q = Q - Q_{\text{peak}}$ in intervals of the drift radius superimposed by the mean values of Δt in each ΔQ bin and a linear fit to the mean values. The r -dependent correction function obtained in this way is the one shown in Figure 4.4. The rise time of the leading edge of the drift time spectrum after the time slewing correction in Figure 6.9 is $T_0 = (2.20 \pm 0.01)$ ns.

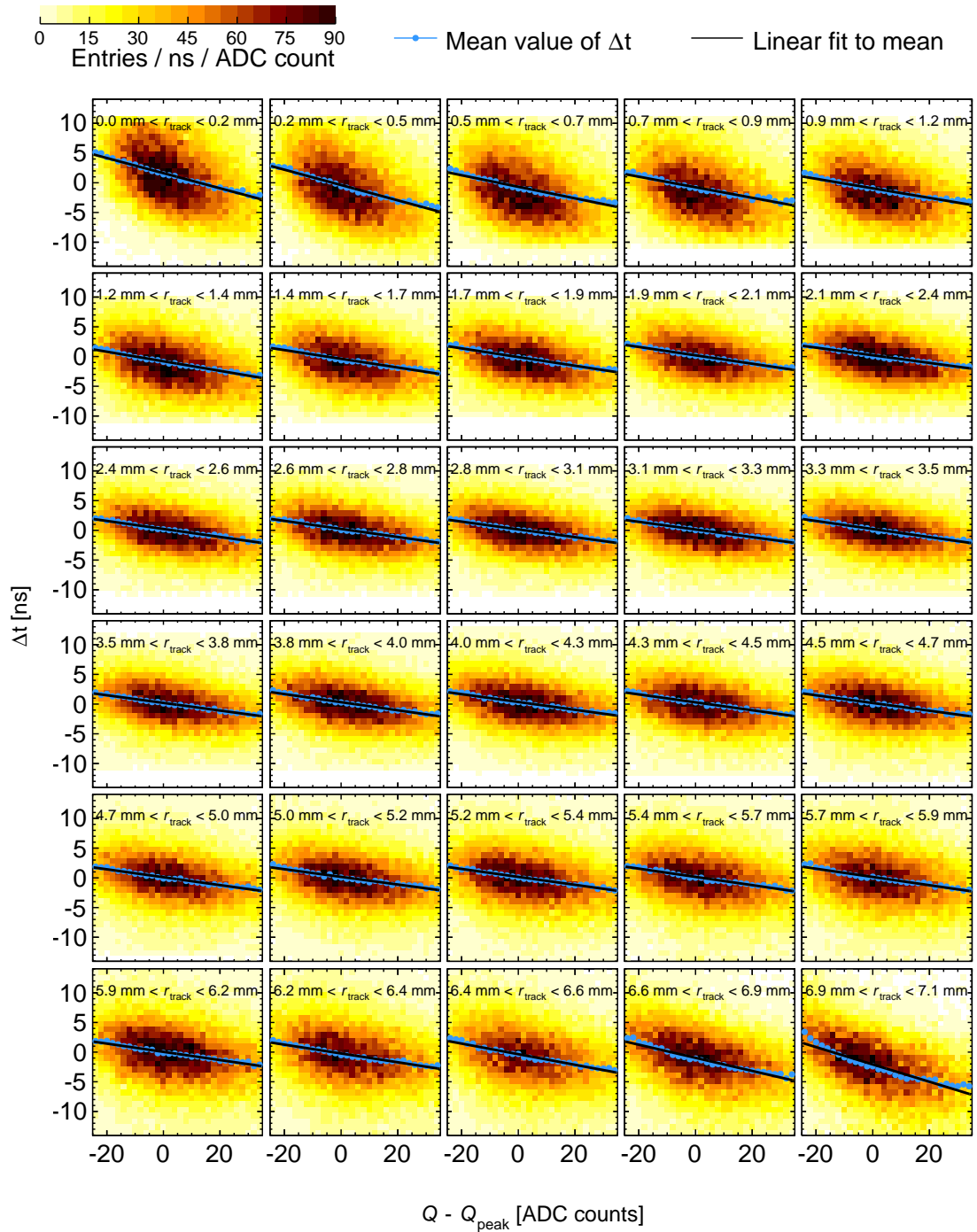


Figure 6.10: Dependence of the time slewing Δt the deviation of the charge measurement from the most probable charge ($Q - Q_{\text{peak}}$) and on the muon impact radius r_{track} .

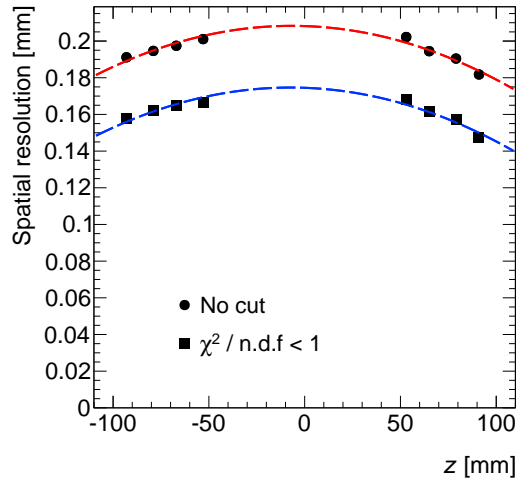


Figure 6.11: Dependence of the average spatial resolution of the analysed drift tubes without irradiation and without multiple scattering correction as a function of the tube layer z -coordinate with and without the quality requirement $\chi^2 / \text{n.d.f.} < 1$ on the reference track (see text).

6.4.3 Spatial Resolution

As we rely on cosmic ray muons with a large low energy fraction, multiple scattering contributes significantly to the spatial resolution depending on the distance between the analysed tube and the reference track supporting points and the amount of material in between, mainly the tube walls (cf. Figure 6.1).

Figure 6.11 shows the average spatial resolution of the analysed drift tubes as a function of the tube layer z -coordinate obtained with the method described in section 4.4 without corrections for multiple scattering. The spatial resolution degrades towards the centre, where the amount of material between the track supporting points and the analysed tubes is largest in both directions.

Due to the low average energy of cosmic ray muons, the spatial resolution is significantly worse than the $(106 \pm 2) \mu\text{m}$ from previous test beam measurements with high energy muons [42]. As we are interested in the resolution for muons with energies $\gg 1 \text{ GeV}$, the multiple scattering contribution $\sigma_{\text{MS}}(z)$ is subtracted quadratically from the measured value:

$$\sigma_{\text{tube}} = \sqrt{\sigma_{\text{meas}}^2 - \sigma_{\text{MS}}^2(z)}.$$

To avoid large uncertainties, it is desirable to reduce σ_{MS} as far as possible. Figure 6.12 shows the dependence of the measured average spatial resolution of the analysed drift tubes as defined in equation (4.10) on the χ^2 per degree of freedom of the track fit in the reference region. It can be seen that the $\chi^2 / \text{n.d.f.}$ value is very sensitive to multiple scattering deteriorating the resolution which can be exploited to reject low energy muon tracks which are mostly affected. Requiring

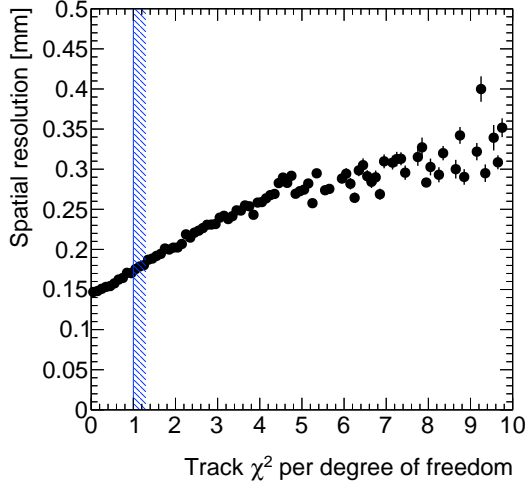


Figure 6.12: Dependence of the average spatial resolution of the drift tubes in the analysis region of the chamber on the reference track $\chi^2/\text{n.d.f.}$ of the reference track. The blue line indicates the cut applied in the analysis.

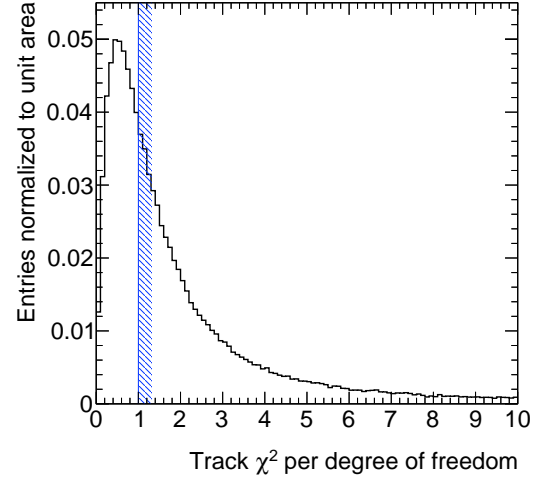


Figure 6.13: Normalised χ^2 distribution of the reference track. The blue line indicates the cut applied in the analysis.

$\chi^2/\text{n.d.f.} > 1$ keeps roughly 40 % of the tracks (compare Figure 6.13) which is still enough for the further analysis. This requirement does not bias the measured spatial resolution, because the drift tubes in the analysis part of the chamber do not contribute to the reference tracks.

After the multiple scattering correction to the average measured resolution $\sigma_{\text{meas}}^2(z)$ in each tube layer, the resolution obtained in the test beam, $\sigma_{\text{beam}} = (106 \pm 2) \mu\text{m}$, is expected, hence

$$\sigma_{\text{MS}}(z) = \sqrt{\sigma_{\text{meas}}^2(z) - \sigma_{\text{beam}}^2} \quad (6.2)$$

which is shown in Figure 6.14. The effects of multiple scattering have also been validated by simulation with MTGEANT-4 [37].

After subtracting the z -dependent multiple scattering contribution from the measured resolution of the individual tubes, the spatial resolution is uniform for all drift tubes (see Figure 6.15) and in good agreement with the previous test beam result. Also the radial dependence shown in Figure 6.16 agrees very well with previous measurements [40, 42, 50].

6.5 Performance Under Irradiation

With the calibration constants determined and with the understanding of the spatial resolution in the absence of irradiation, the effects of photon background can be addressed. Data were recorded

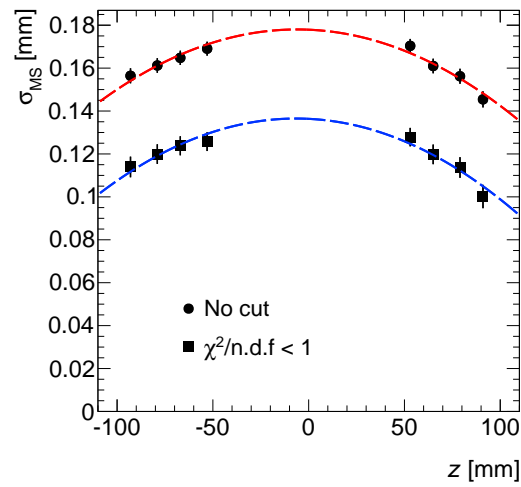


Figure 6.14: Estimate of the multiple scattering contribution to the average spatial resolution for the analysed drift tube layers according to equation (6.2).

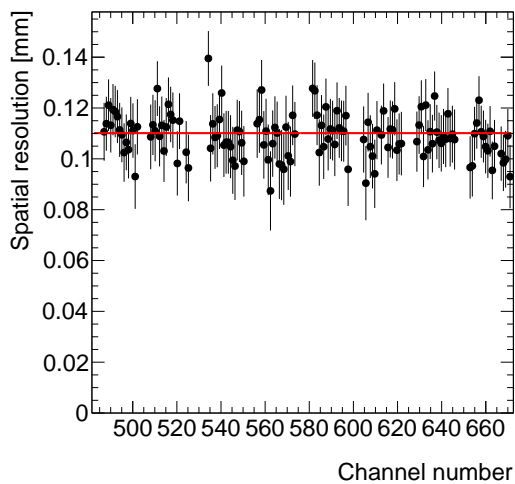


Figure 6.15: Average resolution of individual drift tubes in the analysis region corrected for multiple scattering. The mean value indicated as red line is $\langle \sigma_{tube} \rangle = (110.1 \pm 0.7) \mu\text{m}$

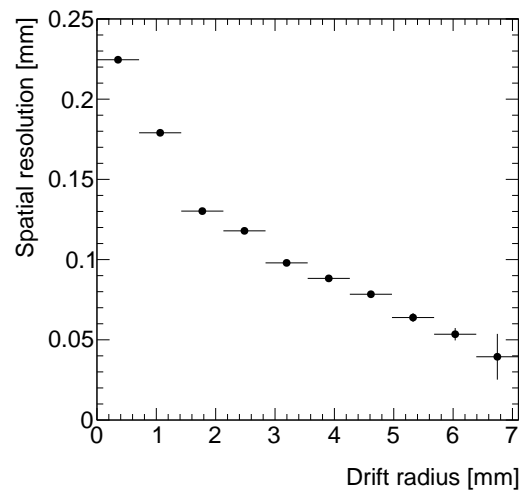


Figure 6.16: Average resolution of all drift tubes in the analysis region as a function of the drift radius.

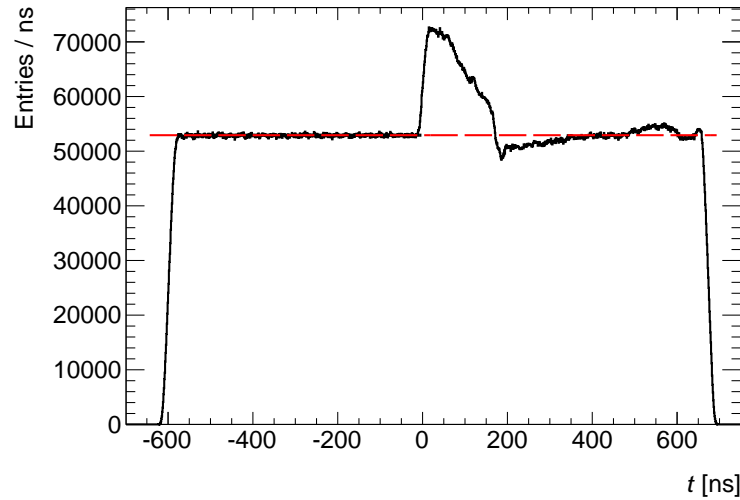


Figure 6.17: Drift time spectrum of all irradiated drift tubes at maximum photon flux. The typical spectrum of cosmic ray muons homogeneously illuminating the drift tubes emerges from a flat plateau indicated by the horizontal red dashed line. The dip at $t > t_{\max} \approx 185$ ns is due to the electronics dead time. The bump around $t \approx 550$ ns is due to afterpulsing caused by imperfect ion tail cancellation of the ASD chip (see section 5.3.2). The read-out window (search window) of the AMT chip was 1275 ns long and starts at -600 ns with respect to the minimum drift time t_0 .

at maximum photon flux (attenuation factor 1) for five days accumulating roughly 2.9 million cosmic muon events. All measurements with sMDT drift tubes have been performed with the ASD chip read out with the minimum dead time setting. Figure 6.17 shows the cumulative drift time spectrum of the irradiated drift tubes for the full data set. The typical spectrum of cosmic ray muons, as shown in Figure 6.9, emerges from an almost flat plateau caused by the uncorrelated photon hits. The dip at $t_{\max} < t < t_{\max} + t_{\text{dead}}$, where $t_{\max} \approx 185$ ns is the maximum drift time and $t_{\text{dead}} \approx 220$ ns the electronics dead time, is caused by masking of photon hits by preceding muon hits.

This section starts with the measurement of the drop of the gas amplification due to irradiation before addressing the influence of the radiation background on the spatial resolution and efficiency in sections 6.5.2 and 6.5.3, respectively.

6.5.1 Gas Gain Drop

The gas amplification G in the presence of radiation background can be measured relative to the nominal value G_0 in the absence of background radiation by means of the rising edge charge q and q_0 measured for either case with the Wilkinson ADC of the front-end electronics according

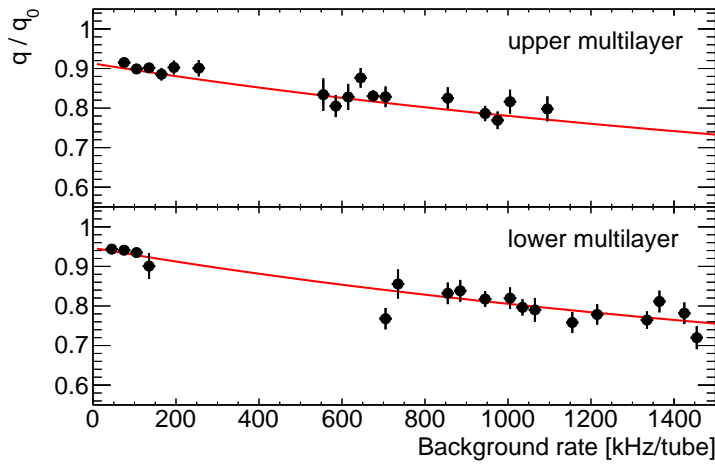


Figure 6.18: Ratio of the rising edge charge q as a function of the corrected photon hit rate relative to the value q_0 without irradiation. The red line is the expectation based on Diethorn's equation with the gas mixture dependent parameters specified in section 3.3.1 and primary ionisation charge of $Q_{\text{prim}}^y = 900 e$ taking into account the voltage drop in the noise filters of $\Delta V = 12.5 \text{ V}$ in the upper and $\Delta V = 7.5 \text{ V}$ in the lower multilayer.

to the relation

$$\frac{q}{q_0} = \frac{G}{G_0}$$

as described in section 4.2.

Figure 6.18 shows q/q_0 for both multilayers of the chamber as a function of the hit rate. The deviation from unity for extrapolation to zero rate is due to the voltage drop in the low-pass noise filters with two $25 \text{ k}\Omega$ resistors (cf. section 2.2.2) in the high-voltage lines. The two multilayers were connected to separate high-voltage channels which draw different currents I_{ML} depending under irradiation. The voltage drop is $\Delta V = 50 \text{ k}\Omega \cdot I_{\text{ML}} = 12.5 \text{ V}$ for $I_{\text{ML}} = 0.25 \text{ mA}$ in the upper and $\Delta V = 7.5 \text{ V}$ for $I_{\text{ML}} = 0.15 \text{ mA}$ in the lower multilayer under irradiation (see Figure 6.8). According to Diethorn's equation (cf. section 3.3.1), this results in a gain drop of 8.7% and 5.3% in the upper and lower multilayers, respectively. This prediction is in good agreement with the extrapolation to zero rate in Figure 6.18.

6.5.2 Spatial Resolution

Figure 6.19a shows the cumulative residual distributions as a function of the impact radius for drift tubes in the irradiated analysis part of the chamber with hit rates in the range 1300 to 1500 kHz. Comparing to the equivalent plot in the absence of radiation background in Figure 4.5,

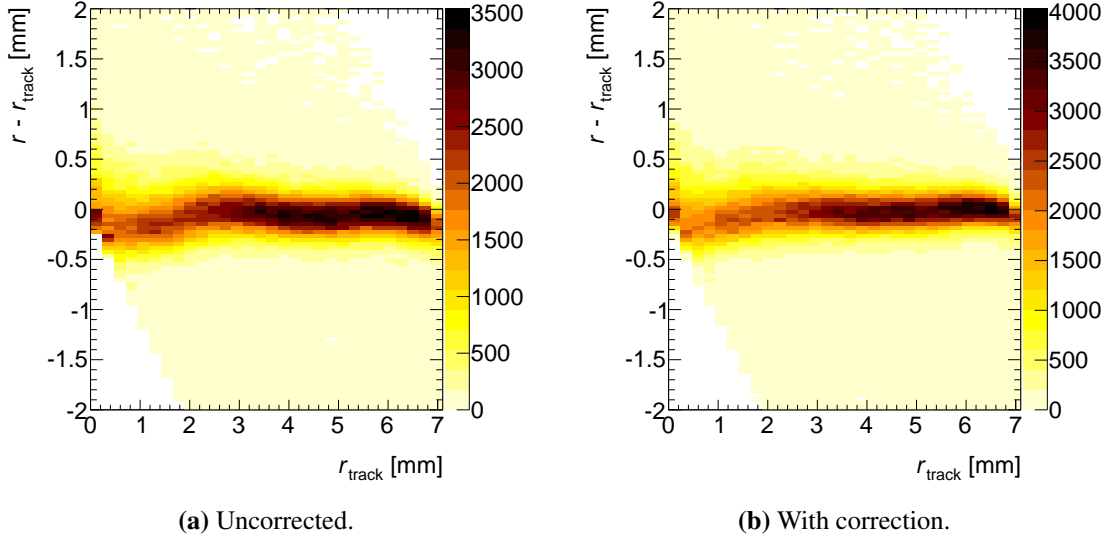


Figure 6.19: Cumulative residual distributions as a function of the drift radius for drift tubes with hit rates in the range 1300 to 1500 kHz (a) before and (b) after correction (see text).

one can already see the effect of the irradiation: The distribution is less flat and less narrow than in the non-irradiated case.

The spatial resolution of the irradiated drift tubes is determined according to the method described in section 4.4 and with time slewing and multiple scattering corrections as described above in bins of the impact radius. The impact radius (r_{track}) dependent shift of the residual distribution is corrected for with

$$r \rightarrow r - \mu(r_{\text{track}}),$$

where $\mu(r_{\text{track}})$ is the mean value of the modified normal distribution (cf. equation (4.7)) fitted to the residual distribution to avoid bias in the 3σ -efficiency determination. The residual distribution after this correction is shown in Figure 6.19b.

As the hit rate is different in each drift tube depending on its position (cf. Figure 6.5) the spatial resolution is determined individually for each tube.

Figure 6.20a shows the spatial resolution as a function of the drift radius for different hit rate intervals. Measurements for different drift tubes with hit rates in the specified intervals are combined in order to increase the statistics and to average out systematics like variations of the discriminator thresholds between channels.

The spatial resolution degrades significantly with increasing hit rate in the whole drift radius range. To distinguish the effect of signal pile-up from space charge effects on the gas gain, the resolution measurement is repeated with the requirement of a minimum time interval Δt between

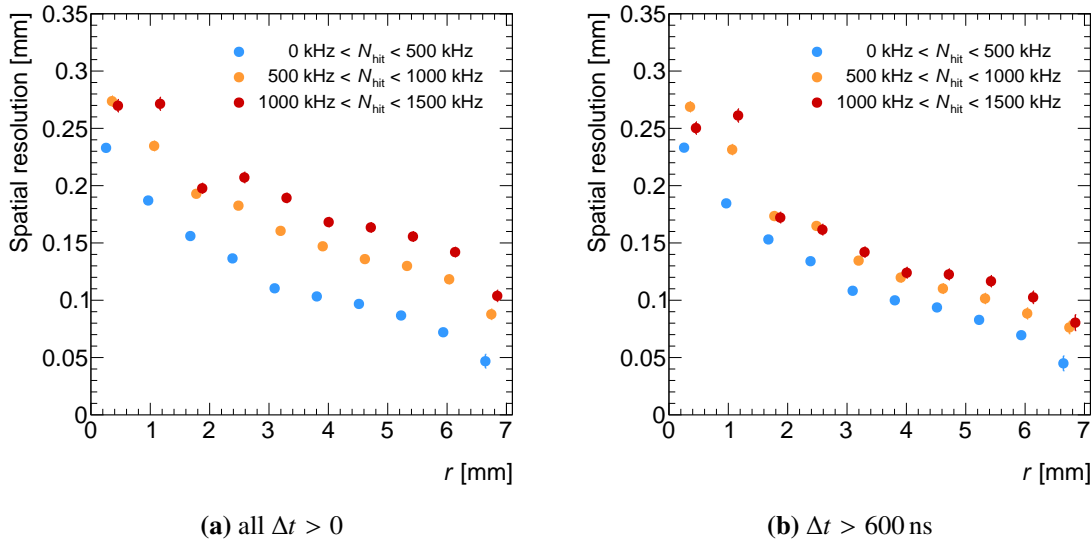


Figure 6.20: Spatial resolution of sMDT drift tubes with multiple scattering corrections as a function of the drift radius for different hit rate intervals (a) without and (b) with requirement of a minimum time interval Δt between successive hits.

successive hits which is equivalent to operating the front-end electronics with the adjustable dead time $t_{\text{dead}} = \Delta t$. The maximum possible Δt cut is 600 ns given by the start of the read-out window 600 ns before the minimum drift time t_0 (cf. Figure 6.17). The influence of space charge effects does not change with this additional requirement because Δt is small compared to the ion drift time which is approximately 1 ms in the sMDT tubes.

Figure 6.20b shows the spatial resolution as a function of the drift radius with the additional requirement $\Delta t > 600 \text{ ns}$. The deterioration of the spatial resolution due to irradiation is strongly reduced. Hence, one can conclude that for sMDT tubes (in contrast to MDT tubes) signal pile-up is the main reason for the degradation of the spatial resolution with increasing rate while space charge effects and gain reduction play a minor role.

The dependence of the average drift tube spatial resolution on the photon hit rate is shown in Figure 6.21. With the requirement $\Delta t > 600 \text{ ns}$, the spatial resolution degrades from $110 \mu\text{m}$ at zero rate to approximately $150 \mu\text{m}$ at the highest rate of 1500 kHz per tube. Without this requirement, the spatial resolution degrades to approximately $195 \mu\text{m}$ at 1500 kHz per tube.

The degradation of the spatial resolution due to signal pile-up can partially be recovered with additional corrections using time and charge information of the preceding background hits as is shown in the following.

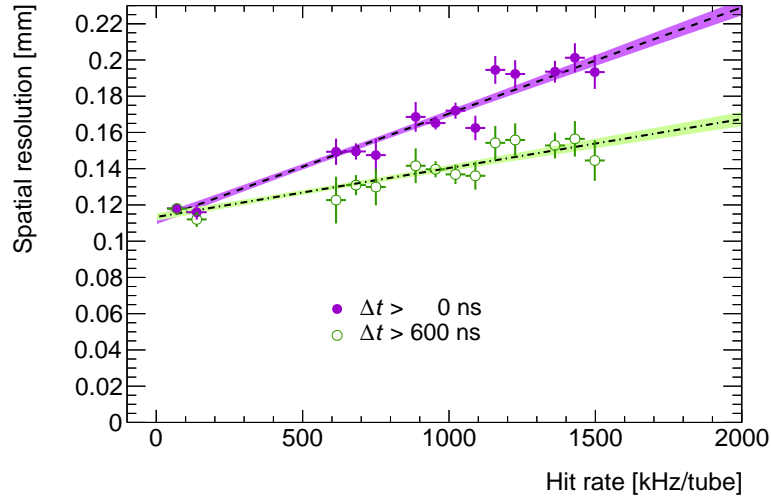


Figure 6.21: Average sMDT drift tube resolution with time slewing and multiple scattering corrections as a function of the hit rate with and without requirement on the minimum time interval Δt between successive hits. Straight lines are fitted to the data points with the 68% confidence intervals of the fit indicated.

Additional Time Slewing Correction Under Irradiation

The time slewing correction described in section 6.4.2 is applied to all drift tubes in the reference tracking part and in the analysis part of the chamber. Due to the drop of the gas amplification caused by the irradiation and the voltage drop in the noise filters discussed above, the signal pulse amplitudes and the measured charge values decrease with increasing rate. Figure 6.22 shows the dependence of the track residuals on the rising edge charge Q measured by the Wilkinson ADC in intervals of the impact radius r_{track} for all drift tubes in the analysis part under irradiation. Despite the already applied standard time slewing correction, a correlation is found that is strongest for small r_{track} . This can be explained by the dependence of the rising edge charge on r_{track} (cf. Figure 4.2) as time slewing is more pronounced for small pulses.

An additional time slewing correction for the irradiated tubes subtracted from the measured drift radius

$$r \rightarrow r - l_i(Q),$$

is obtained by parametrising the dependence of the track residuals on the rising edge charge with straight lines $l_i(Q)$ in intervals $r_i < r_{\text{track}} < r_{i+1}$. After applying this correction, the charge dependence is eliminated (cf. Figure A.1) and the average spatial resolution improves by approximately 10 μm (see Figure 6.24).

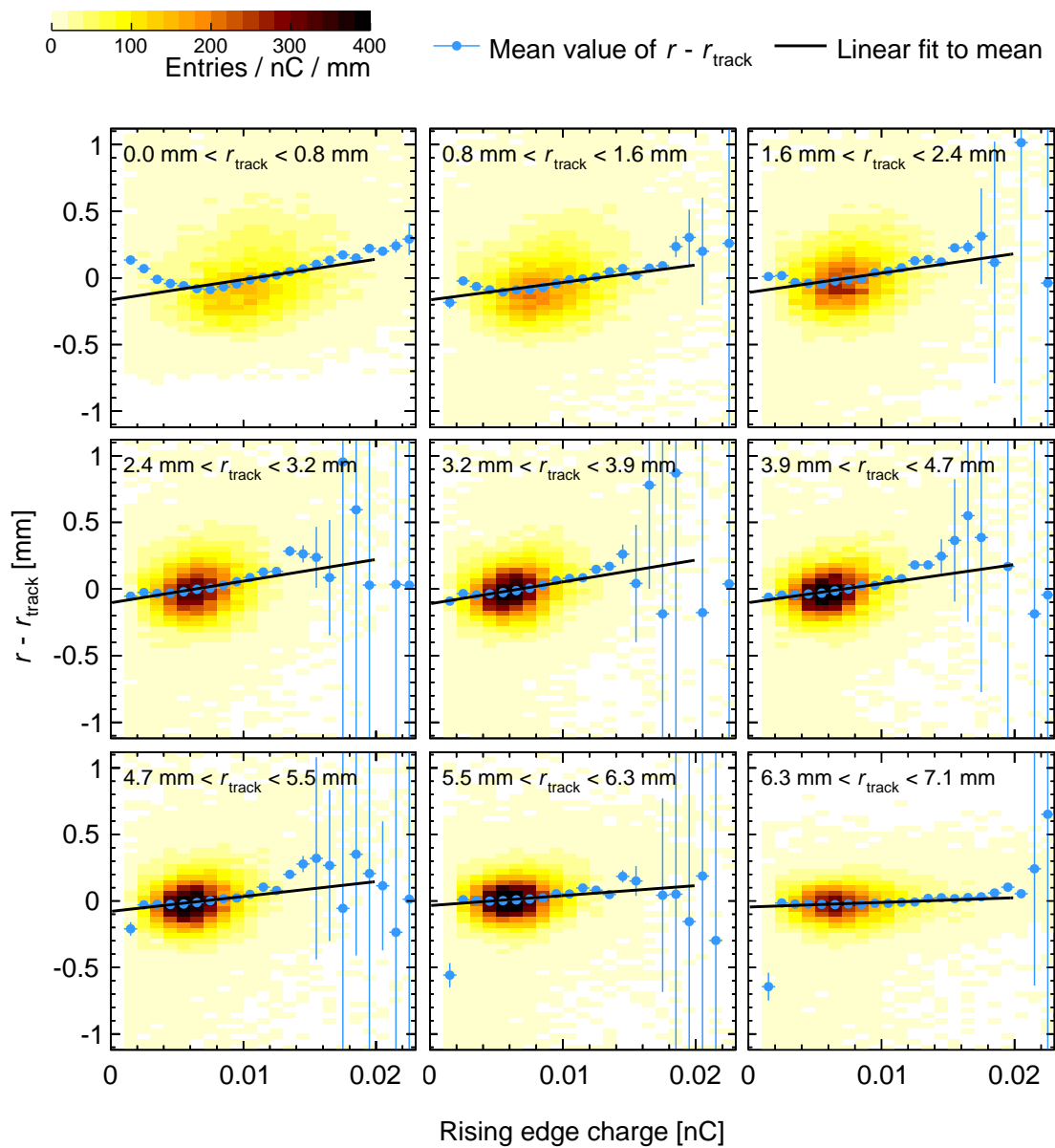


Figure 6.22: Dependence of the track residuals on the rising edge charge measured by the Wilkinson ADC with an integration gate of 18.5 ns in bins of the impact radius r_{track} for all irradiated tubes. The blue dots indicate the mean values of the residual distribution in the bins of the charge. The error bars correspond to the charge bin width and to the RMS of the residual distributions, respectively. Linear fits to the mean values are shown as a black lines.

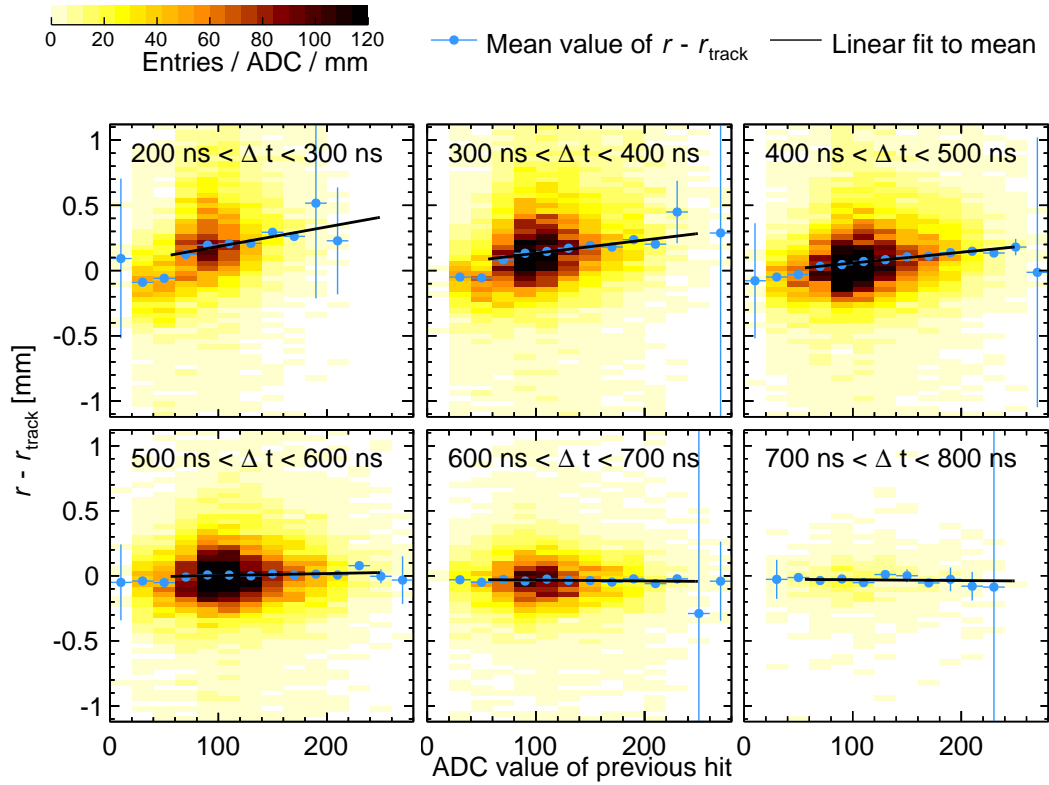


Figure 6.23: Dependence of the residuals on the ADC counts of the preceding hit in sections of the time elapsed since the preceding hit. Black markers indicate the mean values of the residual distribution in bins of the ADC counts. The error markers correspond to the bin width and the RMS in the horizontal and vertical direction, respectively. A linear fit to the mean values in the range 60 to 240 ADC counts is shown as a black line.

Pile-Up Correction

As mentioned above, the main effect of the degradation of the spatial resolution is due to signal pile-up described in section 3.4.3. For muon signals superimposed on the undershoot of a preceding background signal, the baseline is effectively shifted, with the amount of shifting depending on the time elapsed since the previous pulse and the shape of signal and corresponding undershoot.

Figure 6.23 shows the dependence of the track residuals on the rising edge charge of the preceding hit Q_{prev} in intervals of the time Δt elapsed since the preceding hit with the additional time slewing correction described above already applied. A strong correlation is found in the range $200 \text{ ns} < \Delta t < 500 \text{ ns}$ increasing with decreasing Δt where pile-up effects become larger (cf. Figure 3.14).

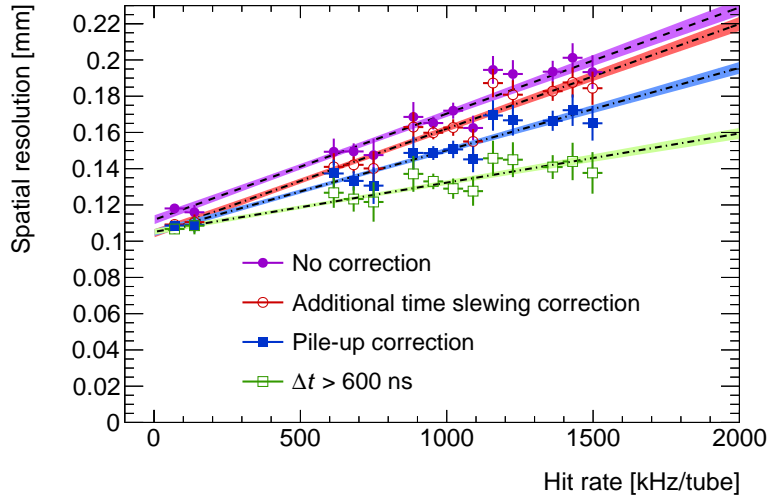


Figure 6.24: Average spatial resolution of all drift tubes in the analysis region as a function of the hit rate before and after applying additional corrections. The purple circles and green open squares are the same as in Figure 6.21. Applying the additional time slewing correction and in addition the pile-up correction (see text) results in the red open circles and the blue full squares, respectively. Straight lines are fitted to the data points with error bands indicating the 68 % confidence intervals of the fits.

As for the additional time slewing correction, a correction is performed by parametrising the track residual dependence on the rising edge charge of the previous hit with straight lines $l_j(Q_{\text{prev}})$ in intervals $\Delta t_j < \Delta t < \Delta t_{j+1}$ which is subtracted from the measured drift radius:

$$r \rightarrow r - l_j(Q_{\text{prev}}).$$

The residual distributions as a function of Q_{prev} after applying the correction function are shown in Figure A.2. The pile-up correction improves the average spatial resolution by approximately $20 \mu\text{m}$ at the highest observed rates of 1500 kHz per tube.

Figure 6.24 summarises the improvements with additional time slewing and signal pile-up corrections. With both together, the spatial resolution improves at the highest observed photon hit rate of 1500 kHz per tube from $195 \mu\text{m}$ to $170 \mu\text{m}$, while the requirement $\Delta t > 600 \text{ ns}$, which is equivalent to operation with an electronics dead time of 600 ns, with which much less signal pile-up effect is expected, improves the resolution to $150 \mu\text{m}$. High dead time, however, reduces significantly the muon efficiency (see next section).

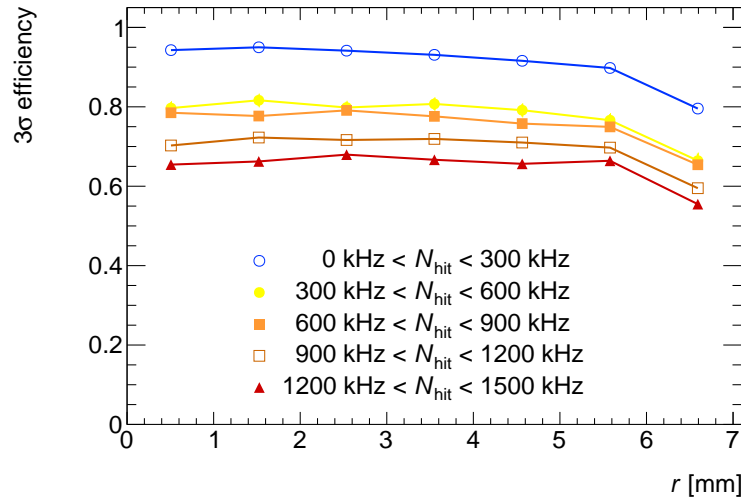


Figure 6.25: 3σ -efficiency as a function of the drift radius r in different intervals of the hit rate.

6.5.3 Muon Efficiency

Like the spatial resolution, the muon efficiency degrades in the presence of radiation background as discussed in chapter 3. Figure 6.25 shows the radial dependence of the 3σ -efficiency (cf. section 4.5) for different ranges of hit rates. The slight decrease of the 3σ -efficiency with increasing drift radius is caused by δ -electrons, the drop close to the tube wall is caused by the shortening of the ionisation path as described in section 2.2.3.

Figure 6.26 shows the average 3σ -efficiency as a function of the photon hit rate. The expected degradation due to masking of hits for an electronics dead time of 220 ns according to equation (3.4) is indicated by the dashed blue line. The measured 3σ -efficiency is significantly lower at high rates and can be described with an effective dead time of 337 ns.

The main reason for the longer effective dead time describing the data is loss of secondary hits due to signal pile-up (see chapter 8 and [68]) and, in addition at very high rates, the loss in detection efficiency due to reduced gas gain.

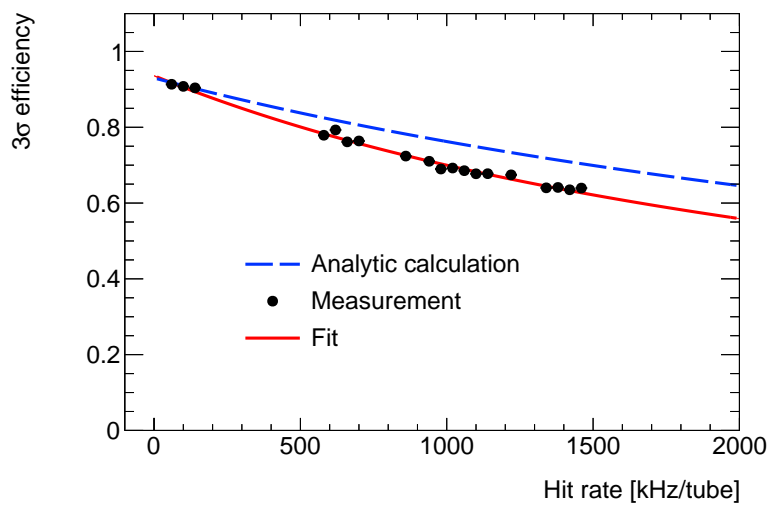


Figure 6.26: Average 3σ -efficiency as a function of the hit rate. The dashed blue line shows the expectation according to equation (3.4) with $t_{\text{dead}} = 220$ ns and $\varepsilon_0 = 0.94$. The solid red line is a fit of equation (3.4) to the data points with free parameters t_{dead} and ε_0 resulting in $t_{\text{dead}} = (337 \pm 3)$ ns and $\varepsilon_0 = 0.936 \pm 0.001$.

7

sMDT Chambers Under Proton Irradiation

7.1 Introduction

Up to 10 % of the background hits in the ATLAS MDT chambers are caused by protons and other charged hadrons [46]. Despite the relatively small contribution, these hits need special attention because they deposit large amounts of charge in the detector increasing the space charge densities and affecting the functionality of the front-end electronics.

In this chapter, irradiation tests of a custom designed sMDT chamber in a narrow high intensity proton beam are discussed. The measurements were carried out at the Tandem-van-de-Graaff accelerator at the Maier-Leibnitz Laboratory in Garching [69]. The sMDT chamber was irradiated with a beam of protons of 20 MeV energy which on average deposit about four times as much ionisation charge in the drift tubes as the 662 keV photons at the GIF. This allows for performance studies of sMDT tubes at space charge densities much higher than can be reached with photon irradiation at the GIF. The study is also relevant for the evaluation of the effects of the similarly high neutron background component which produces even larger signals in the drift tubes. In addition to the measurements of spatial resolution and efficiency as a function of the proton irradiation rate, the drop of the gas amplification due to space charge was studied.

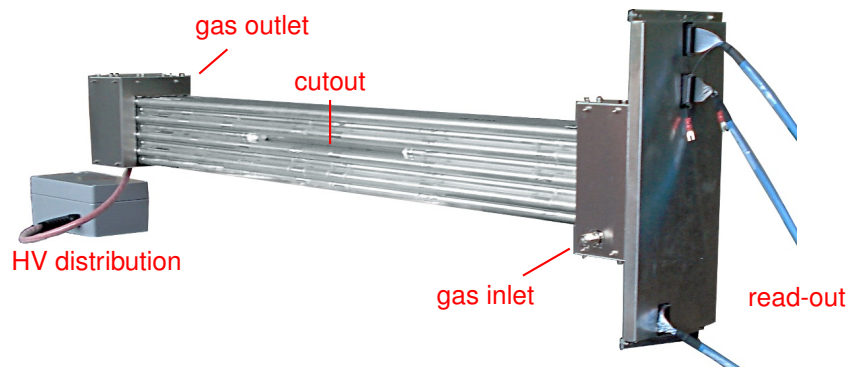


Figure 7.1: The custom designed sMDT chamber used for the measurements under proton irradiation. The drift tube length is 95 cm.

The data were recorded in two periods — in April and May 2011 and in October 2012. For the measurements in 2011 the maximum dead time setting of the ASD chip was used, in 2012 the minimum dead time. The experimental setup and the other operating parameters of the sMDT chamber were the same in both periods.

7.2 Experimental Setup

A photograph of the custom designed sMDT chamber is shown in Figure 7.1. It has all features of the prototype chamber (see section 2.3.2) but consists of only one multilayer with 8 tube layers and 6 tubes per layer. Like in the setup used for the measurements under photon irradiation in the previous chapter, the sMDT chamber serves both as test device and as tracking reference for cosmic ray muons.

Only the centre of the fourth tube layer from top is irradiated by the 3 mm diameter proton beam over a width of 7 cm along the tubes swept out with a frequency of 300 to 980 Hz (see Table 7.1. Simulation with the SRIM software* showed that most protons are stopped in the aluminium tube wall after having traversed three drift tubes [70]. Therefore, two tubes were left out in the irradiated tube layer such that the drift tubes experiencing the highest proton rate are located in the centre of the chamber with best angular coverage for the tracking of cosmic ray muons (cf. Figure 7.4). Each of the four remaining drift tubes in the irradiated layer were connected to individual high-voltage channels with voltage and current monitoring. The four tubes were also connected to a separate mezzanine board in order to avoid saturation of the TDC buffer.

*<http://www.srim.org>

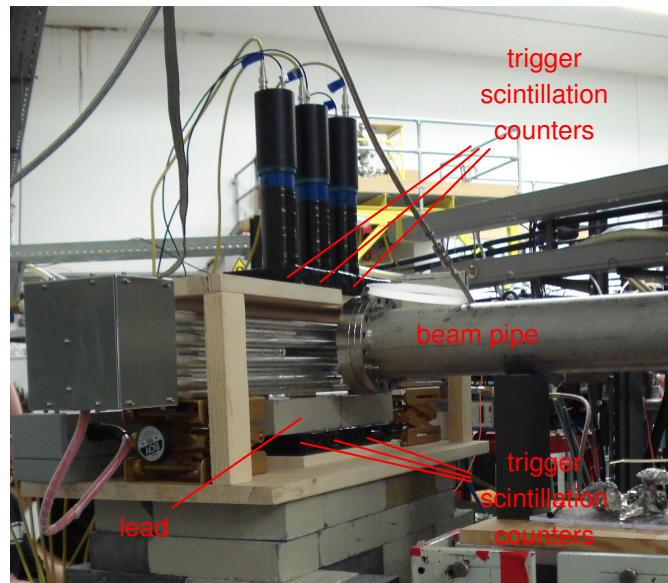


Figure 7.2: Photograph of the experimental setup at the Tandem-van-de-Graaff accelerator with the sMDT chamber, the trigger scintillation counters, lead shielding and the beam pipe.

Two layers of scintillation counters above and below the sMDT chamber were used to trigger on cosmic ray muons (cf. Figures 7.2 and 7.3). For a trigger, at least one hit in each layer was required. A 5 cm thick layer of lead above the bottom scintillation counter layer stops muons with less than 200 MeV energy reducing the influence of multiple scattering on the resolution measurement. Each scintillator layer was segmented into three counters in tube direction with the two middle ones matching the region of the sMDT chamber irradiated by the proton beam. The segmentation of the scintillation counters allows for offline discrimination between muon tracks traversing the irradiated and the unirradiated regions of the sMDT chamber (cf. Figure 7.3). In this way, space charge effects can be distinguished from pure counting rate effects.

7.3 Irradiation Conditions

Homogeneous irradiation of the drift tubes in a defined region is necessary for meaningful measurements. The optimum would be a wide beam spot with a height just small enough not to irradiate the tracking reference drift tubes. The maximum technically possible beam spot width is about 20 to 30 mm (for details see Table 7.1), which is too small for a sufficiently high rate of muon tracks traversing the irradiated region. Therefore, the beam was periodically moved in horizontal direction by means of a wobbler magnet sweeping the drift tube layer over a length of 7 cm corresponding to the width of the beam pipe exit window.

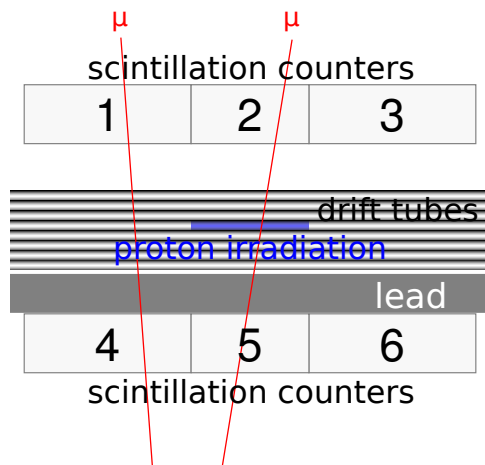


Figure 7.3: Schematic view of the setup perpendicular to the beam direction. A $3 \text{ mm} \times 7 \text{ cm}$ wide band around the sense wire in the blue region cut out from the tube layer is illuminated by the proton beam. The segmentation of the trigger scintillation counters allows for discrimination of cosmic muon tracks traversing the irradiated region (hits in scintillators $1 \wedge 6$, $2 \wedge 5$ and $3 \wedge 4$) from muon tracks traversing the non irradiated regions (hits in scintillators $1 \wedge 4$ and $3 \wedge 6$). The width of the irradiated region along the drift tubes (blue) is 7 cm.

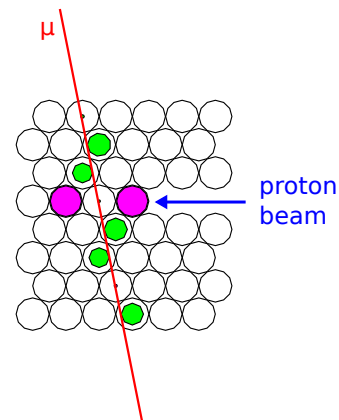


Figure 7.4: Cross sectional view of the custom designed sMDT chamber with a reconstructed muon track shown in red. The measured drift radii are indicated as full green circles, while tubes with out-of-time hits from proton hits uncorrelated with the cosmic muon trigger are coloured in violet.

Table 7.1: Irradiation conditions of the first tube in the analyzed runs. The hit rates quoted are calculated as described in section 7.5.1. The currents are the average values during the runs.

Start date	Hit rate of 1 st tube [kHz]	Current of 1 st tube [nA]	Wobbler frequency [Hz]	Beam spot width [mm]
2011/04/28 20:02	0 ± 0	0.0	—	—
2011/05/04 03:41	0 ± 0	0.0	—	—
2011/04/29 20:54	97 ± 10	50.5	300	10.0
2011/05/03 18:34	184 ± 12	95.0	980	33.0
2011/05/05 00:05	185 ± 9	100.5	880	17.5
2011/05/05 19:22	188 ± 9	95.1	880	17.5
2011/04/30 09:12	928 ± 24	206.4	300	10.0
2011/04/30 00:59	917 ± 47	206.7	300	10.0
2011/05/03 00:38	1463 ± 84	270.1	300	10.0
2012/10/03 23:46	0 ± 0	0.0	—	—
2012/10/10 00:20	23 ± 2	14.6	630	20.0
2012/10/06 15:41	48 ± 2	32.8	630	20.0
2012/10/07 20:08	95 ± 3	56.5	630	20.0
2012/10/05 00:15	137 ± 4	69.4	630	20.0
2012/10/05 23:40	149 ± 4	57.4	630	20.0
2012/10/08 19:20	194 ± 3	93.3	630	20.0
2012/10/09 20:59	311 ± 13	113.3	630	20.0
2012/10/08 10:44	1459 ± 56	241.0	630	20.0
2012/10/08 14:35	2553 ± 152	332.5	630	20.0

To generate uniform space charge along the drift tubes, the wobbler cycle needs to be shorter than the typical ion drift time from the avalanche region close to the wire to the tube wall (cf. section 2.2) which for sMDT drift tubes is approximately 1 ms. Thus, a wobbler frequency of >1 kHz is desirable. The wobbler frequencies achieved were somewhat smaller and are given in Table 7.1. The beam spot size in vertical direction had to be narrow enough to avoid high rates in the adjacent reference drift tubes and varied between 1 and 3 mm.

According to the SRIM simulation [70], the energy loss of 20 MeV protons in the first and second drift tube is independent of the penetration depth around 11 keV/mm and 15 keV/mm, respectively. In the third tube, the energy loss increases strongly with the depth and is very sensitive to geometrical changes like for instance the elevation of the chamber with respect to the beam which defines the amount of aluminium the protons pass. As this is not well under control, only the first two tubes are considered in the analysis.

7.4 Drop of the Gas Amplification

The gas gain drop can be determined using the prediction by Diethorn's equation (cf. section 3.3.1) for the gas amplification if the primary ionisation is known. There are, however, several reasons why one cannot rely on the prediction:

- The prediction of Diethorn's equation may not be reliable for very high space charge densities as in the present case.
- The wobbler frequency is at the limit of what is necessary to achieve uniform space charge densities. This increases the uncertainty of the prediction which assumes uniform irradiation.
- The vertical beam profile was much smaller than the drift tube diameter leading to non-uniform illumination of the drift tubes. One has to assume that the charge multiplication avalanche spreads around the full wire circumference and the resulting space charge distribution is isotropic and independent of the exact position of the incident proton beam.

Therefore, a reliable measurement of the space charge density and, therefore, of the gas amplification is desirable. Two methods are available for the measurement.

Measurement by Means of the Rising Edge Charge: This method was already applied in the previous chapter. It utilises the charge measurement of the Wilkinson ADC of the ASD chip. The method allows for measuring the effective gas gain experienced by muon tracks by selecting only charge measurements associated to a reconstructed track. The amount of gain drop experienced by muons is different from the gain drop experienced by the protons if the proton irradiation is non-uniform and, thus, provides a way to probe the uniformity of the irradiation. The ratio between the rising edge charges of muon signals measured when the chamber is irradiated (q) and when it is not irradiated (q_0) is directly proportional to the relative gas amplification under irradiation. Figure 7.6 shows the relative gas amplification $G/G_0 = q/q_0$ as a function of the proton rate. In addition, predictions based on Diethorn's equation assuming an average primary ionisation charge of $Q_{\text{prim}}^p = 5800 e$ per proton from SRIM simulation [70] for three different hypotheses about the irradiation distribution are shown. For the predictions, the total proton rate is uniformly spread over 100 %, 50 % and 60 % of the total tube cross section (see Figure 7.5). Under the assumption of uniform irradiation of the full drift tube cross section a much higher gain drop is predicted compared to the measured values. This suggests that the wobbler frequency is too low to achieve uniform space charge distribution. The measured behaviour is well described by the 60 % illumination hypothesis.

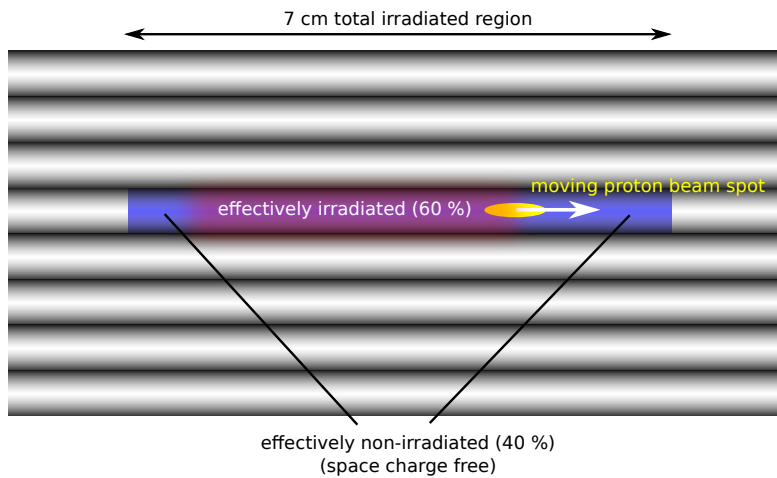


Figure 7.5: Illustration of the non-uniform irradiation in the Tandem measurements due to limited wobbler frequency.

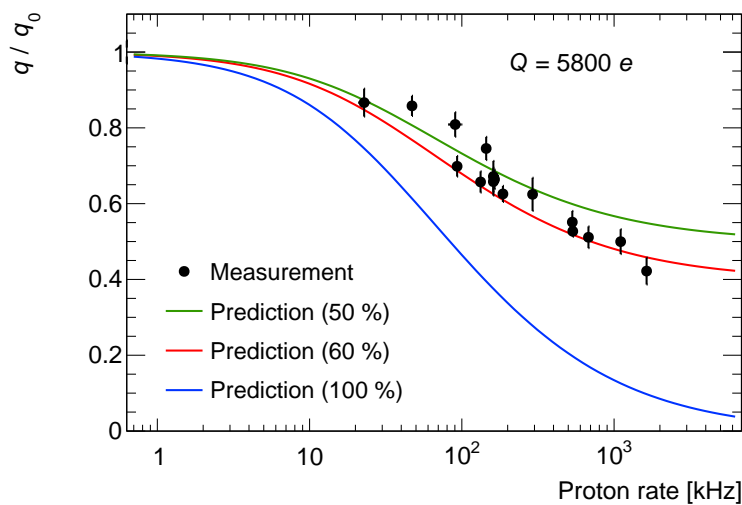


Figure 7.6: Dependence of the relative gas amplification $G/G_0 = q/q_0$ on the proton irradiation rate. The green/red/blue line shows the predicted behaviour using Diethorn's equation from section 3.3.1 assuming that 50%/60%/100% of the drift tube cross section are uniformly illuminated while the remaining 50%/40%/0% are free of space charge.

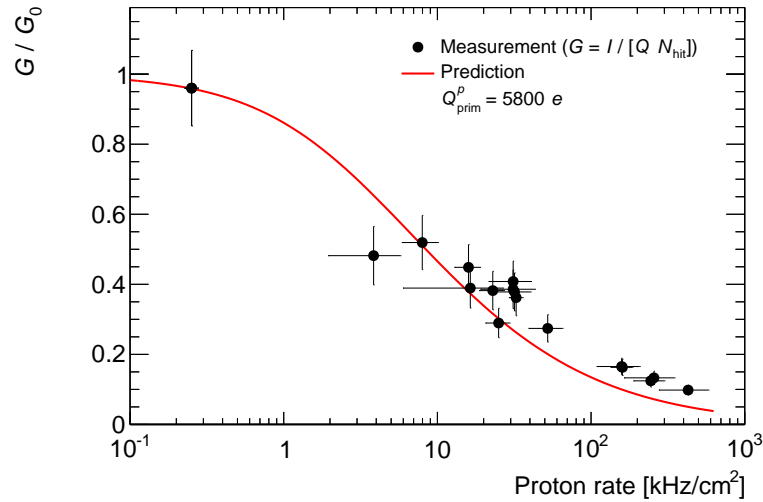


Figure 7.7: Dependence of the relative gas amplification G/G_0 on the proton flux assuming uniform illumination over 60 % of the tube cross section.

Measurement by Means of the Current: The second method utilises the current monitoring of the drift tube high-voltage supply. With the knowledge of the proton rate and primary ionisation, one can use equation (4.4) to calculate the gas amplification. Figure 7.7 shows the measurement for the first drift tube in the proton beam and the prediction from Diethorn's equation for an ionisation charge $Q_{\text{prim}}^p = 5800 e$ per proton and the same assumption as above, that the proton irradiation is concentrated effectively on 60 % of the drift tube cross section while 40 % remain unirradiated. According to the SRIM simulation, the protons lose about $150 \text{ keV} = 11 \text{ keV/mm} \cdot 14.2 \text{ mm}$ of energy due to ionisation in the centre of the first drift tube. Measurement and prediction are in good agreement under the aforementioned assumptions.

The gain drop measurements can be used to discriminate between space charge effects and counting rate effects and is used in the simulations described in chapter 8.

7.5 Data Analysis

7.5.1 Proton Rate

The proton hit rate is determined as described in section 4.1. In addition to the hit rates measured with the sMDT tubes, the proton rate was measured with a scintillation counter mounted instead of the sMDT chamber in the same place every time the beam current was changed. Figure 7.8 shows the correlation between the scintillation counter hit rates and the sMDT rates with and without dead time correction. The dead time corrected hit rates agree well with the scintillation

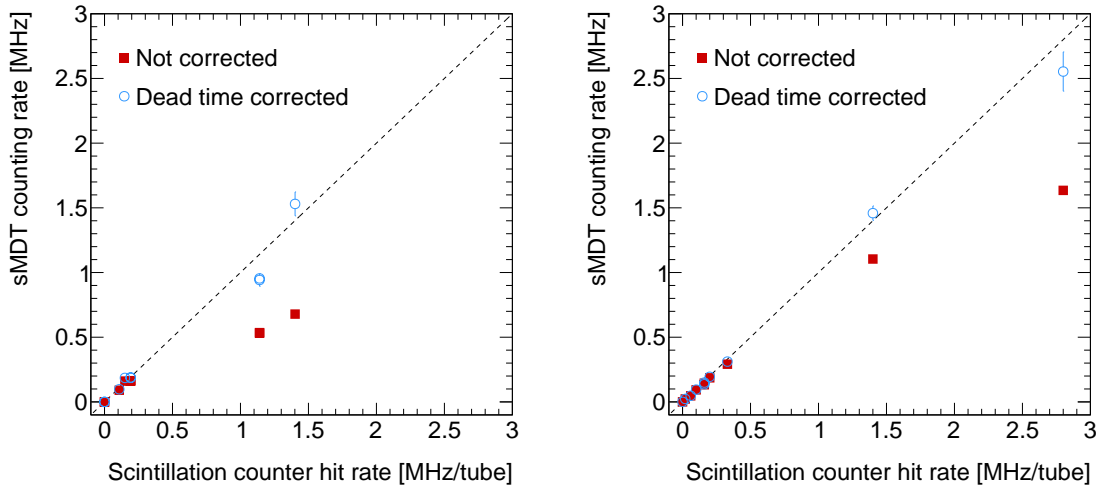


Figure 7.8: Correlation between the sMDT counting rates with and without dead time correction and the reference measurement with a scintillation counter for (left) maximum and (right) minimum dead time setting.

counter hit rates and are used in the following. The loss in sMDT counting rate at high proton beam intensities due to electronics dead time is clearly visible.

7.5.2 Spatial Resolution and Efficiency

The general procedure of the measurement of the spatial resolution is described in section 4.4. In the present case, an additional correction for multiple scattering is applied. As the measurements are performed with cosmic ray muons with low energies starting from about 200 MeV after passing the lead layer, the contribution of multiple scattering in the tube walls to the spatial resolution cannot be neglected. Simulation of the setup with the MTGEANT-4 program [37] shows that multiple scattering contributes with about $\sigma_{\text{MS}} = 60 \mu\text{m}$ quadratically to the measured spatial resolution σ_{meas} in the irradiated tube layer. The energies of muons from interesting physics processes at the LHC are in the range from few GeV up to the TeV scale where multiple scattering within the drift tube walls is negligible. Therefore, the contribution of multiple scattering is subtracted quadratically from the measured resolution:

$$\sigma_{\text{tube}} = \sqrt{\sigma_{\text{meas}}^2 - \sigma_{\text{MS}}^2}.$$

The 3σ -efficiency is determined as in section 4.5 using the with σ of the residual distribution without correction for the muon track extrapolation uncertainty or multiple scattering.

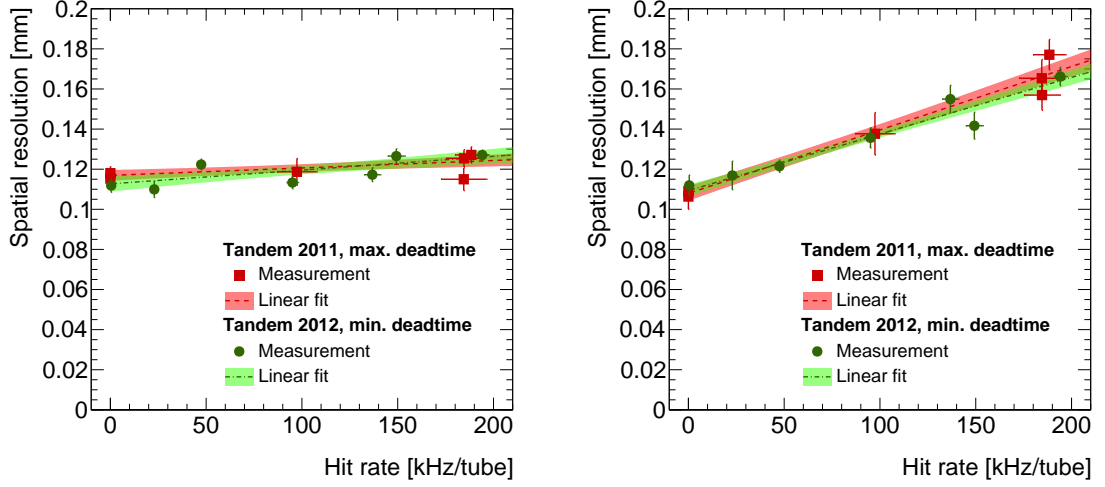


Figure 7.9: Dependence of the spatial resolution on the hit rate in the (left) unirradiated and (right) irradiated regions. The data with proton rates >200 kHz are not used in the resolution measurement because the statistics are too low leading to very large uncertainties.

7.6 Results

The degradation of the spatial resolution in the unirradiated regions of the illuminated tubes should be very small as the average time difference between two hits is large compared to the baseline restoration time t_{blr} . The fraction of pile-up muons on top of a background hit subject to signal pile-up with $t_{\text{dead}} < t < t_{\text{blr}}$ at the background rate N is

$$\int_{t_{\text{dead}}}^{t_{\text{blr}}} N \cdot e^{-N \cdot t} dt = e^{-N \cdot t_{\text{dead}}} - e^{-N \cdot t_{\text{blr}}},$$

which is about 7% at $N = 200$ kHz per tube for the minimum dead time $t_{\text{dead}}^{\text{min}} \approx 220$ ns used in the 2012 measurements and 0 for the maximum dead time $t_{\text{dead}}^{\text{max}} \approx 820$ ns used in the 2011 measurements which is larger than the baseline restoration time $t_{\text{blr}} \approx 600$ ns (cf. section 3.4.3).

Figure 7.9 shows the measured average spatial resolution as a function of the hit rate for both measurement periods in the unirradiated and irradiated regions. There is almost no dependence on the hit rate in the unirradiated region. In the irradiated region, there is a clear deterioration of the spatial resolution due to space charge effects from $110 \mu\text{m}$ in the absence of irradiation to $170 \mu\text{m}$ at the highest hit rate of about 190 kHz per tube. In both regions, there is no effect of the different dead times visible. Signal pile-up effects do not depend on the region and are still small for rates up to 200 kHz (see above and chapter 8).

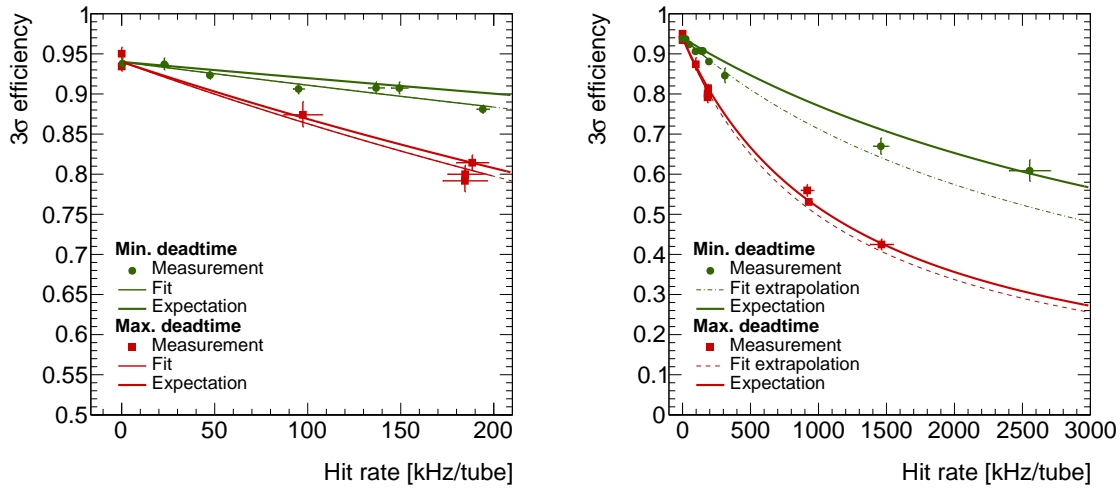


Figure 7.10: Dependence of the 3σ -efficiency on the hit rate in the unirradiated regions. The expectations from masking of hits by preceding background hits during the minimum and maximum dead times of $t_{\text{dead}}^{\text{min}} = 220$ ns and $t_{\text{dead}}^{\text{max}} = 820$ ns, respectively, according to equation (3.4) are shown as solid lines. In addition, equation (3.4) is fitted to the data points in the range 0 to 200 kHz with the dead time as a free parameter. The right plot shows additional data points at very high rates not included in the fit and the extrapolation of the fit from the left plot. The error bands indicate the 68 % confidence intervals of the fits.

Figure 7.10 shows the measured 3σ -efficiency in the unirradiated regions of the illuminated tubes. The efficiency degrades due to masking of muon hits by preceding background hits during the dead time as described by equation (3.4) with an additional fraction $\varepsilon_0 = 0.94$ to account for the rate-independent efficiency loss due to δ -electrons from muon hits (cf. section 2.2.3). The predictions for minimum and maximum dead time of $t_{\text{dead}}^{\text{min}} = 220$ ns and $t_{\text{dead}}^{\text{min}} = 820$ ns, respectively, are shown as solid lines. In addition, the fits of equation (3.4) to the data with the dead time as free parameter are shown with the results $t_{\text{dead}}^{\text{min}} = (319 \pm 24)$ ns and $t_{\text{dead}}^{\text{max}} = (893 \pm 54)$ ns. The measurements agree well with the expectation for the maximum dead time, while for the minimum dead time the observed efficiency is lower than expected and consistent with the value measured under photon irradiation of (337 ± 3) ns (cf. section 6.5.3). The additional degradation can be attributed to signal pile-up as shown by simulation in chapter 8.

An indication of signal pile-up comes also from the data point at the the highest rate of 2500 kHz per tube which agrees with the expectation. At such high proton irradiation, the gas amplification for proton hits drops below 20 % of the nominal value (cf. Figure 7.7), resulting in smaller signal amplitudes and, therefore, less signal pile-up. This behaviour is an artefact of the non-uniform irradiation and does not lead to a muon efficiency gain in case of uniform irradiation.

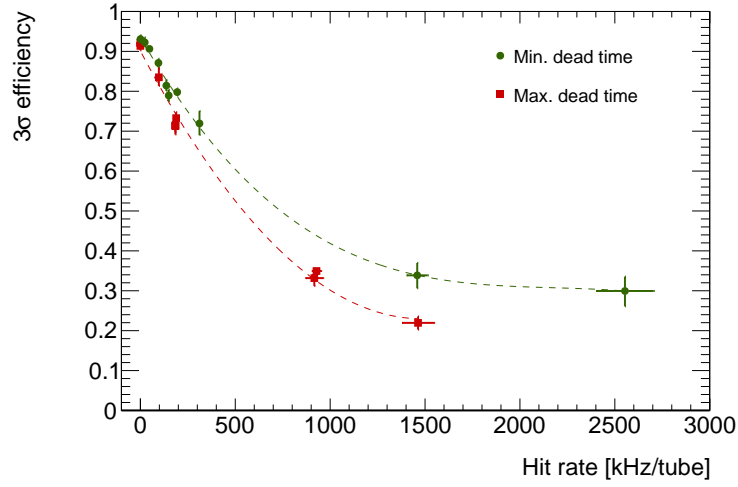


Figure 7.11: Dependence of the 3σ -efficiency on the hit rate in the irradiated region. The dashed lines are shown to guide the eye.

Figure 7.11 shows the dependence of the 3σ -efficiency on the hit rate in the irradiated region of the chamber where space charge effects and gain drop cause additional degradation of the efficiency. The measured total efficiency can be described by a rate independent part ε_0 accounting for efficiency loss due to δ -electrons and the efficiency loss close to the tube wall (cf. section 2.2.3), a hit rate dependent part $\varepsilon_{\text{elx}}(R)$ due to read-out electronics dead time and signal pile-up effects, and a space charge dependent part $\varepsilon_{\text{sc}}(G)$ accounting for efficiency loss due to loss of gas amplification:

$$\varepsilon_{\text{total}}(R, G) = \varepsilon_0 \cdot \varepsilon_{\text{elx}}(R) \cdot \varepsilon_{\text{sc}}(G).$$

Since $\varepsilon_{\text{sc}} = 1$ in the unirradiated regions, the space charge dependent contribution in the irradiated region is given by

$$\varepsilon_{\text{sc}}(G) = \frac{\varepsilon_{\text{total}}^{\text{irr}}}{\varepsilon_{\text{total}}^{\text{non-irr}}}. \quad (7.1)$$

The result is shown in Figure 7.12 as a function of the relative gas amplification G/G_0 measured for muon tracks (see Figure 7.6) and for protons (see Figure 7.7). In addition, the detection efficiency (cf. equation (4.11)) measured without background radiation in a muon beam is shown, where the gas amplification was reduced by lowering the wire potential.

From the good agreement of the G/G_0 dependence of the efficiency measured in the test beam and the one obtained under proton irradiation using the relative gas amplification measured for protons (G_p/G_0), one can conclude that the efficiency loss occurs in the strongly irradiated region of the non-uniform irradiated region. The behaviour is studied in more detail using simulations in

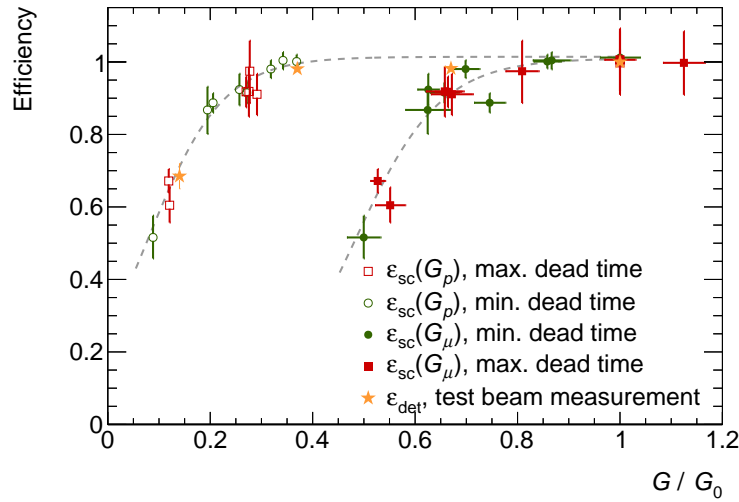


Figure 7.12: Dependence of the space charge dependent efficiency fraction on the relative gain drop measured for muons G_μ/G_0 (see Figure 7.6) and protons G_p/G_0 (see Figure 7.7). The specified efficiency is defined according to equation (7.1). In addition, the detection efficiency (cf. equation (4.11)) measured without background radiation in a muon beam is shown, where the gas amplification was reduced by lowering the wire potential. Dashed lines are drawn to guide the eye.

chapter 8. Looking at the G_p/G_0 dependence, the efficiency loss due to gain drop is less than 1 % as long as the loss of gas amplification is less than 60 %. For the photon dominated background in the ATLAS muon spectrometer, a drop of gas amplification by 30 % corresponds to photon rates of more than 20 kHz/cm² (cf. section 3.3.1), which is much higher than the maximum expected rates at HL-LHC even in the hottest regions of the ATLAS muon spectrometer.

8

Simulation of High-Rate Effects

8.1 Introduction

As observed in the previous chapters, signal pile-up is the main limitation of the performance of the sMDT tubes and contributes also to the performance loss of the MDT tubes when they are operated with the same short dead time as the sMDT tubes. For a quantitative understanding of this effect, detailed simulations on the analogue signal level have been performed which are discussed in this chapter. The spatial resolution of MDT and sMDT tubes in the absence of background radiation can be well described by simulation with the Garfield program [59] as has been shown previously [53, 71, 72]. It turns out, however, that the ion tail of the signal pulse, which is decisive for the pile-up effect, is not well modelled with existing methods. To avoid large systematic uncertainties due to this mismodelling, recorded real signals are used for the background description instead of simulated ones.

8.2 Simulation Chain

Muon signals in the drift tubes are simulated with the Garfield program and stored to disk. The simulation output contains the current $I(t)$ induced on the wire sampled in 1 ns time steps. The induced current is transformed into the amplitude arriving at the discriminator input by means of the transfer function of the amplification and shaping stages of the ASD chip [30].

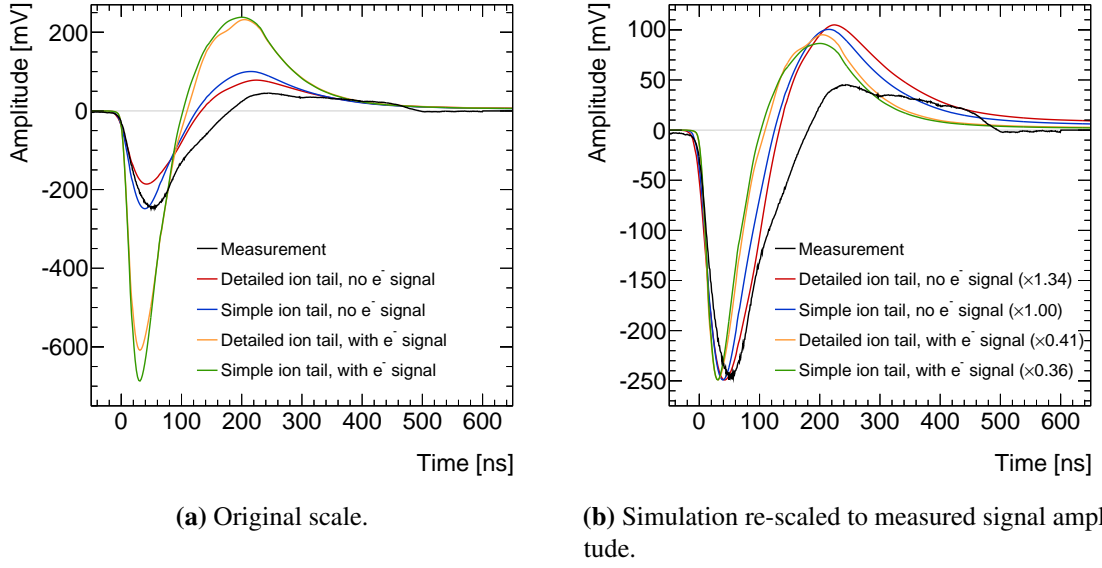


Figure 8.1: Average measured and simulated average muon signals in sMDT tubes after the amplifier and shaper stages of the ASD chip. Simulated signals are shown for two different models (detailed and simple ion tail) and each with and without the electron component.

Figure 8.1 shows averaged simulated muon signals in sMDT tubes using two different models for the ion tail after the application of the transfer function in comparison to the averaged measured muon signals. The difference between the two ion tail models is the start point of the ion trajectories. In the simple model, the ion trajectories start at the wire surface while in the detailed model they start from the average production radius in the avalanche. For both ion tail models, the signals are plotted with and without the electron component.

One observes significant differences in the amplitudes of the simulated signals (see Figure 8.1a) and rather poor agreement of the shapes of measured and simulated signals (see Figure 8.1b). Possible reasons for the disagreement, besides mismodelling by the Garfield program, are uncertainties in the gas amplification and the neglect of the transfer function of the drift tubes themselves.

The signals without the electron component match the measured signal amplitude much better. An attenuation of the electron component can be explained by the skin effect which increases the wire resistance for high frequency signals. The dependence of the wire resistance R on the angular frequency ω can be described by [73]

$$R(\omega) = \begin{cases} \frac{1}{\pi\sigma r_w^2} + \frac{\sigma\mu_0^2 r_w^2}{192\pi} \omega^2 & \text{for } \omega < \frac{8}{r_w^2 \sigma \mu_0} \\ \frac{1}{2\pi r_w} \sqrt{\frac{\mu_0 \omega}{2\sigma}} + \frac{1}{4\pi\sigma r_w^2} + \frac{3}{32\pi r_w^3} \sqrt{\frac{2}{\sigma^3 \mu_0 \omega}} & \text{for } \omega > \frac{8}{r_w^2 \sigma \mu_0} \end{cases}$$

where r_w is the wire radius and σ the electrical conductivity of the wire. For the W/Re anode wire used, which has a DC resistance of $44 \Omega/\text{m}$ [30], this means that frequencies beyond approximately 1 GHz are attenuated increasingly with the distance of the signal creation point from the read-out end. The electron component contains frequencies up to the THz domain and is thus strongly attenuated.

As the rising edge is well described by the simulation, simulated muon signals can be used to study the spatial resolution and efficiency. The amplitudes are, however, rescaled to the measurements (see Figure 8.1). The simulated signals can, however, not be used to describe the background pulses responsible for the signal pile-up effects which strongly depend on the late part ($t \gtrsim 200 \text{ ns}$) of the signal that is not well modelled. Therefore, recorded photon signals are used to simulate the pile-up effects.

The signal pile-up effects depend on the shape of the analogue signal arriving at the discriminator. Hence, the simulated muon signals are convolved with the response function of the analogue chain of the ASD chip. Events are built by superimposing the simulated muon signals with recorded photon signals arriving at a given rate λ . For uncorrelated background hits, the period Δt between two hits follows an exponential distribution:

$$\frac{dN}{d(\Delta t)} = \lambda \cdot e^{-\lambda \cdot \Delta t}. \quad (8.1)$$

Gain drop is taken into account by scaling all signals with the relative gas amplification G/G_0 determined for the given rate with the method based on Diethorn's equation described in section 3.3.1 (for photons see Figure 3.5).

After the signal and background signals have been combined, noise is added in each time bin according to a normal distribution with a width equal to $1/5$ of the discriminator threshold (-38 mV) according to noise measurements for MDT chambers [74]. Figure 8.2 shows two example events at this stage of the simulation. The simulated events are then scanned for discriminator threshold crossings and the threshold crossing times are analysed with the same methods as used for the measurements in the previous chapters to obtain the rate dependence of the spatial resolution and of the 3σ -efficiency.

8.2.1 Recorded Signals

Muon and photon signals have been recorded at the CERN Gamma Irradiation Facility (GIF) with an oscilloscope connected to the analogue output of one of the ASD channels with a coaxial cable with 50Ω impedance. The amplification of the signal by the analogue output driver in this configuration is $\alpha = 1/8$ according to the ASD user's manual [30]. Photon signals were recorded at the maximum photon flux with random triggers. An example is shown in Figure 8.3. The

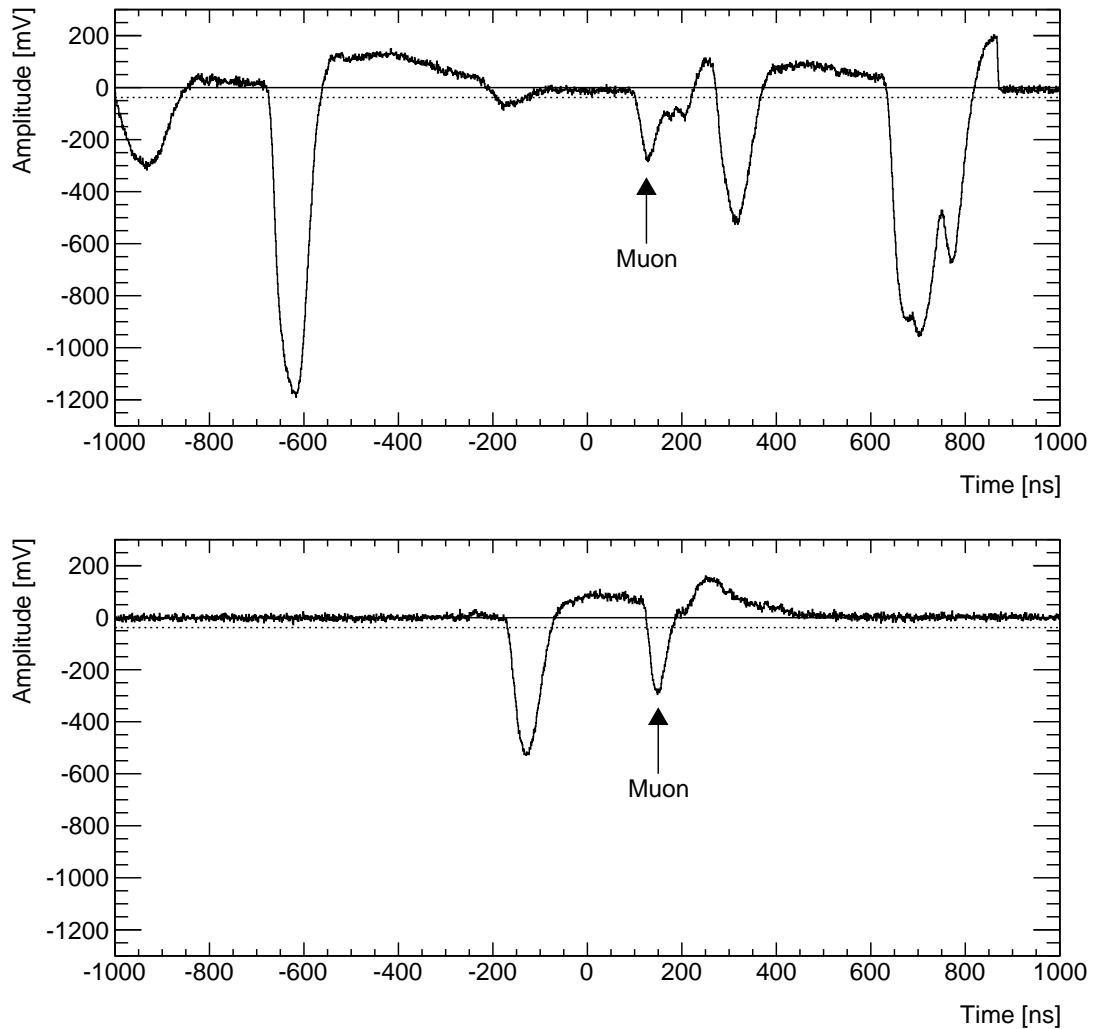


Figure 8.2: Two examples of simulated events in sMDT tubes with 1 kHz uncorrelated rate of 662 keV photons. The recorded background signals are added to the simulated muon signals according to an exponential distribution. The discriminator threshold of -38 mV is indicated with a dashed line.

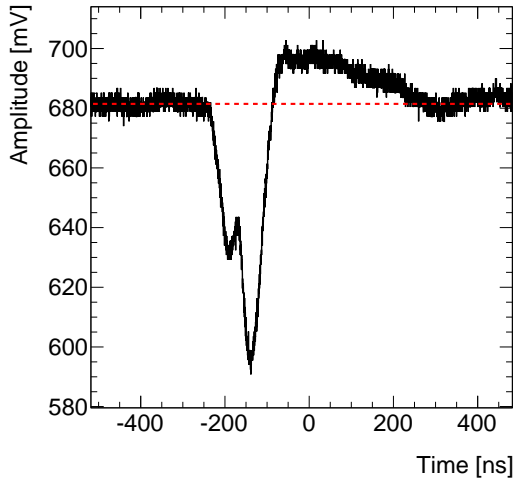


Figure 8.3: Raw recorded photon signal in a SMDT tube measured with an oscilloscope with $50\ \Omega$ termination at the analogue output of the ASD chip. The baseline at 681.5 mV is indicated as a red dashed line.

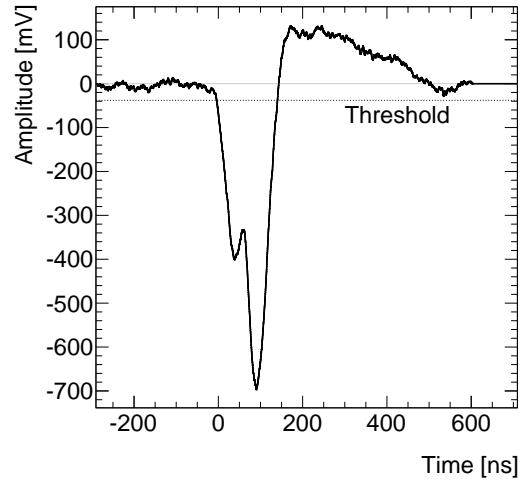


Figure 8.4: The signal shown on the left prepared as simulation input. Equations (8.2) and (8.3) have been applied to subtract the baseline, correct the scale and remove noise.

baseline, $a_0 = 681.5\ \text{mV}$, is subtracted from the raw signals and the amplification corrected for:

$$a(t) \rightarrow [a(t) - a_0] \frac{1}{\alpha}. \quad (8.2)$$

In order to remove noise from the signal, the simple moving average (SMA)

$$a_{\text{MA}}^{(n)}(t_i) = \frac{1}{n} \sum_{j=0}^{n-1} a(t_i - t_j) \quad (8.3)$$

is computed in each time bin i with the order $n = 20$, which is equivalent to applying a low-pass filter. The example signal from Figure 8.3 is shown in Figure 8.4 after the preparatory steps.

Figure 8.5 shows averaged recorded muon and photon signals. Photon signals have been recorded using random triggers at the maximum photon flux at the GIF, muon signals using the cosmic ray scintillator trigger with the photon source closed. While the average shapes of photon and muon signals are very similar, the amplitude of the average photon signal is approximately 2.5 times higher than the average muon signal. This is in good agreement with the expectation discussed below.

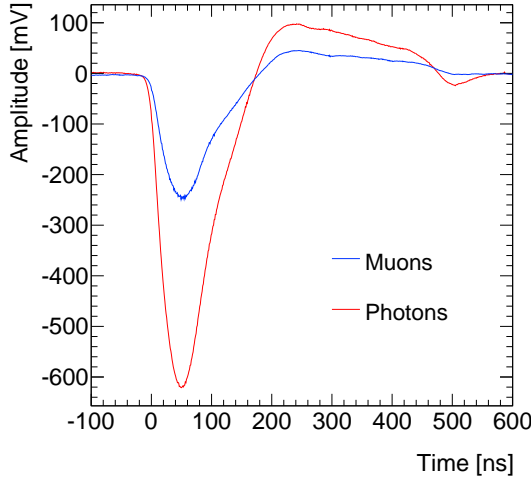


Figure 8.5: Comparison of averaged muon and photon signals recorded in sMDT tubes at the GIF. Muon signals were recorded using a cosmic ray scintillator trigger, photon signals using a random trigger at the maximum photon flux.

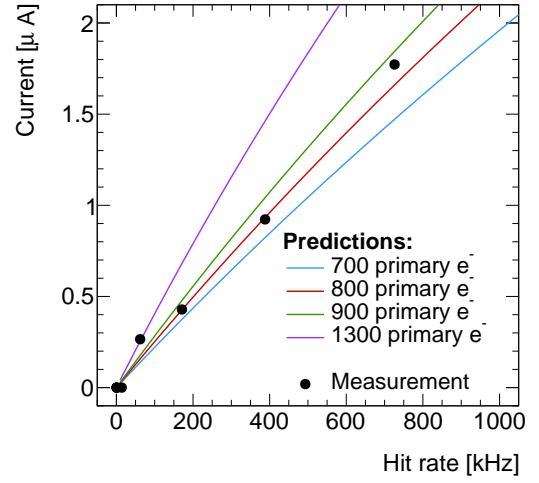


Figure 8.6: Dependence of the drift tube current on the photon hit rate compared to predictions based on Diethorn's formula (cf. section 3.3.1) for different numbers of primary ionisation electrons per converted photon.

For muons with a cluster density of 100 cm^{-1} , a cluster size of 3 (cf. section 2.2) and an average ionisation path length of

$$l = \frac{2}{R} \int_0^R \sqrt{R^2 - r^2} dr = \frac{\pi R}{2} \approx 11.2 \text{ mm}$$

for sMDT tubes with inner radius $R = 7.1 \text{ mm}$, on average 330 primary ionisation electrons are expected.

The average energy deposit per converted 662 keV photon in MDT tubes is 32 keV [71] to 36 keV [53] resulting in an average of 1300 primary ionisation electrons for the ionisation potential of 26 eV [71]. For sMDT tubes, the value is lower as can be seen from Figure 8.6 which shows the current measured in an sMDT tube under photon irradiation at the GIF in comparison with predictions obtained from equation (4.3) and Diethorn's equation (cf. section 3.3.1) for different numbers of primary ionisation electrons. The measurements match best with the predictions for 800 to 900 primary electrons. Numbers of primary electrons of 800 to 900 per converted photon and 330 per muon correspond well with the observed ratio of average photon to muon signal amplitudes of 2.5 (see Figure 8.5).

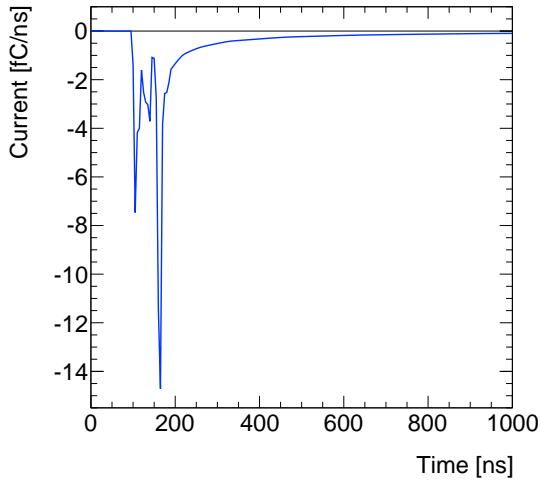


Figure 8.7: Example of the current induced on the anode wire of a by a muon hit from Garfield simulation in 1 ns time bins.

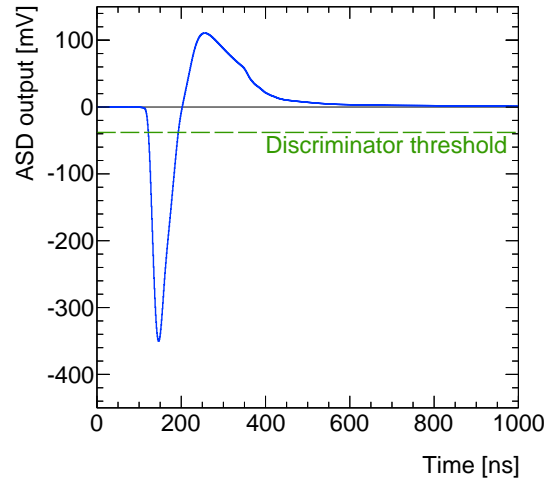


Figure 8.8: The signal from Figure 8.7 after convolution with the charge dependent response function of the ASD chip.

8.2.2 Electronics Response

As stated above, the Garfield simulation is used for the modelling of the muon signals, because no recorded signals with low noise and reference tracks were available. An example of the raw Garfield output, the current induced on the anode wire, is shown in Figure 8.7. In the linear regime, convolution of the drift tube signal with the response function of the analogue read-out chain gives the signal at the discriminator input (see Figure 8.8). As the amplification of the ASD is on purpose non-linear (cf. section 2.2.2 and Figure 2.10), extra effort is needed as described in the following.

In the linear regime of the ASD chip, the response is characterised by the transfer function f which in the time domain equals the response to a delta pulse. The signal $s(t)$ at the discriminator input is obtained by convolution of the raw drift tube signal $w(t)$ with the transfer function:

$$s(t) = (w * f)(t) = \int_{t_{\min}}^{t_{\max}} w(\tau) f(t - \tau) d\tau. \quad (8.4)$$

Figure 8.9 shows the response to 4 ns long delta-like pulses from measurement and from simulation of the ASD chip. The agreement is good except for the ringing in the undershoot caused by imperfect termination of the analogue output. For this reason, the simulated response is used in the following.

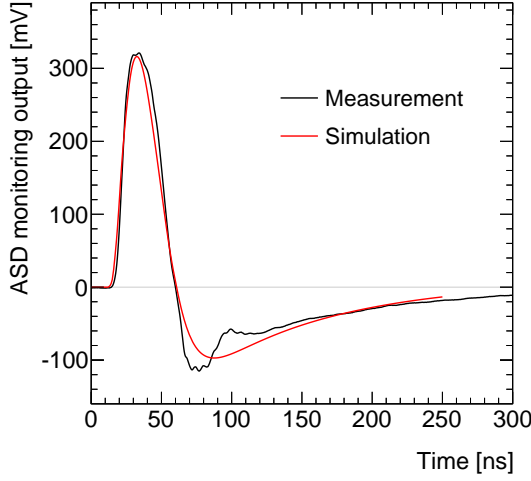


Figure 8.9: Measured and simulated analogue response of the ASD chip to 4 ns long delta-like input pulses. The polarity is opposite to the (negative) drift tube signals previously shown.

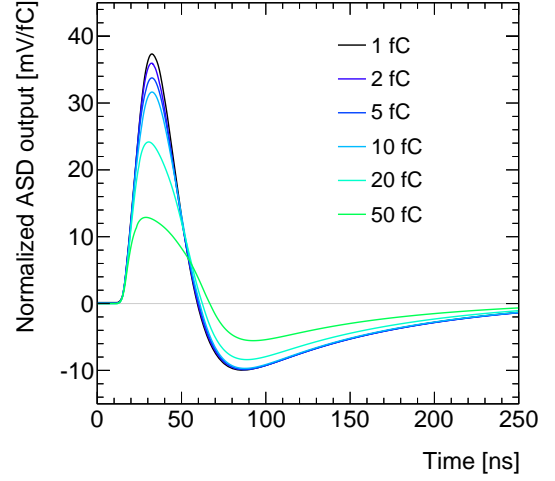


Figure 8.10: Simulated analogue response of the ASD chip to 4 ns long rectangular delta-like pulses for different integral signal charges normalised to 1 fC input charge.

To account for the non-linear response, different delta response functions are used in the convolution depending on the raw signal amplitude $w(t)$:

$$s(t) = (w * f)(t) = \int_{t_{\min}}^{t_{\max}} w(\tau) f(w(\tau)|t - \tau) d\tau. \quad (8.5)$$

The signal sampled in time bins n is then given by

$$s_n = \sum_{m=1}^n w_m f(w_m|t_n - t_m) (t_m - t_{m-1})$$

with the discrete charge dependent response function

$$f(Q|t) = f_i(t) \quad \text{for} \quad Q \in \left[\frac{Q_i + Q_{i-1}}{2}, \frac{Q_i + Q_{i+1}}{2} \right],$$

with $i = 1, \dots, k = 6$, $Q_1 = 1 \text{ fC}, \dots, Q_k = 50 \text{ fC}$ and $f_i(t)$ shown in Figure 8.10. The convolution of the muon signal in Figure 8.7 is shown in Figure 8.8.

Figure 8.10 shows the simulated response of the ASD chip to 4 ns long rectangular delta-like pulses for different integral charges $Q = 1 \text{ fC}, 2 \text{ fC}, 5 \text{ fC}, 10 \text{ fC}, 20 \text{ fC}, 50 \text{ fC}$, normalised to 1 fC input charge.

Two examples of simulated events corresponding to 1 kHz background rate are shown in Figure 8.2. The simulated events are scanned for threshold crossings taking into account masking of threshold crossings due to dead time of the ASD chip as well as the hysteresis (see section 2.2.2). The threshold crossing times obtained are then analysed in the same way as the measured ones in the previous chapters.

The Wilkinson ADC response is simulated by integrating the signal starting from the threshold crossing time for a period equal to the integration gate of the ADC of 18.5 ns. The integration result is directly used as ADC output for the time slewing corrections described in section 4.3.3.

8.3 Simulation of Resolution and Efficiency Under Irradiation

8.3.1 Comparison with Measurements Under Photon Irradiation

Figure 8.11 shows the simulated spatial resolution as a function of the photon background rate in comparison with the measurements at the GIF (see chapter 6). In addition to the results for minimum dead time of 220 ns, the spatial resolution is shown for the additional requirement $\Delta t > 600$ ns on the time between two subsequent hits. In chapter 6, it was concluded that the difference in spatial resolution with and without the additional requirement is caused by signal pile-up. This is confirmed by the simulation which reproduces the difference.

Figure 8.12 shows the 3σ -efficiency for minimum dead time obtained from measurements and simulation as a function of the photon background rate. Simulation and measurement agree very well. In addition, the prediction without signal pile-up according to equation (3.4) is shown. One concludes, that signal pile-up degrades the 3σ -efficiency by more than 10 % for background rates above 1 MHz per tube. This gives the room for improvements of the read-out electronics which are discussed in section 8.4.

8.3.2 Comparison with Measurements Under Proton Irradiation

In contrast to the measurements under photon irradiation, where space charge effects are small, the space charge densities reached in the measurements under proton irradiation (see chapter 7) are much higher, causing significant gain drop. Hence, the gain drop needs to be included in the simulation and also the non-uniformity of the irradiation needs to be taken into account. It was concluded that the effective gain drop experienced by muons is smaller than the gain drop experienced by the protons in the beam configuration at the Tandem accelerator with non-uniform irradiation, caused by the limited wobbler frequency. The effective gain drop was found to be well described for muon tracks by partitioning the 7 cm long irradiated region along the tube into two parts, where the whole proton rate is assumed to be concentrated in 60 % of the irradiated

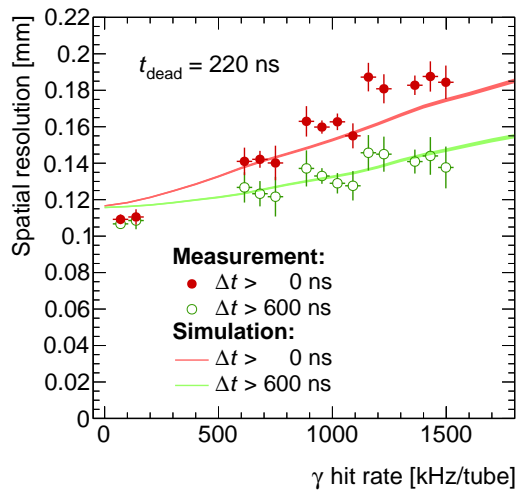


Figure 8.11: Dependence of the average spatial resolution on the photon background rate for the minimum dead time of 220 ns. The simulation agrees well with the measurements with the additional requirement $\Delta t > 600$ ns. Without the requirement the measured deterioration at high rates somewhat exceeds the expectation.

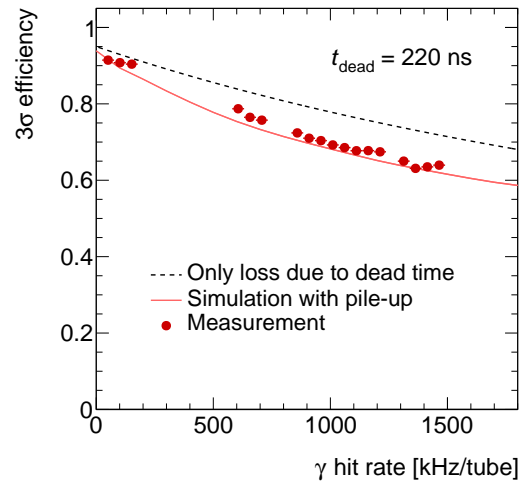


Figure 8.12: Simulated and measured degradation of the 3σ -efficiency with increasing photon background rate for the minimum dead time of 220 ns. In addition, the prediction without signal pile-up according to equation (3.4) is shown as dashed line.

region while the remaining 40 % are assumed to be unirradiated (cf. Figure 7.5). The protons are assumed to see the whole rate concentrated in 60 % of the irradiated region. This results in the relative gas amplification shown in Figure 7.6 for muons and in Figure 7.7 for protons.

Recorded proton signals are not available. Therefore, photon signals are used instead and scaled by the ratio of primary electrons created by photons (900; see above) and protons (5800; cf. section 7.4), which is approximately 6.5. Simulation results for three different models for the gain drop experienced by the muons are compared to the measurement results of chapter 7. They are described in the following.

Partitioned gain drop: In 60 % of the events, the muon signal amplitude is scaled by the relative gas amplification G/G_0 with $G = G \left(\frac{N}{0.6 \cdot A_{\text{irr}}} \right)$ from Diethorn's equation, where N is the overall proton hit rate and A_{irr} the irradiated tube cross section $7.0 \times 1.42 \text{ cm}^2$, while the remaining 40 % of the muon signals are not re-scaled. All proton signal amplitudes are scaled by G/G_0 with $G = G \left(\frac{N}{0.6 \cdot A_{\text{irr}}} \right)$, as the protons see the full space charge density.

Uniform gain drop: All muon signal amplitudes are scaled with the average value of the relative gas gain $G/G_0 = \frac{1}{G_0} \left[0.4 \cdot G_0 + 0.6 \cdot G \left(\frac{N}{0.6 \cdot A_{\text{irr}}} \right) \right]$ corresponding to equal gain drop for all muon hits. The proton signals are treated as above.

No gain drop: The muon signal amplitudes are not modified. The proton signals are treated as above.

Figure 8.13 shows the measured spatial resolution from chapter 7 in the (non-uniformly) irradiated and in the non-irradiated regions as a function of the proton rate together with the three simulation models. The spatial resolution measured in the non-irradiated region is well described by the model with no gain drop confirming that the space charge is limited to the irradiated region. The simulation assuming uniform gain drop describes well the spatial resolution measured in the irradiated region. The partitioned gain drop model predicts a significantly worse spatial resolution than the measured. A reason for the deviation might be in the too simple modelling of the non-uniform irradiation.

The dependence of the 3σ -efficiency on the proton rate in the non-irradiated regions of the sMDT tubes is shown in Figure 8.14 together with the analytic prediction taking only dead time effects into account. The simulation agrees very well with the measurement. The lower efficiency at low rates with respect to the analytic prediction is caused by signal-pileup. At very high rates, the gain drop experienced by the protons causes a loss of the proton signal amplitude, which in turn reduces the signal pile-up effect.

The dependence of the 3σ -efficiency in the irradiated region of the sMDT tubes on the proton rate is shown in Figure 8.15. Measurements in the irradiated region (cf. Figure 7.11) are shown

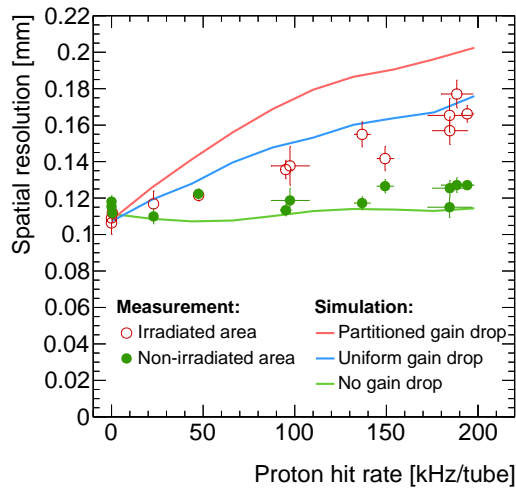


Figure 8.13: Muon spatial resolution in sMDT tubes as a function of the proton hit rate measured in chapter 7 in comparison with the simulation models with partitioned gain drop, uniform gain drop and without gain drop (see text).

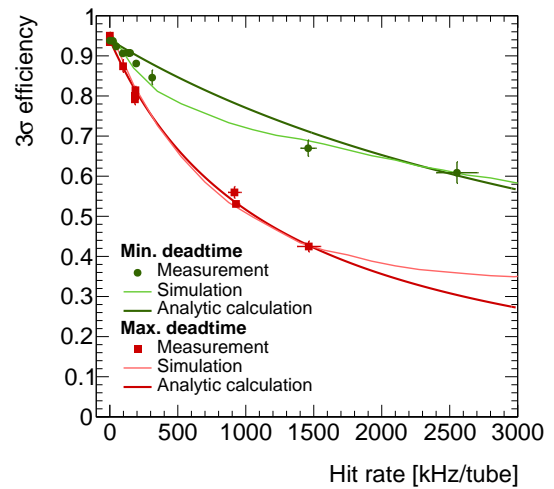


Figure 8.14: The muon 3σ -efficiency in the non-irradiated regions of the sMDT tubes measured in chapter 7 as a function of the proton rate for minimum and maximum dead time settings in comparison with the analytic prediction in equation (3.4) and with the simulation results obtained without gain drop for the muons, only for the protons (see text).

for the minimum and the maximum dead time settings in comparison to simulations with the uniform and partitioned gain drop models. While the uniform gain drop model predicts too high efficiencies, the partitioned model describes the measurements very well.

The systematic uncertainty due to the proton signal amplitude scale is small because signal pile-up does not contribute significantly in the proton irradiation: At low proton rates, overlapping muon and background signals are rare while at high rates protons experience strong gain drop which reduces the signal amplitude and hence the influence of signal pile-up (at 500 kHz proton rate the gain drops to 15 %, at 2500 kHz to 10 % of the nominal value). For 50 % uncertainty in the proton signal amplitude scale, the systematic error on the 3σ -efficiency is about 3 %.

8.3.3 Simulation of Other Chamber Geometries Under Photon Irradiation

The maximum rate reached in the measurements with sMDT tubes under irradiation with 662 keV photons at the GIF (see chapter 6) is 1500 kHz per tube in $l = 95$ cm long drift tubes or $\frac{1500 \text{ kHz}}{2Rl} \approx 10 \text{ kHz/cm}^2$, where $R = 7.1$ mm is the inner tube radius. At a photon rate of 10 kHz/cm^2 , the gas gain drops to about 80 % of its nominal value due to the space charge (cf. sections 3.3.1

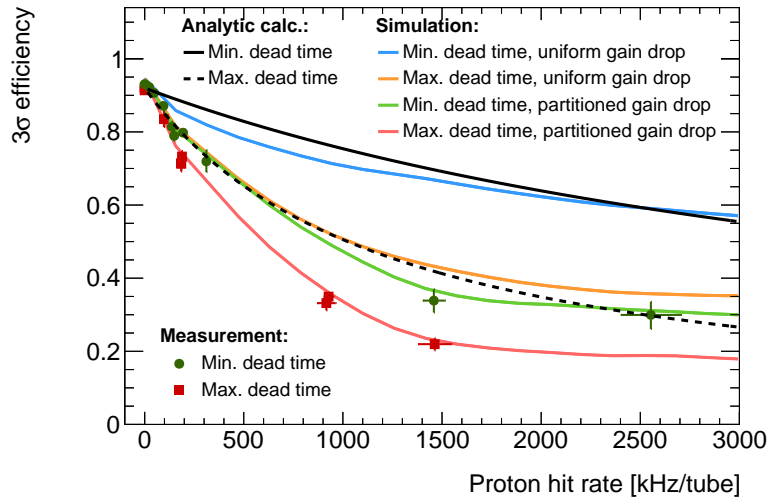


Figure 8.15: The muon 3σ -efficiency in the irradiated region of the sMDT tubes measured in chapter 7 as a function of the proton rate for minimum and maximum dead time settings in comparison with the results obtained with the uniform and partitioned gain drop simulation (see text). In addition, the analytic prediction in equation (3.4) taking into account only dead time effects is shown.

and 6.5.1). The performance loss of the sMDT tubes is predominantly caused by signal pile-up, which depends on the counting rate per drift tube. Therefore, for chambers with other drift tube lengths, the relative impact of signal pile-up and space charge effects on the performance differs.

Figure 8.16 shows simulated spatial resolution and 3σ -efficiency as a function of the background rate obtained from simulation for three different drift tube lengths with and without taking into account gain drop. The maximum expected background rate in the ATLAS Muon Spectrometer at HL-LHC is 14 kHz/cm^2 in the innermost end-cap layer [43]. This maximum rate is only reached close to the beam pipe in sMDT chambers replacing the existing chambers. In this region, the sMDT drift tubes experiencing the highest background flux would be 50 cm long and provide a spatial resolution of approximately $160 \mu\text{m}$ and a 3σ -efficiency of approximately 67%. Drift tube chambers with 200 cm tube length provide similar performance at a four times lower background flux of 3.5 kHz/cm^2 , which is sufficient for all other detector regions besides the inner end-cap layer at HL-LHC.

8.4 Improvements of Signal Processing for High Rates

As has been shown above, the predominant effect deteriorating to the performance of sMDT tubes at high rates is signal pile-up on the overshoot caused by the bipolar shaping of the standard

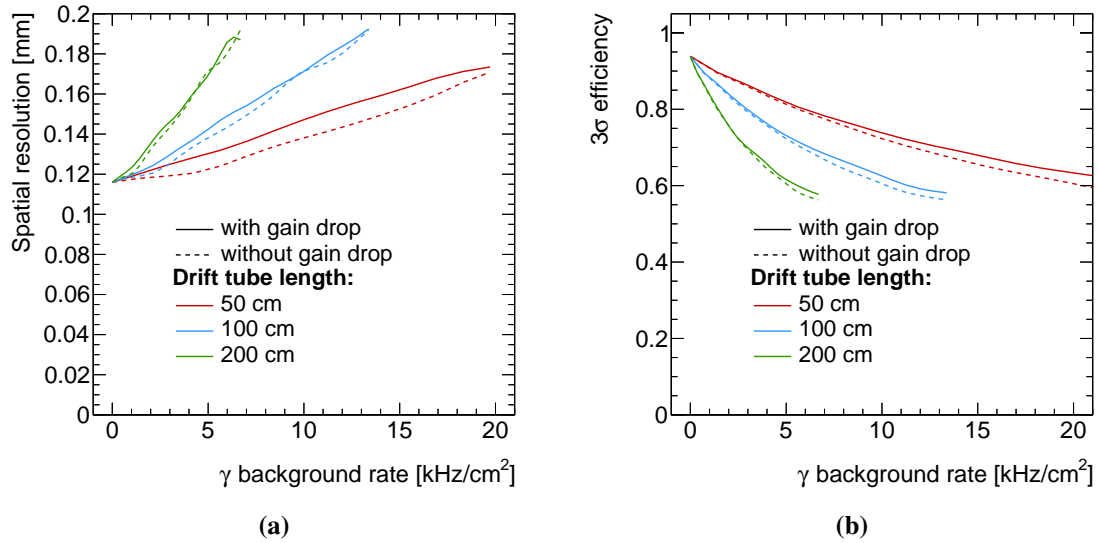


Figure 8.16: Simulation of the dependence of (a) the spatial resolution and (b) the 3σ -efficiency on the photon background flux for three different drift tube lengths obtained with and without taking gain drop into account.

MDT read-out electronics. A well known solution for suppressing this overshoot active baseline restoration [75] for instance implemented in the front-end electronics of the ATLAS Transition Radiation Tracker (see section 1.3.1), the ASDBLR* chip [76], and in the front-end electronics of the CDF Outer Tracker, the ASDQ chip [77].

Measurements with the ASDQ chip on an sMDT chamber have been performed in order to evaluate the improvement of the spatial resolution and 3σ -efficiency with active baseline restoration [68]. Despite the too short peaking time and too high discriminator threshold of the ASDQ for sMDT chambers, which results in a degraded spatial resolution and big efficiency loss near the sense wire where the signal amplitudes become smaller, a significant reduction of the degradation of the 3σ -efficiency and of the spatial resolution with increasing background rate has been observed.

In the following, an empirical approach is used to describe the response of new optimised read-out electronics for sMDT tubes corresponding to an ASD chip combined with active baseline restoration in order to evaluate the possible improvements in performance.

Figure 8.17 shows a typical sMDT muon signal recorded with the oscilloscope at the analogue monitoring output of the ASDQ chip with active baseline restoration. An overshoot is hardly visible. Figure 8.18 shows a muon signal recorded with the standard MDT ASD chip, which shows the distinctive overshoot. The baseline restoration circuit is based on diodes and consequently

* Amplifier/Shaper/Discriminator with active baseline restoration

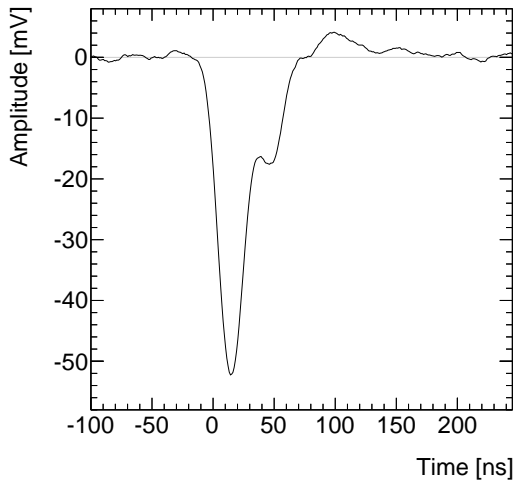


Figure 8.17: Muon signal recorded with the ASDQ chip on an sMDT chamber. An undershoot is hardly visible due to the active baseline restoration.

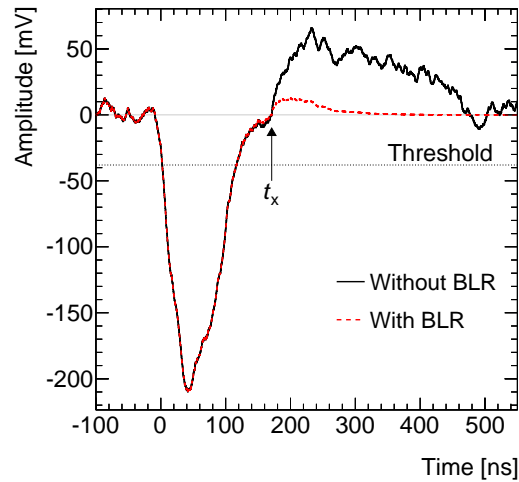


Figure 8.18: Muon signal recorded with the ASD chip with and without baseline restoration BLR (see text).

has non-linear response which cannot be expressed in a simple transfer function. Instead, in the empirical approach the functionality of the baseline restoration is mimicked by attenuating the signal amplitude exponentially after the zero crossing time t_x with a time constant of 50 ns, i.e.

$$s(t) \rightarrow s(t) \cdot e^{-\frac{t-t_x}{50\text{ns}}} \quad \text{for } t > t_x.$$

The red dashed line in Figure 8.18 shows the resulting signal with a very small remaining overshoot comparable to the one in the signals recorded with the ASDQ chip (see Figure 8.17).

Applying this method to the photon background signals leads to a significant improvement of the spatial resolution and 3σ -efficiency. Figure 8.19 shows the spatial resolution for sMDT tubes as a function of the photon background rate as in Figure 8.11. In addition, the simulation result with active baseline restoration is shown. The degradation with increasing photon background rate is strongly reduced. At the highest rate of 1500 kHz per tube, the spatial resolution is expected to improve from 180 μm to 130 μm . Likewise, the 3σ -efficiency is predicted to improve significantly as shown in Figure 8.20. With active baseline restoration, the efficiency is very close to the expectation for the case that only dead time effects contribute, not signal pile-up and gain drop.

The dependence of the spatial resolution and the 3σ -efficiency on the background rate and with and without taking gain drop into account with baseline restoration is shown for different tube lengths in Figures 8.21 and 8.22. The maximum flux values shown correspond to 2 MHz

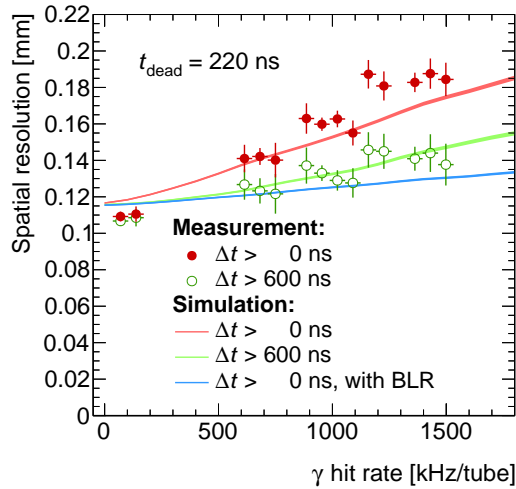


Figure 8.19: Dependence of the measured and simulated spatial resolution of sMDT tubes on the photon background rate. The prediction for active baseline restoration (BLR) added in the ASD read-out in simulation is also shown.

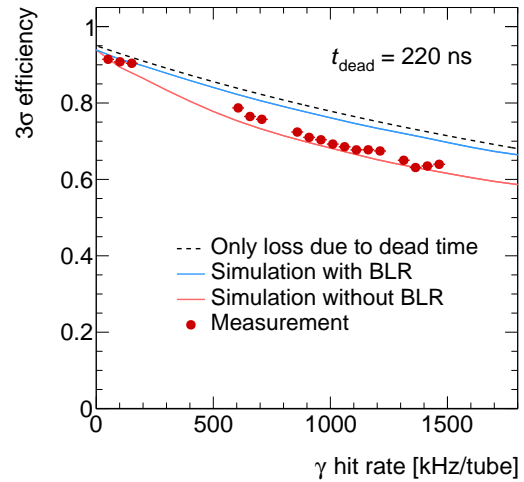


Figure 8.20: Dependence of the measured and simulated 3σ -efficiency for minimum dead time of 220 ns on the photon background rate. The simulation including baseline restoration (BLR) is very close to the optimum expected for only dead time effects (dashed line).

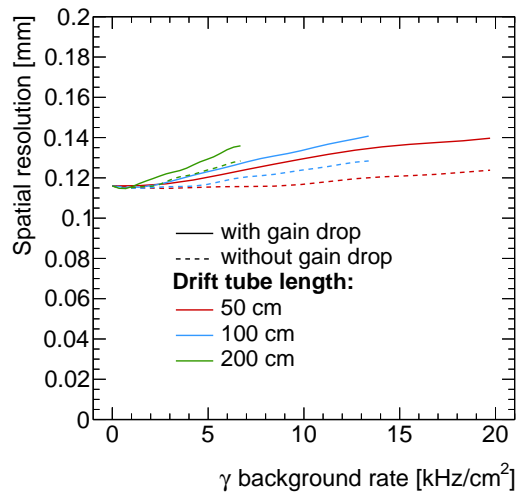


Figure 8.21: Simulated dependence of the spatial resolution on the background flux with baseline restoration (BLR) for different drift tube lengths.

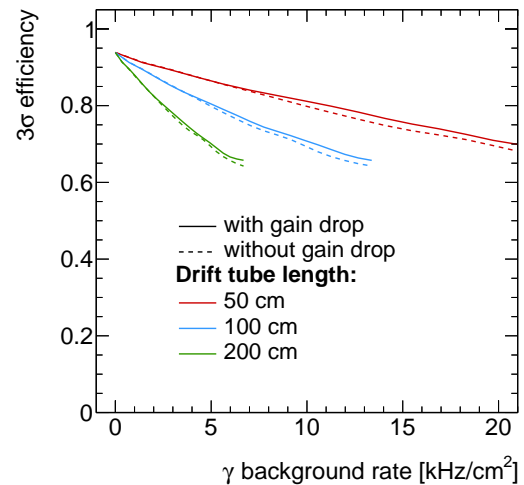


Figure 8.22: Simulated dependence of the 3σ -efficiency on the background flux with baseline restoration (BLR) for different drift tube lengths.

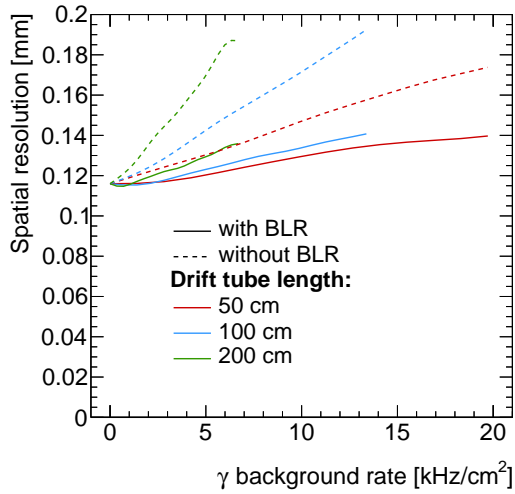


Figure 8.23: Simulated dependence of the spatial resolution on the background flux with and without baseline restoration (BLR) for different drift tube lengths.

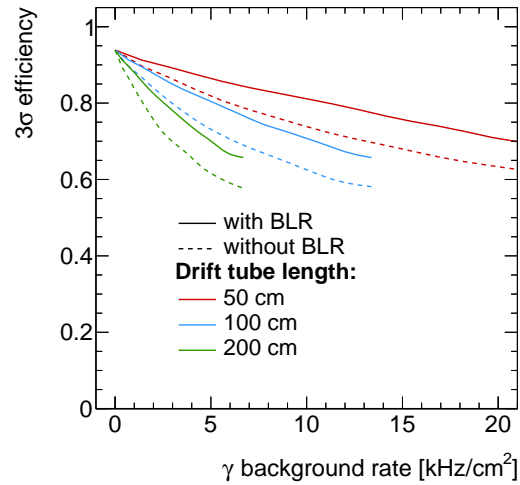


Figure 8.24: Simulated dependence of the 3σ -efficiency on the background flux with and without baseline restoration (BLR) for different drift tube lengths.

counting rate per tube where the efficiency drop due to dead time effects is 65 %.

Finally, in Figures 8.23 and 8.24 the spatial resolution and the 3σ -efficiency, respectively, are compared with and without active baseline restoration. Both resolution and efficiency are significantly improved with baseline restoration.

9

Comparison of the MDT and sMDT Drift Tube Performance

In this chapter, the results of measurements and simulations of the background rate dependence of the MDT and sMDT drift tube performance are compared and summarised.

9.1 Loss of Gas Amplification

Figure 9.1 shows the relative gas amplification G/G_0 of sMDT and MDT drift tubes as a function of the flux of photon conversions. The nominal value of the gas amplification is $G_0 = 2 \cdot 10^4$. In the presence of background radiation, G drops due to the radiation induced ion space charge in the tubes which shields the anode wire potential as discussed in section 3.3.1. For MDT tubes, G drops to 80 % of the nominal value at a flux of 930 Hz/cm^2 , while the corresponding rate for sMDT tubes is 10.39 kHz/cm^2 . This implies an improvement of the rate capability with respect to space charge of sMDT compared to MDT tubes by an order of magnitude. The results of the measurements both for MDT and sMDT tubes agree very well with the predictions by Diethorn's equation [52] for the estimates of the primary ionisation charge of photons converting in the tube walls of $900 e$ and $1300 e$, respectively.

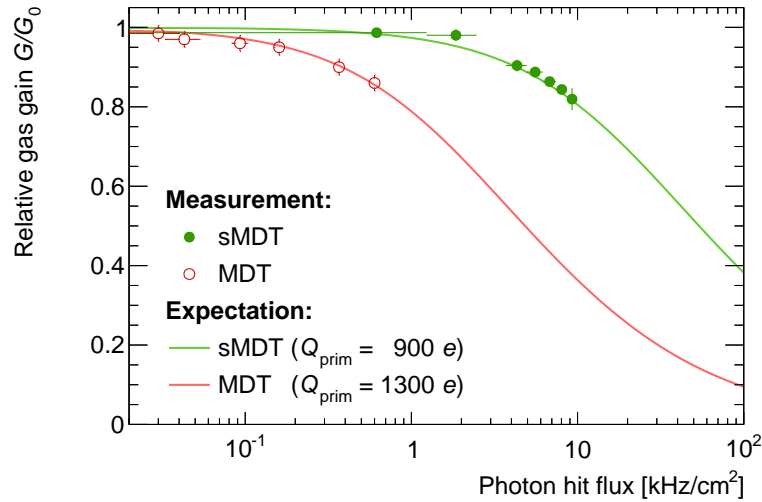


Figure 9.1: Dependence of the relative gas gain G/G_0 in MDT and sMDT tubes on the flux of photon conversions ($G_0 = 2 \cdot 10^4$). The sMDT data (see Figure 6.18) have been corrected for voltage drop in the noise filters. The MDT data are taken from [54]. The expectation is based on Diethorn's equation described in section 3.3.1 for the specified primary ionisation charges Q_{prim} of the converted photons.

9.2 Spatial Resolution

The effect of photon background radiation on the average drift tube spatial resolution is shown in Figure 9.2. For MDT tubes, the degradation of the spatial resolution is dominated by space charge effects (see section 3.3) which depend on the background flux and are independent of the tube length. The MDT measurements were performed with 377 cm long tubes as described in chapter 5. A fit of the function in equation (5.2) is shown as dashed line. The error band indicates the 68 % confidence level of the fit.

For sMDT tubes, space charge effects are strongly suppressed and the degradation of the spatial resolution is dominated by the signal pile-up effect (see section 3.4.3) which depends on the counting rate per tube and, thus, for a given background flux on the tube length. The sMDT measurements have been performed with 95 cm long tubes and are described in chapter 6. Both measurements and simulations for the sMDT tubes are shown with and without the requirement of $\Delta t > 600$ ns on the time difference between two successive hits, which is equivalent to operation with an electronics dead time of 600 ns. The measurements are described very well by the simulation. In addition, the simulation result for active baseline restoration (BLR) is shown, which largely eliminates the signal pile-up effect (see chapter 8).

An expectation for the sMDT spatial resolution can be derived from the average MDT resolution in the drift radius range $r < r_{\max}^{\text{sMDT}} = 7.1$ mm and the ten times higher rate capability in terms of space charge (see above). This expectation does not take into account signal pile-up and agrees with the measured sMDT tube resolution with the requirement $\Delta t > 600$ ns and the simulation with baseline restoration, where signal pile-up is irrelevant.

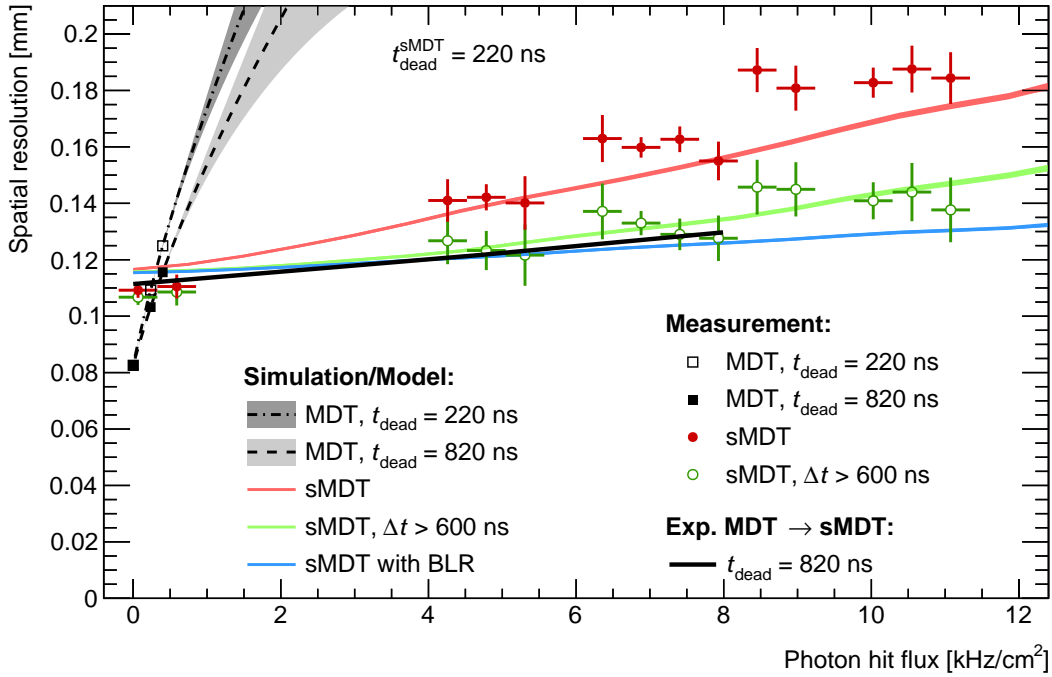


Figure 9.2: Dependence of the average sMDT and MDT drift tube spatial resolution on the flux of photon conversions for minimum and maximum dead time settings of the standard MDT read-out electronics of 220 ns and 820 ns, respectively. In addition, the sMDT resolution with the additional requirement $\Delta t > 600$ ns for the time interval between two successive hits is shown, which is equivalent to operation with an electronics dead time of 600 ns. Solid coloured lines show the simulated sMDT resolution with and without active baseline restoration BLR (see section 8.4). The black line shows an expectation using the average MDT resolution in the drift radius range $r < r_{\max}^{\text{sMDT}} = 7.1$ mm and scaling the rate by a factor of 10 to account for the one order of magnitude higher rate capability of the sMDT tubes in terms of gain drop. The dashed line shows a fit to the MDT data (see text).

The simulation model (see chapter 8) allows for the prediction of the sMDT spatial resolution for other tube lengths. Figure 9.3 shows the results for two tube lengths — 50 cm and 200 cm. The case of 50 cm tube length corresponds to the inner radius of the Small Wheels, the innermost end-cap layer of the ATLAS Muon Spectrometer, which need to be replaced at HL-LHC because

the rate capability of the current detectors will be exceeded. A maximum photon hit flux of 14 kHz/cm^2 is expected in these regions at HL-LHC. The sMDT drift tube spatial resolution for this case is $160 \mu\text{m}$ without baseline restoration improving to $135 \mu\text{m}$ with baseline restoration.

sMDT chambers with 200 cm tube length can easily be operated at rates up to 5 kHz/cm^2 , while the rate limit for safe operation of MDT tubes with respect to gain loss and spatial resolution is around 1 kHz/cm^2 independent of the tube length.

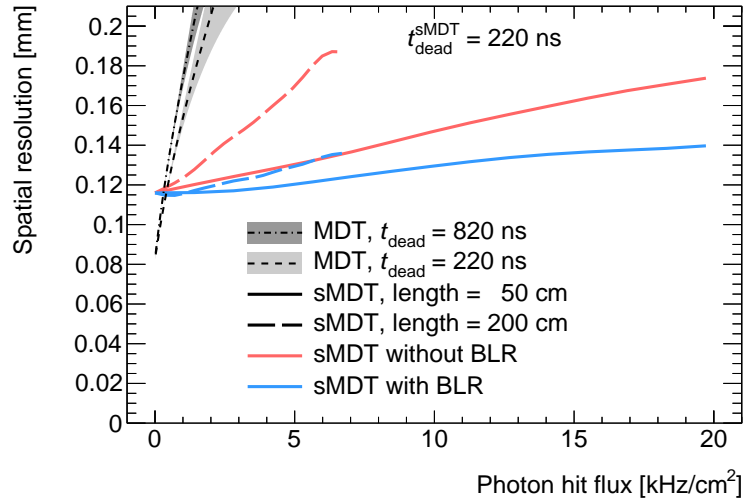


Figure 9.3: Prediction of the average MDT and sMDT drift tube spatial resolution as a function of the flux of photon conversions for different tube lengths. The resolution of the MDT tubes operated at the nominal dead time of 820 ns (from Figure 9.2) is independent of the tube length as signal pile-up is eliminated with this dead time setting. For sMDT tubes, signal pile-up is the dominant reason of resolution degradation in the range up to 20 kHz/cm^2 , where the gas gain drop is below 50 % (cf. Figure 9.1). As signal pile-up depends on the counting rate per tube, the resolution degradation with increasing photon flux of 200 cm long tubes is four times higher than for 50 cm long tubes without baseline restoration.

9.3 Drift Tube Efficiency

The drift tube 3σ -efficiency depends on the counting rate per tube and on the electronics dead time (see section 3.4). Only at very high space charge, gain drop reduces the detection efficiency of the drift tubes which otherwise is 100 % (see chapter 7). Results from measurements and simulation of the 3σ -efficiency are shown in Figure 9.4 together with the analytic calculation according to equation (3.4). The 3σ -efficiency of detecting a real muon hit not a background hit under irradiation is defined as the probability to measure a drift radius deviating by less than three

times the drift tube spatial resolution from the expected value from extrapolation of a reference track to the drift tube.

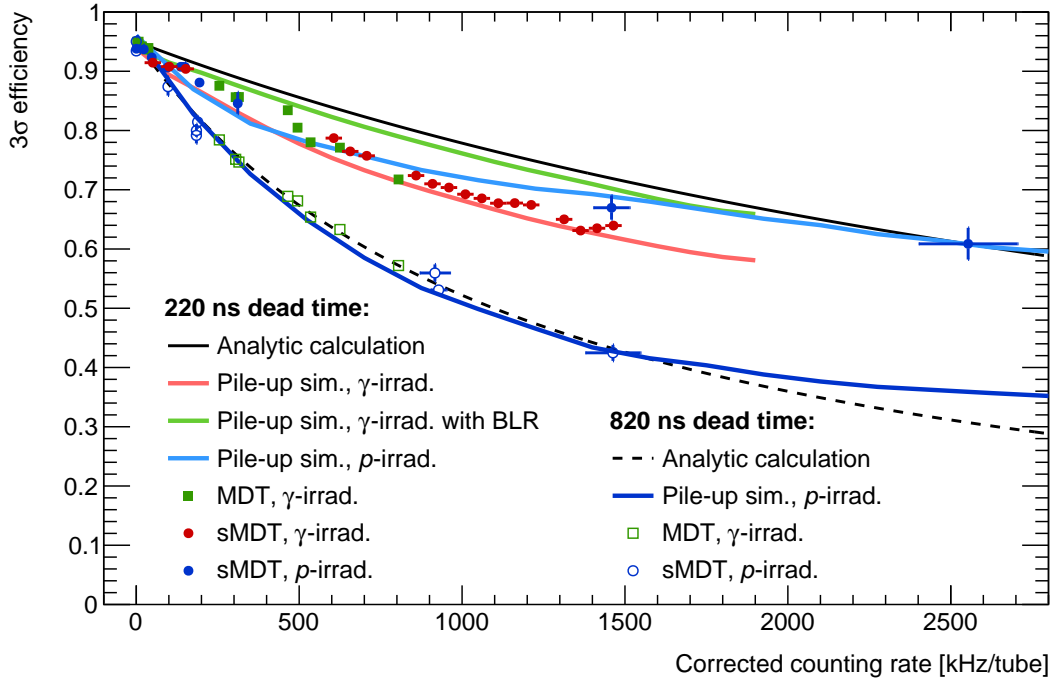


Figure 9.4: Dependence of the 3σ -efficiency of sMDT and MDT drift tubes on the counting rate measured in the tubes corrected for electronics dead time for minimum and maximum dead time of the standard MDT read-out electronics of 220 ns and 820 ns, respectively. Measurements have been performed under photon irradiation at the GIF (MDT, sMDT) and under proton irradiation (sMDT). For the analytic calculation the prediction by equation (3.4) is used.

One can see that the measurements for both MDT and sMDT tubes operated with the maximum dead time setting of 820 ns agree very well with the analytic prediction which takes into account only dead time effects. With the minimum dead time setting of 220 ns, the measured efficiency is significantly lower than the simple prediction. The difference is due to the signal pile-up effect which is very well reproduced by the simulation. In addition, the simulation result with additional active baseline restoration (BLR) is shown, which largely recovers the efficiency loss due to the signal pile-up effect bringing the efficiency very close (within 2 %) to the analytical prediction which marks the optimum for the given dead time setting.

The two points measured at the highest rates with the short dead time with proton irradiation deviate from the extrapolation of the measurements and simulation under photon irradiation. This is an artefact of the experimental setup where the drift tubes were irradiated locally with protons,

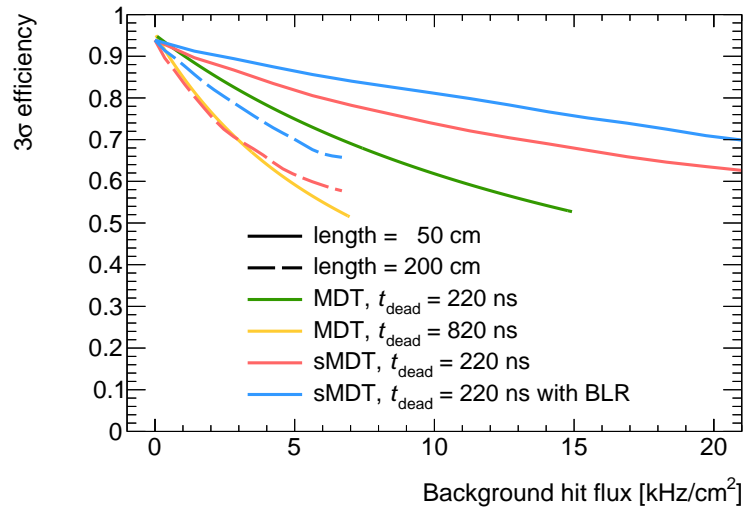


Figure 9.5: Dependence of the 3σ -efficiency of sMDT and MDT tubes on the corrected counting rate normalised to the area cross-section of the tubes. The efficiency is shown for 50 cm and 200 cm long tubes. The sMDT values are from simulation (see chapter 8), the MDT values from fits to the measured efficiency (see chapter 5).

while the efficiency is measured outside of the irradiated region and is very well reproduced by the simulation. At the highest proton rates, the gas gain in the irradiated region drops to only 10 % of the nominal value. The very low gas gain and consequently low amplitude of the proton signals reduces the pile-up effect. The cosmic muon hits outside of the irradiated region for which the efficiency is measured are not affected by the gain drop in the irradiated region.

Figure 9.5 shows the predicted 3σ -efficiency of MDT and sMDT tubes as a function of the dead time corrected flux. One can see that a reduction of the baseline dead time setting of 820 ns to the minimum value of 220 ns yields a significant improvement for the MDT tube efficiency. The rate capability of sMDT tubes with the same length is still a factor two higher due to the smaller cross-section area exposed to the uniform irradiation. A disadvantage of operating the MDT tubes with the minimum dead time, which is shorter than the maximum drift time of the MDT tubes, is the increase of the number of threshold crossings per hit by about 30 % (see section 5.3.3) which increases the required buffer size and bandwidth of the read-out electronics. The 3σ -efficiency of 50 cm long MDT tubes at the inner radius of the Small Wheels, where the expected background rate is maximum 14 kHz/cm^2 at HL-LHC, is 70 % without and 77 % with active baseline restoration.

The smaller tube diameter of the sMDT chambers also allows for using a larger number of tube layers per chamber in the same available space in the Muon Spectrometer which, together with the increased single-tube efficiency at high rates, improves the track segment reconstruction

efficiency and resolution of the sMDT chambers. For a single-tube efficiency ε , the probability to get at least m muon hits in n drift tube layers is

$$\sum_{k=m}^n \binom{n}{k} \varepsilon^k (1 - \varepsilon)^{n-k},$$

which in an sMDT chamber with $n = 2 \times 6$ tube layers and $\varepsilon > 70\%$ is always more than 99% if at least $m = 5$ hits are required. An estimate of the track segment resolution of new sMDT chambers in the Small Wheels as a function of the distance R from the beam line based on the rate dependence of the single-tube efficiency and resolution described above is shown in Figure 9.6. The variation of the chamber resolution as a function of R is due to the R -dependence of the tube length, which increases approximately linearly with R , and due to the background rate, which decreases rapidly with R (cf. Figure 3.3). The step in the chamber resolution at $R = 220$ cm is due a proposed change from 2×6 tube layers per chamber to 2×4 which is sufficient at larger R . A chamber resolution of better than $40 \mu\text{m}$ is achieved up to the highest expected rates, which fulfils the requirements for the ATLAS Muon Spectrometer.

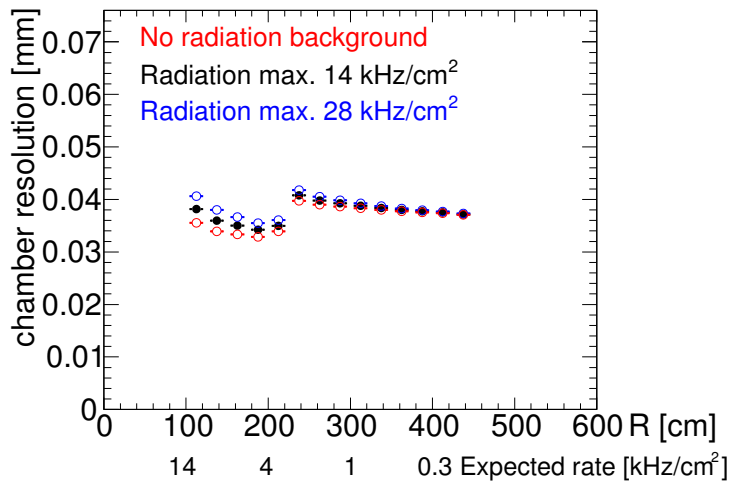


Figure 9.6: Expected dependence of the track segment resolution of sMDT chambers in the inner end-cap layer (Small Wheels) of the ATLAS Muon Spectrometer on the distance R from the beam line. The maximum expected rate is 14 kHz/cm^2 . In addition, the chamber resolution for double background rates and without background radiation is shown. The step at $R = 220$ cm is due to a higher number of tube layers per chamber at small R (see text).

Summary

After the first LHC run culminating in the discovery of the Higgs boson by the ATLAS and CMS experiments in 2012, preparations for the planned high-luminosity upgrade of the LHC to HL-LHC by the year 2025 have already begun. The increase in instantaneous luminosity by almost an order of magnitude increases the demands on the detectors and electronics of the LHC experiments. Many detector components will exceed their lifetimes or rate capability and will have to be replaced.

The background radiation in the ATLAS Muon Spectrometer consists mainly of photons and neutrons with energies of about 1 MeV. The efficiency of the Monitored Drift Tube (MDT) chambers, the precision tracking detectors of the ATLAS Muon Spectrometer, for those photons and neutrons is about $3 \cdot 10^{-4}$ and $5 \cdot 10^{-3}$, respectively. The MDT chambers consist of layers of aluminium drift tubes with 30 mm diameter. They are operated with Ar/CO₂ (93/7) gas mixture at 3 bar absolute pressure and with a wire potential of 3080 V corresponding to a gas amplification of $2 \cdot 10^4$, which is low enough to prevent ageing.

The spatial resolution and the muon efficiency of the MDT chambers degrades with increasing background irradiation rates. Beyond a hit rate of 1 kHz/cm², the efficiency and spatial resolution of the MDT tubes becomes too low because of a drop of the gas amplification by more than 20 % due to radiation induced space charge shielding the anode wire potential and because of fluctuations in the space charge causing variations of the drift velocity which cannot be taken into account in the calibration of the space-to-drift-time relationship.

In this thesis, new muon drift tube detectors with smaller tube diameter of 15 mm (sMDT chambers) have been developed and tested. The reduced tube diameter yields an improvement of the rate capability by about an order of magnitude. The maximum drift time in sMDT tubes is 185 ns, four times shorter than the maximum drift time in MDT tubes implying shorter signals and allowing for operation with an electronics dead time reduced by about the same factor, considerably improving the efficiency. An sMDT chamber has been tested with cosmic ray muons under 662 keV photon irradiation at the CERN Gamma Irradiation Facility (GIF) at rates of up to 11 kHz/cm². In addition, an sMDT chamber has been irradiated by a 20 MeV high

intensity proton beam of the Tandem-van-de-Graaff accelerator at the Maier-Leibnitz Laboratory in Garching. The drift-tube efficiency measurements in the GIF could be extended in this way up to counting rates of 2.5 MHz per tube corresponding to 17.6 kHz/cm^2 in 1 m long tubes. The 20 MeV protons deposit on average about 6.5 times more charge in the drift tube as the 662 keV photons. The photon irradiation measurements are very well described by a dedicated simulation of the signal formation and processing by the read-out electronics.

The measurements and simulation together showed that the sMDT chamber performance is limited by the current read-out electronics taken from the MDT chambers, where bipolar shaping is used in order to prevent baseline shift at high rates. A disadvantage of this shaping scheme is, however, the large and long overshoot it introduces at the end of each negative signal which effectively shifts the baseline for muon signals directly following a background signal. This deteriorates the resolution and effectively leads to an increased dead time which in turn degrades the efficiency. The signal pile-up effect can be mostly eliminated by using active baseline restoration after the shaping stage of the read-out electronics. The potential improvements have been studied by simulation.

The sMDT chambers with the current read-out electronics provide a drift tube spatial resolution of $160 \mu\text{m}$ and a muon efficiency of 70 % at the highest background irradiation rates of 14 kHz/cm^2 expected in the ATLAS Muon Spectrometer at HL-LHC in regions where the tube length is only 50 cm, while the resolution and efficiency without irradiation are $106 \mu\text{m}$ and 94 %, respectively. Simulation predicts improvement of the spatial resolution and efficiency to $135 \mu\text{m}$ and 77 %, respectively, if optimised read-out electronics with active baseline restoration are used. In other detector regions with lower expected irradiation rates much longer sMDT tube lengths can be used. Because of the smaller tube diameter, typically twice as many drift-tube layers can be installed in the same available volume in the ATLAS Muon Spectrometer, improving sMDT chamber tracking efficiency and resolution considerably. Together with their compatibility with respect to services and data acquisition system, this makes the sMDT chambers the best replacements for the MDT chambers with high background rates at HL-LHC in the ATLAS experiment. The first new sMDT chambers will be installed in ATLAS in the 2016/17 and 2019–2020 LHC shutdown periods.

A

Additional Time Slewing and Pile-Up Corrections

This chapter contains supplementary plots of the additional time slewing corrections under irradiation and the pile-up corrections.

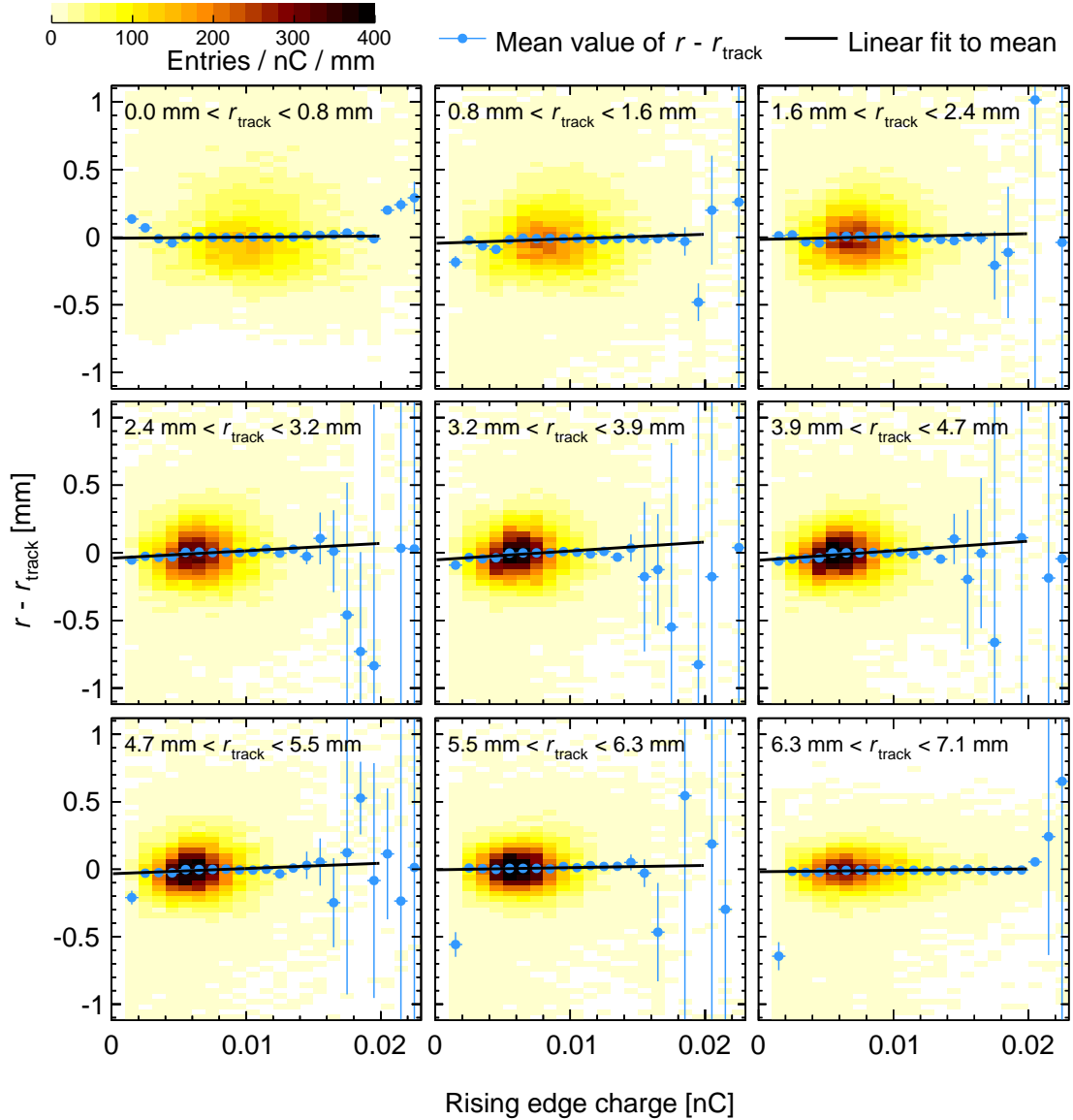


Figure A.1: Dependence of the track residuals on the rising edge charge measured by the Wilkinson ADC with an integration gate of 18.5 ns in bins of the impact radius r_{track} for all irradiated tubes after the additional time slewing corrections have been applied. The blue dots indicate the mean values of the residual distribution in the bins of the charge. The error bars correspond to the charge bin width and to the RMS of the residual distributions, respectively. Linear fits to the mean values are shown as a black lines. It can be seen that after the corrections, the charge dependence is eliminated.

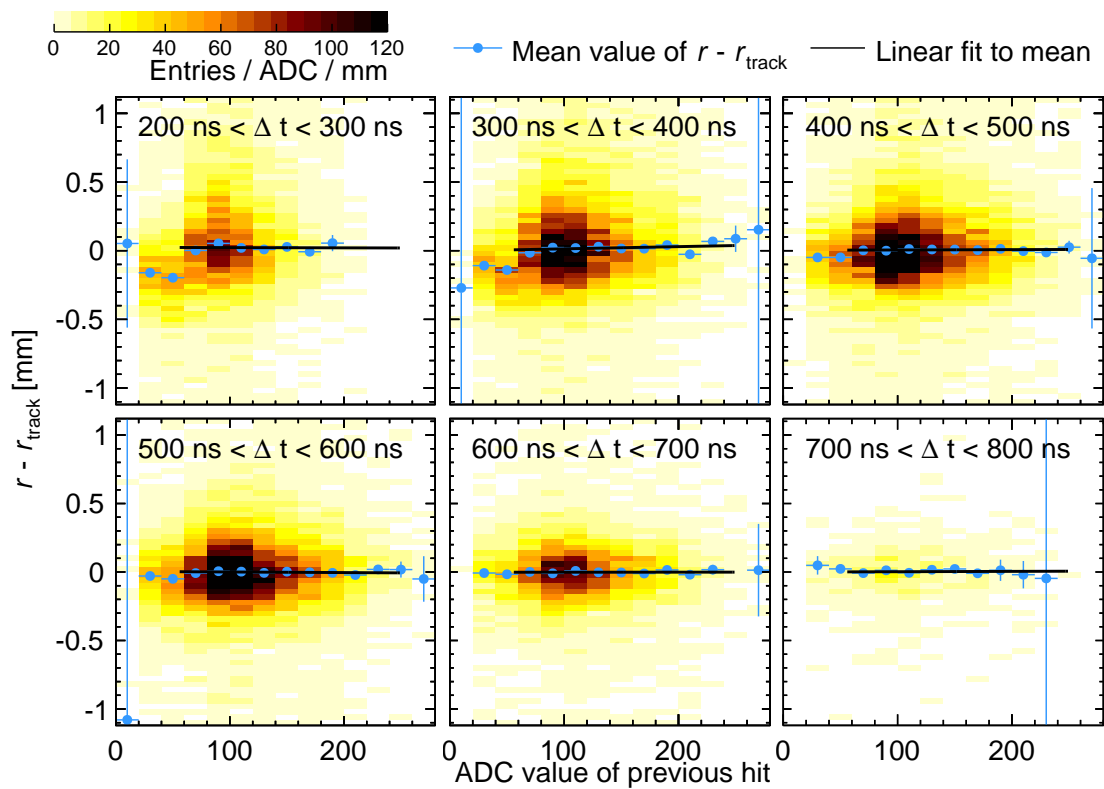


Figure A.2: Dependence of the residuals on the ADC counts of the preceding hit in sections of the time elapsed since the preceding hit after the pile-up corrections have been applied. Black markers indicate the mean values of the residual distribution in bins of the ADC counts. The error markers correspond to the bin width and the RMS in the horizontal and vertical direction, respectively. A linear fit to the mean values in the range 60 to 240 ADC counts is shown as a black line. It can be seen that after the corrections the charge dependence is eliminated.

List of Figures

1.1	The CERN accelerator complex.	3
1.2	The ATLAS experiment at the Large Hadron Collider [2].	4
1.3	The superconducting solenoid (blue) and toroid (red) magnet coils [2].	5
1.4	The ATLAS Inner Detector [2].	7
1.5	The ATLAS calorimeter system [2].	8
1.6	The ATLAS Muon Spectrometer [2].	10
1.7	Illustration of the Level-1 muon trigger	11
1.8	Illustration of the muon momentum measurement in the ATLAS Muon Spectrometer.	12
1.9	Schematic of the first level (L1) trigger [2].	13
1.10	CERN LHC and HL-LHC schedule [15].	14
2.1	Exploded view of the MDT end-plug and cross sections of an MDT drift tube in transverse and longitudinal direction [2].	19
2.2	Cluster density as a function of the muon kinetic energy at nominal MDT operating parameters	20
2.3	Schematic view of an ATLAS MDT chamber in the barrel region [2].	21
2.4	Photograph of the read-out end of an 2×3 layer MDT elx where the different electronics components are visible in sections of 3×8 tubes.	22
2.5	Electrical connections to an MDT drift tube.	22
2.6	Circuit diagram of the noise filters used in the high-voltage connections to suppress pick-up noise [29].	23
2.7	Block diagram of one ASD channel [28]	24
2.8	Response of the Wilkinson ADC of the ASD chip to a typical muon pulse [30].	25
2.9	Simulated delta pulse response of the ASD chip.	25
2.10	Calibration curve for the charge measurement of the Wilkinson ADC.	25
2.11	Schematic diagram of the MDT readout electronics [2].	27

2.12	Dependence of the single-tube spatial resolution on the drift radius determined from an external reference measurement with and without time slewing correction [35].	28
2.13	Illustration of the behaviour of the single-tube spatial resolution on the drift radius	28
2.14	Dependence of the hit and the 3σ -efficiency of the drift tubes on the drift radius depending on the number of hits taken into account in the read-out window [35].	29
2.15	Illustration of the effect of δ -electrons knocked out of atoms in the tube wall by the muons on the tube efficiency (see text).	29
2.16	Dependence of the average single-tube spatial resolution and 3σ -efficiency on the photon background rate.	31
2.17	Photograph of sMDT and MDT drift tubes.	32
2.18	Exploded view of an sMDT drift tube.	33
2.19	Photographs of the different stages of the sMDT chamber assembly	34
2.20	Photographs of the signal and high-voltage hedgehog boards for MDT and sMDT chambers	35
2.21	The sMDT prototype chamber mounted in a transport frame.	36
2.22	CAD model and photograph of a BME (barrel, middle, extra) sMDT chamber installed in April 2014 in the ATLAS Muon Spectrometer.	37
2.23	The middle layer of the muon spectrometer in the barrel region with the positions of new additional chambers, two in the “elevator region” and twelve in the “feet region”, indicated.	37
3.1	Simulated flux of photons and neutrons in one quadrant of the ATLAS detector at the LHC design luminosity of $1 \cdot 10^{34} \text{ cm}^{-2} \text{ s}^{-1}$ [46].	41
3.2	Expected background rates in the ATLAS muon chambers per drift tube and per cm^2 at $\sqrt{s} = 8 \text{ TeV}$	42
3.3	Expected hit rate in the inner end-cap layer of the ATLAS Muon Spectrometer, the so-called Small Wheels, as a function of the radial distance from the beam axis for MDT chambers and CSCs (cathode strip chambers) at an instantaneous luminosity of $3 \cdot 10^{34} \text{ cm}^{-2} \text{ s}^{-1}$ and $\sqrt{s} = 7 \text{ TeV}$ [19].	43
3.4	Radial dependence of the MDT spatial resolution for different photon irradiation rates [35].	44
3.5	Relative gas amplification in MDT and sMDT tubes at nominal operating conditions as a function of the photon background flux detected by the drift tubes for $Q_{\text{prim}} = 900 e$ and $1300 e$	47

3.6	Drift velocity in Ar/CO ₂ (93/7) at 3 bar absolute pressure as a function of the electric field strength (left) and of the drift radius (right) in Ar/CO ₂ (93/7) at 3 bar absolute pressure calculated with the Magboltz program [57].	47
3.7	Cross section of an MDT tube with an incident muon track and ionisation clusters.	49
3.8	Illustration of the signal induced by three distinct ionisation clusters.	49
3.9	Typical signals induced by muon tracks with impact radius $r = 4$ mm in MDT (left) and sMDT (right) drift tubes as simulated with the Garfield program [59].	50
3.10	A fast random sequence of signals processed by unipolar shaping and bipolar shaping [55]	50
3.11	Typical simulated signals created by muon tracks with drift radius $r = 4$ mm in MDT and sMDT drift tubes.	51
3.12	Comparison of the drift time spectra of MDT (30 mm diameter) and sMDT (15 mm diameter) drift tubes.	52
3.13	Calculated dependence of the observed counting rate and the muon efficiency on the real hit rate for minimum and maximum dead time setting of the ASD chip.	53
3.14	Illustration of the signal pile-up effects due to the undershoot caused by bipolar shaping.	54
4.1	Drift time spectrum of a uniformly illuminated sMDT chamber fitted with equation (4.5) at the rising edge (red) and equation (4.6) at the falling edge (blue) for the determination of the minimum and maximum drift times, respectively. . . .	58
4.2	Rising edge charge in ADC counts as a function of the drift radius.	60
4.3	Dependence of the time slewing Δt on the deviation ΔQ of the measured ADC counts from the peak in the bin $0.47 \text{ mm} < r_{\text{track}} < 0.71 \text{ mm}$	60
4.4	Dependence of the time slewing correction factor on the drift radius. The markers show the obtained values in slices of the impact parameter, the solid line indicates the fit of a quadratic curve.	60
4.5	Distribution of the track residuals $r - r_{\text{track}}$ as a function of r_{track} for an sMDT tube.	61
4.6	Projection of the bin $3.31 \text{ mm} < r_{\text{track}} < 3.79 \text{ mm}$ of the residual distribution fitted with equation (4.7).	61
5.1	Sketch of the experimental setup used in 2004 [35] at the CERN Gamma Irradiation Facility in the X5 muon beam.	66
5.2	Distribution of the time difference $\Delta t = t_2 - t_1$ between first and second hit for minimum and maximum dead time setting.	68

5.3	Measured analog response of the ASD chip to a 100 ns long rectangular input current pulse after the last shaping stage illustrating the afterpulsing caused by the imperfect ion tail cancellation of the ASD chip.	69
5.4	Total counting rate of all 24 drift tubes read out by one AMT chip for minimum and maximum dead time.	70
5.5	Cumulative drift time spectra of all 24 irradiated tubes read out with minimum dead time at different irradiation levels.	71
5.6	Single-tube spatial resolution as a function of the drift radius for different irradiation rates and maximum dead time averaged over the four drift tubes.	73
5.7	Degradation of the single-tube spatial resolution for minimum dead time averaged over the four drift tubes (see text).	73
5.8	Overall single-tube spatial resolution as a function of the photon hit rate for the minimum (220 ns) and maximum (820 ns) dead times. The dashed lines show fits of equation (5.2) to the data points.	75
5.9	Average 3σ -efficiency of the four drift tubes in the active area of the beam telescope as a function of the drift radius for different irradiation rates.	75
5.10	Dependence of the 3σ -efficiency of MDT tubes on the dead-time-corrected counting rate.	76
6.1	Schematic view of the experimental setup at the GIF.	78
6.2	Photograph of the experimental setup at the GIF.	79
6.3	Mapping of the drift tubes to the mezzanine boards.	80
6.4	Counting rates in the sMDT chamber in the GIF with attenuation factor 5.	81
6.5	Counting rates in the sMDT chamber in the GIF with attenuation factor 1. Part of the channels on the mezzanine boards in the strongly irradiated region are deactivated (white).	82
6.6	Temperature (left) and relative humidity (right) variations during the measurement campaign.	83
6.7	Variation of the gas pressure during the measurement campaign.	83
6.8	Variation of the currents drawn by the two multilayers during the measurement campaign.	83
6.9	Cumulative drift time and ADC spectra of all sMDT drift tubes in the GIF setup after time slewing corrections with the gamma source switched off	85
6.10	Dependence of the time slewing Δt the deviation of the charge measurement from the most probable charge ($Q - Q_{\text{peak}}$) and on the muon impact radius r_{track}	86

6.11	Dependence of the average spatial resolution of the analysed drift tubes without irradiation and without multiple scattering correction as a function of the tube layer z -coordinate with and without the quality requirement $\chi^2/n.d.f. < 1$ on the reference track (see text).	87
6.12	Dependence of the average spatial resolution of the drift tubes in the analysis region of the chamber on the reference track $\chi^2/n.d.f.$ of the reference track.	88
6.13	Normalised χ^2 distribution of the reference track.	88
6.14	Estimate of the multiple scattering contribution to the average spatial resolution for the analysed drift tube layers according to equation (6.2).	89
6.15	Average resolution of individual drift tubes in the analysis region in the GIF setup corrected for multiple scattering.	89
6.16	Average resolution of all drift tubes in the analysis region as a function of the drift radius.	89
6.17	Drift time spectrum of all irradiated drift tubes in the GIF setup at maximum photon flux.	90
6.19	Cumulative residual distributions as a function of the drift radius for drift tubes with hit rates in the range 1300 to 1500 kHz before and after correction.	92
6.20	Spatial resolution of sMDT drift tubes with multiple scattering corrections as a function of the drift radius for different hit rate intervals without and with requirement of a minimum time interval Δt between successive hits.	93
6.21	Average sMDT drift tube resolution with time slewing and multiple scattering corrections as a function of the hit rate with and without requirement on the minimum time interval Δt between successive hits.	94
6.22	Dependence of the track residuals on the rising edge charge measured by the Wilkinson ADC with an integration gate of 18.5 ns in bins of the impact radius r_{track} for all irradiated tubes.	95
6.23	Dependence of the residuals on the ADC counts of the preceding hit in sections of the time elapsed since the preceding hit.	96
6.24	Average spatial resolution of all drift tubes in the analysis region as a function of the hit rate before and after applying additional corrections.	97
6.25	3σ -efficiency as a function of the drift radius r in different intervals of the hit rate.	98
6.26	Average 3σ -efficiency in sMDT tubes as a function of the hit rate.	99
7.1	The custom designed sMDT chamber used for the measurements under proton irradiation.	102

7.2	Photograph of the experimental setup at the Tandem-van-de-Graaff accelerator with the sMDT chamber, the trigger scintillation counters, lead shielding and the beam pipe.	103
7.3	Schematic view of the setup at the Tandem accelerator perpendicular to the beam direction.	104
7.4	Cross sectional view of the custom designed sMDT chamber with a reconstructed muon track.	104
7.5	Illustration of the non-uniform irradiation in the Tandem measurements due to limited wobbler frequency.	107
7.6	Dependence of the relative gas amplification $G/G_0 = q/q_0$ in the Tandem setup on the proton irradiation rate.	107
7.7	Dependence of the relative gas amplification G/G_0 on the proton flux assuming uniform illumination over 60 % of the tube cross section.	108
7.8	Correlation between the sMDT counting rates with and without dead time correction and the reference measurement with a scintillation counter for maximum and minimum dead time setting.	109
7.9	Dependence of the spatial resolution on the hit rate in the unirradiated and irradiated regions.	110
7.10	Dependence of the 3σ -efficiency on the hit rate in the unirradiated regions in the Tandem setup.	111
7.11	Dependence of the 3σ -efficiency on the hit rate in the irradiated region	112
7.12	Dependence of the space charge dependent efficiency fraction on the relative gain drop measured for muons and protons.	113
8.1	Average measured and simulated average muon signals in sMDT tubes after the amplifier and shaper stages of the ASD chip.	116
8.2	Two examples of simulated events in sMDT tubes with 1 kHz uncorrelated rate of 662 keV photons.	118
8.3	Raw recorded photon signal in a sMDT tube measured with an oscilloscope with $50\ \Omega$ termination at the analogue output of the ASD chip.	119
8.4	The raw signal after preparation as simulation input.	119
8.5	Comparison of averaged muon and photon signals recorded in sMDT tubes at the GIF.	120
8.6	Dependence of the drift tube current on the photon hit rate compared to predictions based on Diethorn's formula for different numbers of primary ionisation electrons per converted photon.	120

8.7	Example of the current induced on the anode wire of a by a muon hit from Garfield simulation in 1 ns time bins.	121
8.8	The signal from Figure 8.7 after convolution with the charge dependent response function of the ASD chip.	121
8.9	Measured and simulated analogue response of the ASD chip to 4 ns long delta-like input pulses.	122
8.10	Simulated analogue response of the ASD chip to 4 ns long rectangular delta-like pulses for different integral signal charges normalised to 1 fC input charge. . . .	122
8.11	Simulated and measured dependence of the average spatial resolution on the photon background rate for the minimum dead time of 220 ns	124
8.12	Simulated and measured degradation of the 3σ -efficiency with increasing photon background rate for the minimum dead time of 220 ns.	124
8.13	Muon spatial resolution in sMDT tubes as a function of the proton hit rate measured in chapter 7 in comparison with the simulation models with partitioned gain drop, uniform gain drop and without gain drop.	126
8.14	The muon 3σ -efficiency in the non-irradiated regions of the sMDT tubes measured in chapter 7 as a function of the proton rate for minimum and maximum dead time settings in comparison with the analytic prediction in equation (3.4) and with the simulation results obtained without gain drop for the muons, only for the protons.	126
8.15	The muon 3σ -efficiency in the irradiated region of the sMDT tubes measured in chapter 7 as a function of the proton rate for minimum and maximum dead time settings in comparison with the results obtained with the uniform and partitioned gain drop simulation.	127
8.16	Simulation of the dependence of the spatial resolution and the 3σ -efficiency on the photon background flux for three different drift tube lengths obtained with and without taking gain drop into account.	128
8.17	Muon signal recorded with the ASDQ chip on an sMDT chamber.	129
8.18	Muon signal recorded with the ASD chip with and without baseline restoration BLR.	129
8.19	Dependence of the measured and simulated spatial resolution of sMDT tubes on the photon background rate.	130
8.20	Dependence of the measured and simulated 3σ -efficiency for minimum dead time of 220 ns on the photon background rate.	130
8.21	Simulated dependence of the spatial resolution on the background flux with baseline restoration (BLR) for different drift tube lengths.	130

8.22	Simulated dependence of the 3σ -efficiency on the background flux with baseline restoration (BLR) for different drift tube lengths.	130
8.23	Simulated dependence of the spatial resolution on the background flux with and without baseline restoration (BLR) for different drift tube lengths.	131
8.24	Simulated dependence of the 3σ -efficiency on the background flux with and without baseline restoration (BLR) for different drift tube lengths.	131
9.1	Dependence of the relative gas gain G/G_0 in MDT and sMDT tubes on the flux of photon conversions.	134
9.2	Dependence of the average sMDT and MDT drift tube spatial resolution on the flux of photon conversions for minimum and maximum dead time settings of the standard MDT read-out electronics of 220 ns and 820 ns, respectively.	135
9.3	Prediction of the average MDT and sMDT drift tube spatial resolution as a function of the flux of photon conversions for different tube lengths.	136
9.4	Dependence of the 3σ -efficiency of sMDT and MDT drift tubes on the counting rate measured in the tubes corrected for electronics dead time for minimum and maximum dead time of the standard MDT read-out electronics of 220 ns and 820 ns, respectively.	137
9.5	Dependence of the 3σ -efficiency of sMDT and MDT tubes on the corrected counting rate normalised to the area cross-section of the tubes.	138
9.6	Expected dependence of the track segment resolution of sMDT chambers in the inner end-cap layer (Small Wheels) of the ATLAS Muon Spectrometer on the distance R from the beam line.	139
A.1	Dependence of the track residuals on the rising edge charge measured by the Wilkinson ADC with an integration gate of 18.5 ns in bins of the impact radius r_{track} for all irradiated tubes after the additional time slewing corrections have been applied.	144
A.2	Dependence of the residuals on the ADC counts of the preceding hit in sections of the time elapsed since the preceding hit after the pile-up corrections have been applied.	145

List of Tables

1.1	Energy and transverse momentum resolution and η -coverage of the ATLAS sub-detectors.	6
2.1	MDT chamber parameters [2]	19
2.2	ASD analog specifications	23
2.3	Ranges and nominal values of the ASD operation parameters [30,31]	26
7.1	Overview of the irradiation conditions in the data recorded at the Tandem accelerator.	105

Bibliography

- [1] L. Evans and P. Bryant, *LHC Machine*, JINST **3** (2008) S08001.
- [2] ATLAS Collaboration, G. Aad et al., *The ATLAS Experiment at the CERN Large Hadron Collider*, JINST **3** (2008) S08003.
- [3] CMS Collaboration, S. Chatrchyan et al., *The CMS experiment at the CERN LHC*, JINST **3** (2008) S08004.
- [4] ATLAS Collaboration, G. Aad et al., *Observation of a new particle in the search for the Standard Model Higgs boson with the ATLAS detector at the LHC*, Phys.Lett. **B716** (2012) 1.
- [5] CMS Collaboration, S. Chatrchyan et al., *Observation of a new boson at a mass of 125 GeV with the CMS experiment at the LHC*, Phys.Lett. **B716** (2012) 30.
- [6] LHCb Collaboration, A. Augusto Alves, Jr. et al., *The LHCb Detector at the LHC*, JINST **3** (2008) S08005.
- [7] ALICE Collaboration, K. Aamodt et al., *The ALICE experiment at the CERN LHC*, JINST **3** (2008) S08002.
- [8] LHCf Collaboration, O. Adriani et al., *The LHCf detector at the CERN Large Hadron Collider*, JINST **3** (2008) S08006.
- [9] TOTEM Collaboration, G. Anelli et al., *The TOTEM experiment at the CERN Large Hadron Collider*, JINST **3** (2008) S08007.
- [10] MoEDAL Collaboration, J. Pinfold et al., *Technical Design Report of the MoEDAL Experiment*, CERN-LHCC-2009-006. MoEDAL-TDR-001, CERN, Geneva, June 2009, <https://cds.cern.ch/record/1181486>.

- [11] ATLAS Public Luminosity Results.
<https://twiki.cern.ch/twiki/bin/view/AtlasPublic/LuminosityPublicResults>.
- [12] ATLAS Collaboration, G. Aad et al., *Measurement of the Higgs boson mass from the $H \rightarrow \gamma\gamma$ and $H \rightarrow ZZ^* \rightarrow 4\ell$ channels with the ATLAS detector using 25 fb^{-1} of pp collision data*, arXiv:1406.3827 [hep-ex].
- [13] CMS Collaboration, S. Chatrchyan et al., *Observation of a new boson with mass near 125 GeV in pp collisions at $\sqrt{s} = 7$ and 8 TeV*, JHEP **1306** (2013) 081.
- [14] L. Arnaudon et al., *Linac4 Technical Design Report*, CERN report, CERN-AB-2006-084, CERN, Geneva, Dec. 2006, <http://cds.cern.ch/record/1004186>.
- [15] F. Bordry, "LHC schedule approved by CERN management and LHC experiments."
<http://lhc-commissioning.web.cern.ch/lhc-commissioning/schedule/LHC%20schedule%202015-2034%20FkBordry%20-december-2013.pdf>, Dec. 2013.
- [16] ATLAS Collaboration, *ATLAS Insertable B-Layer Technical Design Report*, CERN report, CERN-LHCC-2010-013. ATLAS-TDR-19, CERN, Geneva, Sept. 2010,
<http://cds.cern.ch/record/1291633>.
- [17] G. Aielli et al., *Proposal for the Upgrade of the Elevator Regions in the ATLAS Barrel Muon Spectrometer*, ATL-MUON-INT-2014-001, CERN, Geneva, Jan 2014.
- [18] ATLAS Collaboration, *Letter of Intent for the Phase-I Upgrade of the ATLAS Experiment*, CERN report, CERN-LHCC-2011-012, CERN, Geneva, Nov. 2011,
<http://cds.cern.ch/record/1402470>.
- [19] ATLAS Collaboration, M. L. Gonzalez Silva et al., *New Small Wheel Technical Design Report*, CERN report, CERN-LHCC-2013-006, CERN, Geneva, June 2013,
<http://cds.cern.ch/record/1552862>.
- [20] ATLAS Collaboration, *Letter of Intent for the Phase-II Upgrade of the ATLAS Experiment*, CERN report, CERN-LHCC-2012-022, CERN, Geneva, Dec. 2012,
<http://cds.cern.ch/record/1502664>.
- [21] E. Simioni et al., *The Topological Processor for the future ATLAS Level-1 Trigger: from design to commissioning*, arXiv:1406.4316 [physics.ins-det].
- [22] P. Schwegler, O. Kortner, H. Kroha, and R. Richter, *Improvement of the L1 trigger for the ATLAS muon spectrometer at high luminosity*, Nucl. Instr. Meth. A **718** (2013) 245 .

- [23] S. Nowak et al., *A Muon Trigger with high p_T -resolution for Phase-II of the LHC Upgrade, based on the ATLAS Muon Drift Tube Chambers*, ATL-MUON-PROC-2014-002, CERN, Geneva, June 2014, <https://cds.cern.ch/record/1711641>.
- [24] S. Horvat, O. Kortner, and H. Kroha, *Determination of the Spatial Drift-Tube Resolution using Muon Tracks*, ATL-MUON-PUB-2006-008, CERN, Geneva, Apr. 2006.
- [25] P. Bagnaia et al., *Calibration model for the MDT chambers of the ATLAS Muon Spectrometer*, ATL-MUON-PUB-2008-004, CERN, Geneva, Feb. 2008.
- [26] J. von Loeben, *Calibration of the ATLAS Precision Muon Chambers and Study of the Decay $\tau \rightarrow \mu\mu\mu$ at the Large Hadron Collider*, PhD thesis, Max-Planck-Institut für Physik and Technische Universität München, June 2010, CERN-THESIS-2010-099.
- [27] H. van der Graaf et al., *RasNiK, an Alignment System for the ATLAS MDT Barrel Muon Chambers: Technical System Description*, NIKHEF technical report, Amsterdam, 2000, <http://cds.cern.ch/record/1073160>.
- [28] Y. Arai et al., *ATLAS Muon Drift Tube Electronics*, JINST **3** (2008) P09001.
- [29] B. Bittner, *Alignment of the ATLAS Muon Spectrometer Using Muon Tracks*, diploma thesis, Max-Planck-Institut für Physik and Technische Universität München, 2009, MPP-2008-270.
- [30] C. Posch, E. Hazen, and J. Oliver, *MDT-ASD User's Manual*, ATL-MUON-2002-003, CERN, 2007, <http://cds.cern.ch/record/684217>.
- [31] Z. Yan and S. P. Ahlen, *ADC Performance and Calibration of MDT Chambers*, ATL-COM-MUON-2011-039, CERN, Geneva, Nov. 2011.
- [32] Y. Arai, *AMT-3 (ATLAS Muon TDC version 3) & AMT-2 User's Manual*. KEK, National High Energy Accelerator Research Organization, rev. 0.34, Dec. 2009, <http://atlas.kek.jp/tdc/amt3/>.
- [33] M. Deile et al., *Resolution and efficiency of the ATLAS muon drift-tube chambers at high background rates*, Nucl. Instr. Meth. A **535** (2004) 212.
- [34] M. Deile et al., *Performance of the ATLAS precision muon chambers under LHC operating conditions*, Nucl. Instr. Meth. A **518** (2004) 65.
- [35] S. Horvat et al., *Operation of the ATLAS muon drift-tube chambers at high background rates and in magnetic fields*, IEEE Trans. Nucl. Sci. **53** (2006) 562.

- [36] J. Dubbert et al., *Modelling of the space-to-drift-time relationship of the ATLAS monitored drift-tube chambers in the presence of magnetic fields*, Nucl. Instr. Meth. A **572** (2007) 50.
- [37] O. Kortner, *MTGEANT-4 - The Munich Test-Stand Simulation Programme*, ATL-MUON-2000-021, CERN, Geneva, Sept. 2000, <http://cds.cern.ch/record/684120>.
- [38] S. Agosteo et al., *A facility for the test of large-area muon chambers at high rates*, Nucl. Instr. Meth. A **452** (2000) 94.
- [39] B. Bittner et al., *Construction and Test of a Prototype Chamber for the Upgrade of the ATLAS Muon Spectrometer*, Physics Procedia **37** (2012) 515.
- [40] H. Kroha et al., *Construction and test of a full prototype drift-tube chamber for the upgrade of the ATLAS muon spectrometer at high LHC luminosities*, Nucl. Instr. Meth. A **718** (2013) 427.
- [41] P. Schwegler, *Construction and Test of Muon Drift Tube Chambers for High Counting Rates*, diploma thesis, Max-Planck-Institut für Physik and Technische Universität München, Nov. 2010, MPP-2010-184.
- [42] B. Bittner, *Development and Characterisation of New High-Rate Muon Drift Tube Detectors*, PhD thesis, Max-Planck-Institut für Physik and Technische Universität München, June 2012, MPP-2012-130.
- [43] J. Dubbert et al., *A proposal of building new small wheels: the NSW project*, ATL-MUON-INT-2013-003, CERN, Geneva, Nov. 2013.
- [44] G. A. Chelkov et al., *Investigation of spectral efficiency of pressurized drift tubes for detection of neutrons in the energy range between 5 eV and 200 keV*, ATL-MUON-93-031, CERN, Geneva, Nov. 1993, <http://cds.cern.ch/record/685700>.
- [45] S. Baranov et al., *Gamma sensitivity of Pressurized Drift Tubes*, ATL-MUON-94-036, CERN, Geneva, Feb. 1994, <http://cds.cern.ch/record/685755>.
- [46] S. Baranov et al., *Estimation of Radiation Background, Impact on Detectors, Activation and Shielding Optimization in ATLAS*, ATL-GEN-2005-001, CERN, Geneva, Jan. 2005, <http://cds.cern.ch/record/814823>.
- [47] G. Aielli et al., *Cavern background measurements and comparison with simulation*, ATL-COM-MUON-2013-003, CERN, Geneva, Feb. 2013.

- [48] E. Heijne et al., *Comparison of Measurement and Simulation of ATLAS Cavern Radiation Background*, ATL-COM-GEN-2013-003, CERN, Geneva, Apr. 2013.
- [49] S. König, *Ageing studies for the ATLAS MDT Muonchambers and development of a gas filter to prevent drift tube ageing*, PhD thesis, Albert-Ludwigs-Universität, Freiburg im Breisgau, Jan. 2008.
- [50] B. Bittner et al., *Performance of drift-tube detectors at high counting rates for high-luminosity LHC upgrades*, Nucl. Instr. Meth. A **732** (2013) 250 .
- [51] S. Sun et al., *Predicting Hit Rates in the ATLAS Monitor Drift Tube at $10^{34} \text{ cm}^{-2} \text{ sec}^{-1}$ at $\sqrt{s} = 7$ and 8 TeV* , ATL-COM-MUON-2013-011, CERN, Geneva, Mar. 2013.
- [52] W. Diethorn, *A methane proportional counter system for natural radiocarbon measurements*, US Atomic Energy Commission Report **NYO-6628** (1956).
- [53] M. Aleksa, *Performance of the ATLAS Muon Spectrometer*, PhD thesis, Technische Universität Wien, Sept. 1999.
- [54] M. Aleksa et al., *Rate effects in high-resolution drift chambers*, Nucl. Instr. Meth. A **446** (2000) 435.
- [55] W. Blum, W. Riegler, and L. Rolandi, *Particle Detection with Drift Chambers*, Springer-Verlag Berlin Heidelberg, 2008.
- [56] W. McDaniel and E. Mason, *The mobility and diffusion of ions in gases*, Wiley series in plasma physics, Wiley, 1973.
- [57] S. Biagi, *Monte Carlo simulation of electron drift and diffusion in counting gases under the influence of electric and magnetic fields*, Nucl. Instr. Meth. A **421** (1999) 234 .
- [58] S. Ramo, *Currents induced in electron motion*, Proc. IRE **27** (1939) 584.
- [59] R. Veenhof, *GARFIELD Users Manual*. CERN, program library W5050, <http://garfield.web.cern.ch/garfield/>.
- [60] R. D. Evans, *The Atomic Nucleus*, McGraw-Hill, New York, 1955.
- [61] O. Kortner and F. Rauscher, *Automatic Synchronization of Drift-Time Spectra and Maximum Drift-Time Measurement of an MDT*, ATL-MUON-2005-012, CERN, Geneva, 2002, <http://cds.cern.ch/record/681467>.

- [62] M. Deile et al., *An efficient method to determine the space-to-drift-time relationship of the ATLAS monitored drift tube chambers*, IEEE Nuclear Science Symposium Conference Record **1** (2007) 685.
- [63] M. Deile and N. P. Hessey, *Obtaining the Space-Time Relationship of Drift Tubes from the Drift-Time Spectrum*, ATL-MUON-99-002, CERN, Geneva, Apr. 1999, <http://cds.cern.ch/record/683844>.
- [64] P. Bagnaia et al., *Charge-dependent corrections to the time response of ATLAS muon chambers*, Nucl. Instr. Meth. A **533** (2004) 344.
- [65] S. Horvat, *Study of the Higgs Discovery Potential in the Process $pp \rightarrow H \rightarrow 4\mu$* , PhD thesis, Max-Planck-Institut für Physik and Zagreb University, Zagreb, Apr. 2005, MPP-2005-35.
- [66] D. Primor et al., *A novel approach to track finding in a drift tube chamber*, JINST **2** (2007) P01009.
- [67] J. Wotschack, *MDT Parameter Book*, , CERN, Geneva, 2007, <https://cds.cern.ch/record/1072147>.
- [68] S. Ott, *Optimization of the ATLAS Muon Detector Readout Electronics for High Rates*, master's thesis, Max-Planck-Institut für Physik and Technische Universität München, June 2014, MPP-2014-261.
- [69] Maier-Leibnitz-Laboratorium der Universität München und der Technischen Universität München. <http://www.bl.physik.uni-muenchen.de/>, 2014.
- [70] A. Zibell, *High-Rate Irradiation of 15mm Muon Drift Tubes and Development of an ATLAS Compatible Readout Driver for Micromegas Detectors*, PhD thesis, Ludwig-Maximilians-Universität, June 2014.
- [71] W. Riegler, *Limits to Drift Chamber Resolution*, PhD thesis, Technische Universität Wien, Nov. 1997, <http://cds.cern.ch/record/1274450>, CERN-THESIS-98-021.
- [72] C. Valderanis, *Study of the Performance of ATLAS Muon Drift-Tube Chambers in Magnetic Fields and at High Irradiation Rates*, PhD thesis, Max-Planck-Institut für Physik and Technische Universität München, 2012.
- [73] M. Deile, J. Dubbert, and N. P. Hessey, *Charge Division and Intrinsic Pulse Shaping in Drift Tubes*, ATL-MUON-96-105, CERN, Geneva, Jan. 1996, <http://cds.cern.ch/record/683593>.

-
- [74] M. Aleksa, N. P. Hessey, and W. Riegler, *MDT Noise Measurements in the X5 and H8 Test Beam*, ATL-MUON-98-254, CERN, Geneva, Sept. 1998, <http://cds.cern.ch/record/683709>.
- [75] L. B. Robinson, *Reduction of Baseline Shift in Pulse-Amplitude Measurements*, Rev. Sci. Instrum. **32** (1961) 1057.
- [76] ATLAS TRT Collaboration, T. Akesson et al., *Straw tube drift-time properties and electronics parameters for the ATLAS TRT detector*, Nucl. Instr. Meth. A **449** (2000) 446 .
- [77] W. Bokhari et al., *The ASDQ ASIC for the Front End electronics of the COT*, CDF/DOC/TRACKING/CDFR/4515, 1999, <http://projects-docdb.fnal.gov/cgi-bin/ShowDocument?docid=779>.

Acknowledgements

The last page is devoted to everybody going along with me during the last years. I am deeply grateful to PD Dr. Hubert Kroha for giving me the opportunity to work in an extremely exciting field and to prepare this thesis in his group. His door was always open and his continuous interest in countless discussions account for many of the insights I gained during the last years. I also want to thank him for many possibilities of travelling to CERN and many conferences and workshops, which were probably the most intense and instructive periods for me.

I am also indebted to Oliver Kortner who, despite of many other commitments, was always available for help. His advice and ideas were often my last hope and many times opened up completely new approaches.

Many people were involved in the measurement campaigns this thesis is based on. I want to thank Jörg Dubbert for passing on his expert knowledge, for being my main contact point for all the big and small issues one gets confronted with during any kind of activities at CERN and for many nice Pizza and Burger evenings.

Great thanks to all test beam crew members from the MPI group, especially Alessandro Manfredini, Daniele Zanzi, Sebastian Nowak and Sebastian Ott and to the colleagues from LMU Munich, Ralf Hertenberger and Andre Zibell for the smooth preparation of the measurements at the MLL.

I thank all my colleagues for the very nice atmosphere during the lunch and coffee breaks and in between, making the last years a pleasant time. Special thanks go to Sebastian Stern, Max Goblirsch and Rainer Röhrig for hosting all these coffee breaks in their office and to my office mate Johanna Bronner for many funny moments.

Der größte Dank gilt meinen Eltern und Großeltern für ihre von Anfang an bedingungslose Unterstützung, die mir das Studium überhaupt ermöglicht hat und für ihr stetiges Interesse, nicht nur an meiner Arbeit.

Zuletzt danke ich dem ganz besonderen Menschen in meinem Leben. Ohne Rebecca wäre die Welt für mich eine andere. Danke für all die schönen Erlebnisse, den stetigen Rückhalt und die Sicherheit, die du mir gibst und dafür dass du immer da bist wenn ich dich brauche.

